Insight into the May 2015 Inflation event at Kīlauea volcano, Hawai'i

A look into the subsurface with geodetic measurement tools

Mark J.W. Bemelmans

Committee:
Dr. Elske de Zeeuw-van Dalfsen
Prof. dr. ir. Ramon Hanssen
Dr. ir. Deyan Draganov

[This page has intentionally been left blank.]

Cover picture credit: Washington Post, obtained from `https://www.washingtonpost.com/graphics/2018/national/amp-stories/before-and-after-kilaueas-wrath-on-hawaiis-big-island/` on 12-11-2019

Insight into the May 2015 summit inflation event of the Kīlauea volcano, Hawai'i.

By

M.J.W. (Mark) Bemelmans

To obtain the degree of Master of Science
at Delft University of Technology
To be defended publicly on Wednesday December 18, 2019 at 14:00

Name supervisor	*Research department*
(Daily/Main) Dr. E. (Elske) de Zeeuw-van Dalfsen	Mathematical Geodesy and Positioning (MGP)/ Royal Dutch Meteorological Institute (KNMI)
Prof. Dr. Ir. R.F. (Ramon) Hanssen	Mathematical Geodesy and Positioning (MGP)
(External) Dr.Ir. D.S. (Deyan) Draganov	Applied Geophysics and Petrophysics (AGP)

This thesis is confidential and cannot be made public until December 18, 2019.

Preface

This now eight month long project has been a truly inspiring and motivating journey which has seen me in many emotional states from seemingly unending excitement to all consuming frustration. At times when my motivation was low, the people around me patiently supported me and when my excitement had no limit they equally patiently listened to what I had to say. Now that this project inches closer and closer to the eleventh hour, these emotions have become amplified. Dealing with all these feelings and the project, which (spoiler warning) is about an active volcano, made me think of a quote from the founder of my favourite past time, judo:

"Walk a single path, becoming neither cocky with victory nor broken with defeat, without forgetting caution when all is quiet or becoming frightened when danger threatens."

- Jigoro Kano

This quote from judo shares many facets with my graduation project. Firstly, the active volcano central to my research should at all times be treated with caution even at times when it seems to be inactive and being frightened by the volcano limits the ability to understand its complex structure and behaviour. Secondly, my progression through the project was not highest at times when I was filled with excitement over new results nor when I was filled with dread and defeat when some things didn't work out as intended, for the fiftieth time. I progressed the most when I (or my supervisors) allowed myself (or pushed me) to take a step back and consider the bigger picture and the situation at hand. I have learned a tremendous amount from the past months and will forever take those lessons with me in my upcoming adventures.

This project is not the work of just one person, many people helped or guided me throughout the project for which I am grateful. First of all I would like to thank Elske de Zeeuw-van Dalfsen. This was a first time for the both of us, me as the student and you as the supervisor. Nevertheless, you always responded with the perfect combination of support, guidance and thought provoking discussions that I needed to finish the graduation. Your expertise knowledge on volcanic processes in general and at Kīlauea specifically saved me many hours and helped me push this research to a higher level. Secondly, I would like to thank Ramon Hanssen for his critical viewpoints which refined mine. Your stimulating support throughout the project made it such that I never became insecure about my work. Similarly, I want to thank Floris Heuff, for his help with the processing of the InSAR data. Without your help I would probably still be stuck in data processing. I also want to thank my external supervisor Deyan Draganov for his critical review of this thesis.

My research could not have been possible without the data made available through the Hawaiian Volcano Observatory (HVO) for which I would like to thank Ingrid Johanson and the other researchers at the observatory who did all of the heavy lifting gathering the data. A special thanks goes out to Mike Poland who's many year at the HVO were of insurmountable importance. Our email conversations and meeting in October provided valuable insights that would not have been available to someone who has never visited the Hawaiian volcanoes. I will also thank Andy Hooper and Marco Bagnardi for their freely available GBIS software which allowed me to widen my modelling possibilities far beyond what I could have achieved in eight months time.

Finally, my family and many friends were always there to lift my spirits and sharpened my research and writing through suggestions, comment or by dragging me from my computer for a well-deserved break. In this regard I want to thank my family for their support, and thought provoking discussions sometimes lasting well into the night. I want to thank Michael who was there all throughout the process, similarly my fellow graduation companions Geiske, Meike, Kirsten, Kathelijne, Anda, Fieneke and the many others from the master track GRS or outside of that for their mutual support that kept me far away from insanity. A final big thank you goes out to all my friends from judo and climbing which have always encouraged me in my crazy endeavours.

Abstract

We use ground and space geodetic data to study surface deformation and gravity change at Kīlauea volcano from January to September 2015. This period includes an episode of heightened activity in May 2015, which we refer to as 'the May 2015 event'. The data set consists of Global Navigation Satellite System (GNSS), tilt, visual and seismic time series along with 25 descending and 15 ascending acquisitions of the Sentinel-1a satellite in Interferometric Wide swath mode and microgravity surveys taken a few years before and just after the May 2015 event. We identify four different stages of surface deformation and volcanic activity during the May 2015 event which we attribute to the movement of magma and pressure changes in response to a magma supply and withdrawal imbalance in the shallow plumbing system. In particular, we model the deformation sources attributed to the Halema'uma'u reservoir (HMMR) and South caldera reservoir (SCR). The SCR was best described by inflation of a spheroidal at 2.8 (2.65-3.07) km depth below the Southern caldera region. The HMMR source was modelled by a point source deflation located East of the Halema'uma'u crater at 1.5 (0.95-2.62) km depth. The surface microgravity changes which would result from changes in these reservoirs are significantly lower than the actually observed microgravity changes. We attribute this to the lack of complexity of the single point source model used. Mechanisms that add/remove mass from the subsurface without accompanying surface deformation, which are not part of the point source model, played a significant role. More frequent microgravity campaign surveys, even if measured at a reduced network, are the only way to improve our understanding of these processes and help to quantify them.

List of Acronyms and Abbreviations

2D FFT	two dimensional fast Fourier transform
3D	three dimensional
AGP	Applied Geophysics and Petrophysics
ALD	Azimuth Looking Direction
AOI	Area of Interest
AQG	Absolute Quantum Gravitmeter
asc	ascending
ASF	Alaska Satellite Facility
CSK	CosmoSky-MED
DEM	Digital Elevation Model
desc	descending
DI	Deflation-Inflation
DS	Distributed Scatterers
dsc	descending
EDM	Electronic Distance Measurement
ERZ	East Rift Zone
ESM	Equivalent single master
FAG	Free-Air Gradient
GBIS	Geodetic Bayesian Inversion Software
GNSS	Global Navigation Satellite System
GPS	Global Positioning System
GRS	Geoscience and Remote Sensing
HMMR	Halema'uma'u reservoir
HST	Hawai'i Standard Time
HVO	Hawaiian Volcano Observatory
ifg	interferogram
InSAR	Interferometric Synthetic Aperture RADAR
ITRF2000	International Terrestrial Reference Frame 2000
KNMI	Royal Dutch Meteorological Institute
LOS	Line of Sight
MGP	Mathematical Geodesy and Positioning
m.s.l.	mean sea level
PDF	Probability Density Function
PS	Persistent Scatterers
PSI	Persistent Scatterer Interferometry
RADAR	Radio Detection and Ranging
SAR	Synthetic Aperture RADAR

SBAS	Short Baseline Subset
SC	Southern Caldera
SCR	South caldera reservoir
SLC	Single Look Complex
SM	Single Master
SSE	sum of squared errors
StaMPS	Stanford Method for Persistent Scatterer Interferometry
SVD	singular value decomposition
SWRZ	Southwest Rift Zone
TEC	Total Electron Content
TSX	TerraSAR-X
UERZ	Upper East Rift Zone
unc.	uncertainty
USA	United States of America
USGS	United States Geological Survey
UTC	Universal Time Corrected
vv	vertical-vertical

List of Figures

List of Tables

Contents

1 Introduction

Figure 1: View of Kīlauea volcano, the focal point of this research. The Hawaiian Volcano Observatory (HVO) building is located in the foreground with the Halema'uma'u crater in the center. The plume is coming from the lava lake which shares its name with the crater. The viewing direction of this picture is to the South, the area where the rim of the Kīlauea caldera is least evident. However, the Kīlauea caldera can be seen in the upper left part of the image as a small step. Credit: M. Poland, United States Geological Survey (USGS). Public domain.

Kīlauea volcano, Hawai'i (Figure 1) is recognized as one of the most active volcanoes on earth as it has been intermittently erupting, and showing signs of activity ever since recording of these events started around 1790 [Moore and Trusdell, 1993; Poland et al., 2014]. Even before western contact, the native inhabitants were aware of the seemingly unpredictable and sometimes violent nature of Kīlauea volcano. It is therefore not surprising that Kīlauea is one of the most instrumented volcanoes in the world, leading to unique opportunities to not only monitor the volcano but also study small-scale events in tremendous detail.

It is of great importance to collect and combine all available measurements taken by satellites as well as ground-based instruments. This is the only way to get the most complete understanding of the subsurface processes. A greater comprehension of the plumbing system beneath Kīlauea will result in an increased effectiveness in mitigating future events and help to better design the observation network and fieldwork campaigns in the future [Dzurisin, 2006].

1.1 Research objective

The objective of this work is to combine ground-based observations and satellite data - in particular gravimetric surveys and Sentinel-1 SAR data - to gain insight into the intrusion that occurred in May 2015 at Kīlauea volcano. This will help build a complete story of the associated events before, during and after the intrusion.

Insight into this event is important because it is one of only a few events that occurred in the Southern caldera region, that has been observed in such detail. This is mainly because the area is significantly less active than the ERZ which has seen most of the Kīlauea activity since the Pu'u O'o vent became active in 1987 [Tilling et al., 2010]. The 2015 event provides an opportunity to better understand this part of the volcano and help focus future research. In addition, this event is one of the first Southern caldera inflation events of the volcano that has been captured in great detail by Synthetic Aperture RADAR (SAR) satellites with a high spatial resolution. The previous inflation event discussed by Myer et al. [2008]; Baker and Amelung [2012] occurred in 2006 and was captured by Interferometric Synthetic Aperture RADAR (InSAR). Jo et al. [2015] found that the likely source of the inflation is located 2.8 km below the surface, with an uncertainty of only 12 meters. This is significantly better constrained than the estimated location of the Southern caldera magma chamber by Poland et al. [2014] who places it at 2-4 km depth by reviewing past publications [Delaney et al., 1990; Delaney and McTigue, 1994; Owen et al., 1995, 2000; Cervelli and Miklius, 2003; Baker and Amelung, 2012] into the deformation of the summit in relation to magma transport and storage. These publications are based on different data sets and use different source geometries, all of which show poorly constrained depth estimates. Added insights into the subsurface of the volcano will result in a safer living and visiting environment for the over 200.000 inhabitants of the island and the many visitors. Additionally, a better understanding of the volcano in general - including the time-line of events - will aid in the prediction and the response to future events. In the light of the 2018 eruption it is clear that eruptions of Kīlauea volcano can have significant societal and economic impact. Increased insight into the volcano will help us prepare for future volcanic unrest which in turn can reduce the societal and economic impact of future eruptions.

1.2 Area of interest

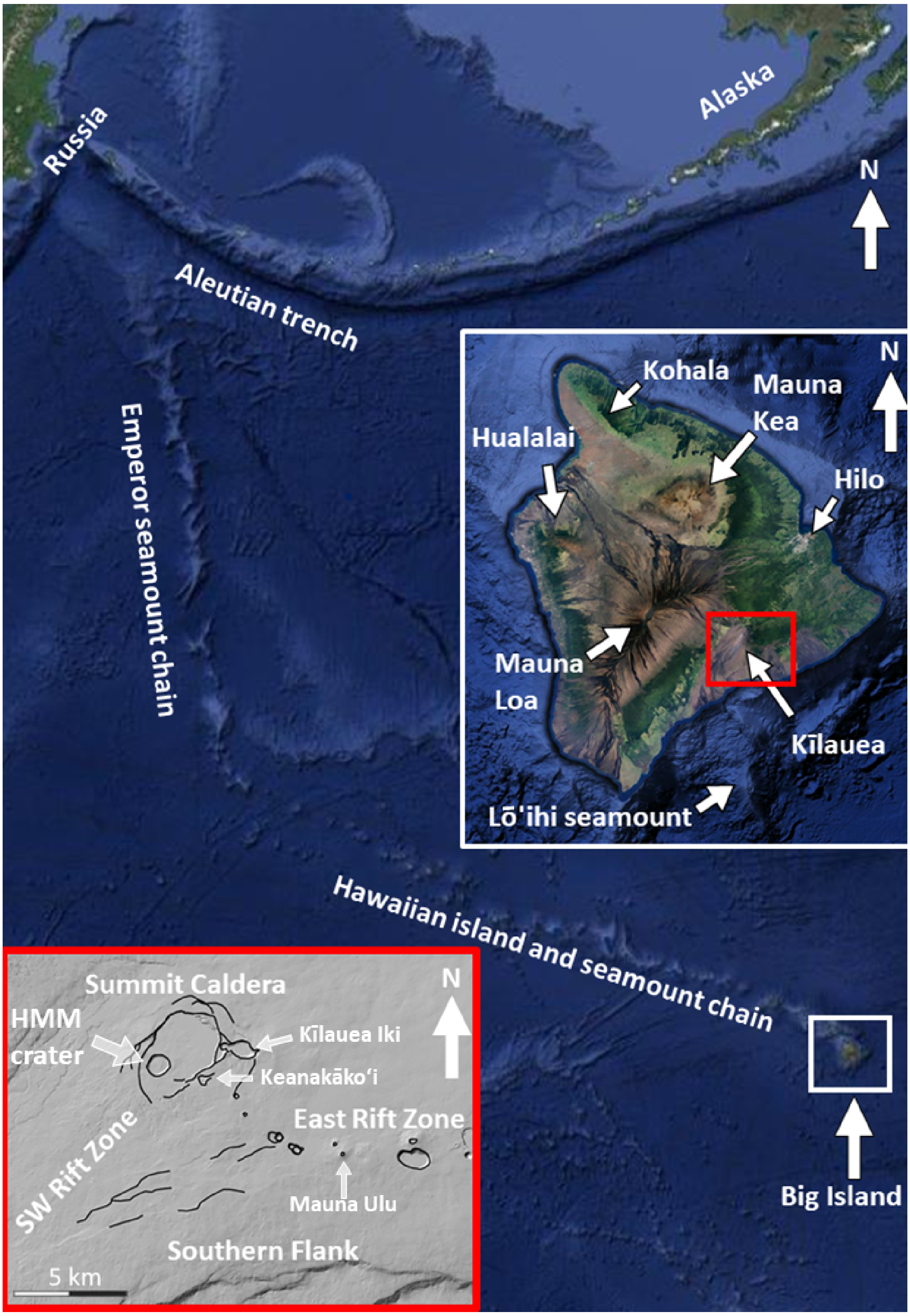

Figure 2: Geographical location of the area of interest with labels showing the relevant geographical structures. SW is Southwest. HHM = Halema'uma'u

Figure 2 shows the Big Island of Hawai'i which forms the youngest island in a chain of volcanic islands and island remnants called the Hawai'i-Emperor seamount chain. The chain stretches from the Aleutian trench to the Big Island of Hawai'i and the seamount of Lō'ihi on the southern side of the Big Island [Tilling et al., 2010].

The Big Island, with Hilo as the largest city, is comprised of five shield volcanoes: Kohala, Mauna Kea, Hualalai, Mauna Loa, and Kīlauea (see Figure 2) of which the latter three are still considered active as they have erupted in historic times [Poland et al., 2014]. Kīlauea is the most active of the Hawaiian volcanoes and has been nearly continuously active ever since observations were started over 200 years ago.

1.3 Eruptive history and origin of volcanism

The origin of these volcanic islands and seamount chain lies in a hot spot which sits underneath the pacific ocean plate and provides the energy to melt the asthenosphere and lithosphere and form volcanoes. According to Gonnermann et al. [2012] this hot spot is located more than 80 km depth and roughly 20 km south of Kīlauea. Figure 3 shows a simplified schematic of the magma supply system of Mauna Loa, Kīlauea and Lō'ihi.

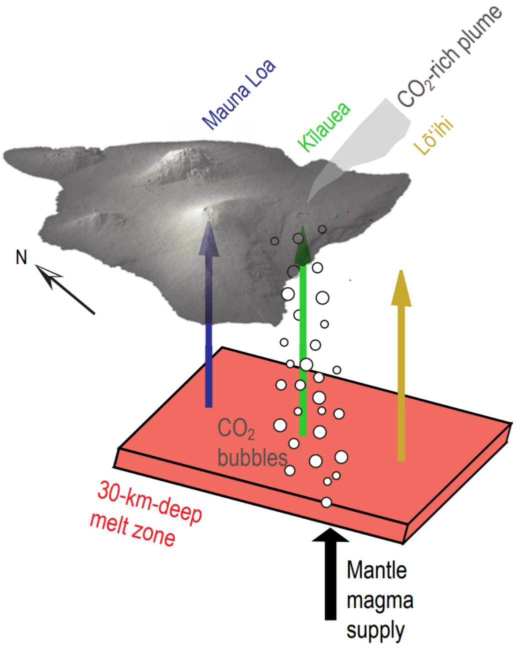

Figure 3: Schematic for the magma supply to the Hawaiian volcanoes. The black arrow shows the magma supply from the more than 80 km deep hot spot source to a nearly horizontal melt zone at 30 km depth. From this zone, magma is supplied to Mauna Loa, Kīlauea and Lō'ihi as indicated by the blue, green and yellow arrows, respectively. Kīlauea volcano is closest to the magma supply from the hot spot and most of the CO_2 rich magma travels to Kīlauea where it exits as fumes. Copied from Poland et al. [2014].

Plate tectonics cause the created islands to move away from the hot spot, allowing erosion to take over from land formation. As a result, a chain of increasingly further eroded extinct volcanoes is formed.

The eruptions at the Hawaiian volcanoes are relatively mild effusive eruptions of basaltic lava with a low viscosity. This composition allows the lava to travel vast distances and gives the island its characteristic shield-like shape. Hawaiian eruptions have given their name to this type of eruptions, meaning that around the world, eruptions of a similar style are referred to as "Hawaiian". Kīlauea volcano has several characteristic surface features which are displayed in Figure 2 and outlined in the aerial photo of Figure 4.

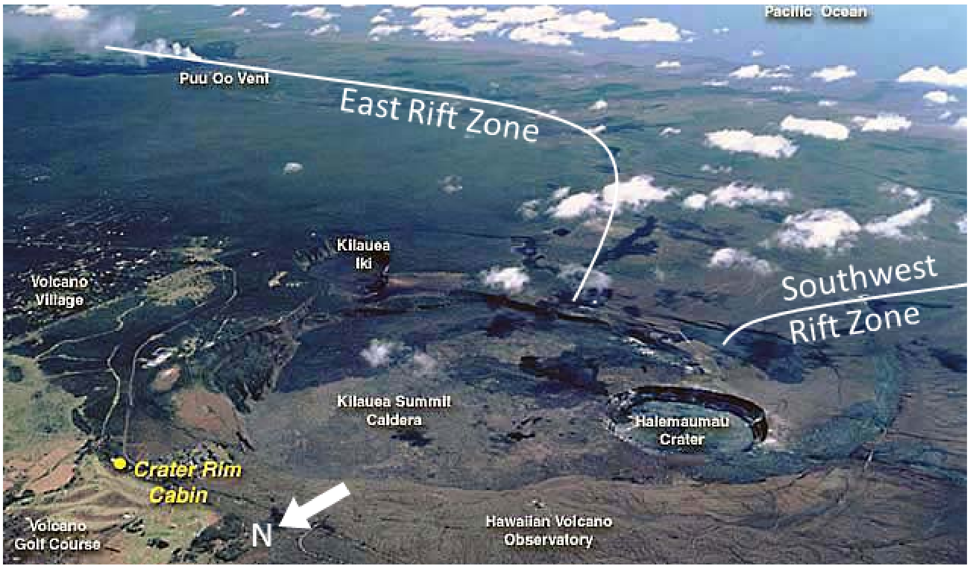

Figure 4: Aerial photograph of Kīlauea volcano including the rift zones and the Halema’uma’u crater. Image obtained from: `https://craterrimcabin.com/html/pages/summitcabin.html` on 12-11-2019.

Most striking is the Summit caldera with the Halema’uma’u crater. A caldera is a large circular or oval depression over a 1 km in size which forms most often by inward collapse after large amounts of magma have been expelled from subsurface reservoirs. In the case of Kīlauea, the summit caldera is about 5 km in diameter and the rim lies roughly 1200 m above sea level with the caldera floor at 1080 m. The nearly circular depression in the caldera floor is the Halema’uma’u crater, which is a tube-like conduit connecting the magma reservoirs to the surface. The entire crater itself was once a lava lake [Heliker et al., 2003]. However, in 2015 this lava lake, located on the western side of the Halema’uma’u crater, had shrunk to roughly 140 m by 220 m lake, connected to a vertical shaft approximately 140 m by 160 m in dimensions. The lava level varies between the floor of the Halema’uma’u crater at 1025 meters above sea level and 950 m above sea level [Bagnardi et al., 2014]. For Kīlauea, the lava lake is not the only location where magma can reach the surface. Lava also exits through fissure eruptions along the East Rift Zone (ERZ) and Southwest Rift Zone (SWRZ). Rift zones are areas of weakness in the volcano which form a locally linear area that is being rifted, or pulled apart. Volcanic rift zones provide the easiest pathways for magma to travel from the summit storage region(s). By successive eruptions from the rift zones, the volcano builds up its flanks. Rift zone intrusions are formed when the stresses created by the slope of the volcano flank and the pressure of the magma chamber(s) exceed the material strength of the rock forming a set of vertical intrusions, referred to as dikes. If the magma is able to reach the surface, fissure eruptions will take place and lava spouts out travelling down hill until it either solidifies or reaches the coast to from new land. Activity along the ERZ is more common than activity along the SWRZ, this has resulted in more land formation along the ERZ towards the Easternmost point of the Big Island. The weakness that resulted in the formation of the ERZ remains in the newly formed land, extending the rift zones. Currently, the ERZ stretches about 50 km from the summit and extends a further 70 km below the surface of the ocean to meet up with the oceanic plate, whereas the SWRZ only stretches 28 km Southwest before it reaches the coast and has no clear extension below the water. Several volcanic cones, which are surface expressions of the rift zones can be seen along the ERZ and SWRZ. From 1983 to 2018 the ERZ had an active cone with a lava lake called ”Pu’u ’Ō’ō” [Heliker et al., 2003; Dzurisin, 2006] (see Figure 4) which frequently also erupted from vents on its flanks. The eruptive activity of both Kīlauea and Mauna Loa volcanoes are presented in Figure 5.

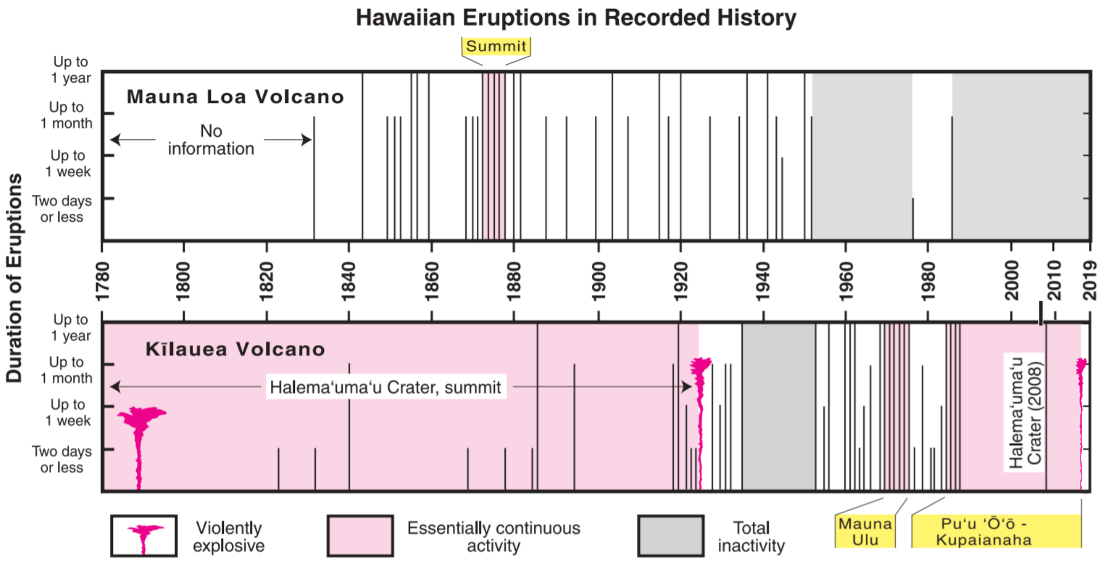

Figure 5: Volcanic activity at Mauna Loa and Kīlauea volcano from 1780 to 2019. Vertical lines indicate eruptive events of various duration. Adapted from: Tilling et al. [2010].

An essentially continuously active period at Kīlauea volcano often ends with a violently explosive period. Additionally, activity at Kīlauea volcano and Mauna Loa volcano does not seem to correlate which indicates a separated plumbing system. The violent eruption of 2018 focused on the ERZ whereas the 2015 event (which was not an eruption and is therefore not shown in the figure) took place at the Southern caldera region.

Eruptions of Kīlauea volcano occur at the summit, which includes the Halema’uma’u crater and the Southern caldera region, or along one of the two rift zones. Of the two rift zones, the East Rift Zone has historically been much more active. The plumbing system of Kīlauea volcano is not definitively known and evolves over time, but the assumed structure resembles that of Figure 6 which is copied from Poland et al. [2014].

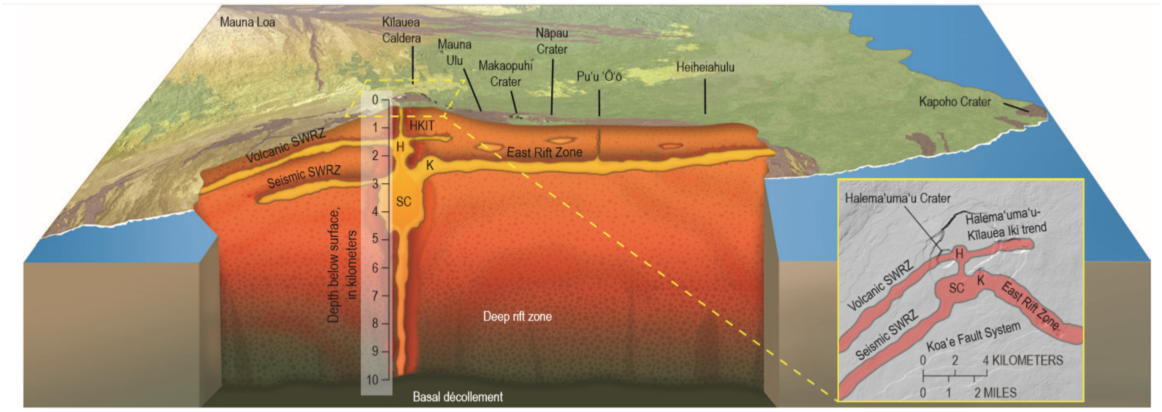

Figure 6: Illustration of the proposed structure of the Kīlauea subsurface magma plumbing system. Schematic cut-away shows a cross section through Kīlauea’s summit and rift zones. Magma pathways and storage areas are exaggerated in size for clarity. H, Halema’uma’u reservoir, K, Keanakāko’i reservoir, SC, South caldera reservoir; SWRZ, Southwest Rift Zone. Plan view gives the relations of magma pathways to surface features and topography in the vicinity of Kīlauea Caldera. Copied from: Poland et al. [2014]

The latest eruptive phase of Kīlauea volcano, lasting from 1983 to 2018, has resulted in great insight into the structure of Kīlauea volcano. This is mainly due to the dense monitoring network which started small over 100 years ago and currently records data from well over 100 instruments. The network is maintained by the HVO who were willing to share their observations for use in this research. This network contains GNSS stations and tiltmeters to measure displacement and tilt of the surface, respectively. Additionally, seismographs are able to capture the earthquakes and tremors that occur in the area and thermal cameras monitor the lava lake. The monitoring network is discussed in detail in Chapter 3. The continuous measurements of position, tilt, seismic activity, and lava level variation can be used to identify pre-eruptive change to the volcano which are used to estimate the timing, location, magnitude and likelihood of future events [Dzurisin, 2006].

1.4 Relevant previous research

Active research of Kīlauea volcano has been going on for over 100 years. This has accumulated in the currently proposed vision of the plumbing system (Figure 6). One of the first analysis of magma supply rate to Kīlauea in relation to eruptive activity using microgravity observations was performed by Dzurisin et al. [1980] who estimated the magma supply rate between 1975 to 1977 from defromation and microgravity data at 0.07-0.16 $^{kg^3}/_{year}$. Dzurisin et al. [1980] also showed that the filling or emptying of void space causes a gravity change at the surface without accompanying deformation and that this does not remove the otherwise linear relationship between maximum ground uplift and maximum gravity change, but merely changes the slope of $\Delta height$ to $\Delta gravity$. The 1975 to 1977 time period was the scene of rapid summit inflation and deflation caused by a large earthquake. In particular, the deflation of the summit was coupled to the migration of magma down the ERZ. Dzurisin et al. [1980] presents a schematic for the migration of magma from the summit down the ERZ and showed that the inflation center propagated from the summit to the middle ERZ over a period of 1.5 years as indicated by both surface deformation and gravity measurements. The first 20 years of the last eruption which took place from 1983 to 2018 are described in detail in Heliker et al. [2003] who noted that long term gravity changes in the summit region reflect both changes in the eruptive style and the stress regime. With the use of these data Heliker et al. [2003] were able to detect time periods of mass addition and subtraction to/from the summit which they directly linked to the efficiency of the ERZ conduit. Additionally, they found that the eruptions from the ERZ were not primarily fed from the shallow magma chambers, but that these were merely way-points for the magma on its way to the ERZ. The microgravity change between 1975 and 2008 was investigated by Johnson et al. [2010] who found mass accumulation in the summit region without significant surface deformation and linked this to the filling of void space (in the from of an interconnected network of cracks) beneath the summit. Johnson et al. [2010] suggests that this mass accumulation is the gradual recovery from the 1975 7.2 magnitude earthquake on the Southern flank of the volcano.

An analysis of more recent changes in the local gravity and surface deformation is performed by Bagnardi et al. [2014] who showed that between March 2011 and October/November 2012 about $0.56 \cdot 10^{11}$ kg of mass was added to the Halema'uma'u reservoir. From the surface deformation they gathered that roughly $1.71 \cdot 10^6$ m^3 of volume was added to the same reservoir. Using a magma density of 2500 $^{kg}/_{m^3}$ they found that the volume inferred from the gravity changes is about an order of magnitude larger than the inflation volume as estimated by surface deformation. Bagnardi et al. [2014] explains this significant discrepancy by saying that mass can be added to the reservoir without resulting surface deformation. This can happen by i) densification of the reservoir as magma fills spaces previously occupied by gas and/or ii) compressibility of the magma. According to Rivalta and Segall [2008], this increases the volume involved in the intrusion by (up to) a factor of 4. For the analysis of the local gravity changes between 2012 and 2015 the same gravity data from 2012 is used as was used by Bagnardi et al. [2014]. The previously discussed papers all used gravity data obtained through measurement campaigns as opposed to continuous gravity measurements. Continuous microgravity data from 2011 to 2015 were investigated by Poland and Carbone [2016] who found a strong correlation between gravity changes, lava level variation and deformation of the summit region. Increases in the gravity signal without associated surface deformation are attributed to the filling of void space, which might not have been observed from just the surface deformation and lava level data [Poland and Carbone, 2016].

The link between surface deformation and magma reservoirs was introduced by Mogi [1958] who came up with the now famous 'Mogi' models for volcano deformation, partly by assessing the surface deformation of Kīlauea volcano. The inflation leading up to the eruption of 1967-1968 provided some additional information gathered by Fiske and Kinoshita [1969]. With the use of deformation modelling, they postulated that a complex network of sills and dikes existed 2 to 3 km below the surface of Halema'uma'u crater. Fiske and Kinoshita [1969] noticed that the center of inflation would shift around the summit area. Sudden and large shifts in positions were attributed to the inflation of different regions of the complex magmatic system. The deformation modelling scene made its largest advance with the introduction of InSAR. The first major surface deformation event that was captured with InSAR is the 2000-2008 surface deformation in relation to the surge in magma supply rate from 2003 to 2007. This whole period was investigated by Baker and Amelung [2012] who identified four different magma storage areas to be the locus of deformation. The shifts in surface deformation were attributed to magma movement between these storage areas and the ERZ. The four sources they constrained with deformation source models were 1) a shallow (1.5 km depth) point source on the Eastern edge of the Halema'uma'u crater, 2) a 3 km deep penny shaped crack close to the Keanakāko'i crater, 3) another penny shaped crack located 3.6 km deep to the South of source 2. Finally, source 4, a 4 km deep dipping dike was placed in the southern caldera region oriented along the upper SWRZ axis. Baker and Amelung [2012] suggests a top-down (shallow to deep) order of inflation and deflation for the different sources. During 2007 and 2011 there have been eruptions and inflation along the ERZ which were studied by Montgomery-Brown et al. [2010, 2011] (2007 eruption) and Lundgren et al. [2013] (2011 eruption). They all linked summit activity to the inflation and eruptions of the ERZ with Lundgren et al. [2013] estimating the depth of the connecting conduit at about 3 km.

Poland et al. [2014] provides an overview regarding the magma supply, transport and storage of Kīlauea. They talk about the variations in magma supply over the past decades showing evidence for the increased magma supply rate from 2003 to 2007 and the decrease in supply rate from 2007 to 2012. This changing magma supply rate resulted in significant surface deformation in the summit region. This included an intrusion in the Southern caldera region in 2007. This intrusion was captured in great detail by the Radarsat-1 SAR satellite and was modelled by Baker and Amelung [2012] as a dipping dike intrusion at 3.6 km depth. However, Poland et al. [2014] model the same deformation source as a horizontal distributed opening with an optimal depth of 3 km. The proposed magma system by Poland et al. [2014] includes two long term magma chambers, a shallow chamber near the Halema'uma'u crater and a roughly 3 km deep chamber in the Southern caldera region. The plumbing system also includes a temporary storage area under the Keanakāko'i crater which connects the Southern caldera reservoir and the ERZ. Jo et al. [2015] is the only published work on the May 2015 inflation event. They only analyzed the surface deformation as measured by the CosmoSky-MED (CSK) satellite. They attribute the surface deformation to a dipping prolate spheroid for which the major axis is approximately 3.1 km and the two minor axes both 2.1 km located 2 km South of the Halema'uma'u crater, in the Southern caldera region. Besides a prolate spheroid model, Jo et al. [2015] also fitted a sill-like intrusion model to the deformation data but found that the distribution of the model parameters describing the sill-like intrusion from the Monte-Carlo simulation were displaying multi-modal behavior and decided that the prolate spheroid model was a better fit than the sill-like intrusion model.

1.5 Chronology of events surrounding the May 2015 intrusion

The availability of dense monitoring data provide the unique opportunity to investigate the 2015 intrusion in great detail, even though the event happened more than four years ago. An analysis of observations described and logged by the HVO and the Smithsonian Institution Global volcanism program led to a list of events which occurred directly before, during or after the intrusion.

Table 1: List of events surrounding the May 2015 event.

Date of event	Description of event
21 - April - 2015	Abrupt but small magnitude inflation (positive radial tilt) of the summit area beginning at 16:40.
23 - April - 2015	Rise of lava lake at Halema'uma'u crater to 20m below rim.
23 - April - 2015	Collapse of overhanging Western wall of the Halema'uma'u crater at 05:20.
24 - April - 2015	Inflation since April 21st reaches 4.5 microrad of radial tilt measured by the summit tilt-stations.
25 - April - 2015	Rise of lava lake to 12m below rim. Radial tilt reaching 5.5 microrad.
28 - April - 2015	Lava lake slowly rises to 3-4m below rim, briefly reaching the rim on 28-04. Radial tilt reaching 7.5 microrad.
29 - April - 2015	Lava lake overflowed multiple times starting at 21:40 of the previous night. No additional (radial) tilt.
30 - April - 2015	New rim created, lava level 4m below new rim. Seismicity raise from normal levels at summit and upper ERZ areas.
05 - May - 2015	Lava lake overflows multiple times between 01-05 and 05-05. Slight inflationary radial tilt since April 30th.
10 - May - 2015	Deflation detected in summit area combined with a significant drop in lava level, deflation continued until 12-05.
12 - May - 2015	Overflows almost daily since 06-05, new rim 10m higher than old rim. Seismicity increased at the upper SWRZ.
13 - May - 2015	Change from deflation in summit area to rapid and localized inflation just South of the Kīlauea caldera. (recorded by tilt). Seismicity decreased at Upper ERZ, seismicity continued at SWRZ. Seismicity increased slightly Northwest from the summit.
14 - May - 2015	Increase in seismicity in summit and upper SWRZ (southern part of the caldera).
15 - May - 2015	Lava level 50 m below new rim. Seismicity rates remain elevated in the southern part of the Kīlauea caldera. Inflation just south of summit caldera continued.
18 - May - 2015	Tilting slowed since 16-05, seismicity in SWRZ above background level but reduced.
19 - May - 2015	Inflation deflation cycle recurred at at the summit associated with the Halema'uma'u source. No tilting associated with May 15th event. Seismicity back at normal levels.

Each of the developments in this sequence plays a role and helps to understand the sub-surface changes that took place pre-dating the May 2015 event.

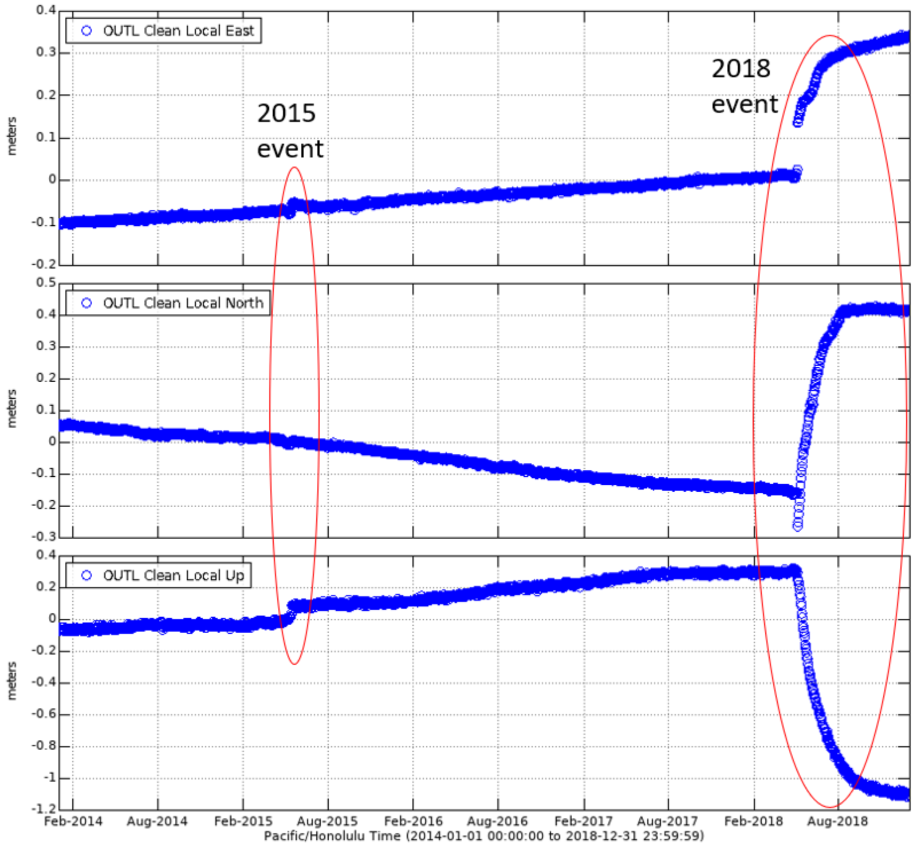

Figure 7: Measured displacement of the OUTL GPS station from January 2014 to December 2018.

As shown by Table 1, the inflation event of May 15th 2015 occurred after a sequence of other observable changes, which started on April 21st 2015. The availability of these observations allows for targeted research into this event which did not lead to an eruption. But does, nevertheless, provide a significant amount of information.

After May 19th 2015 the activity of Kīlauea volcano returned to 'normal' levels and no major deformation event occurred at the summit until the destructive eruption started in May 2018. The time in between was characterized by slow but steady deformation of the Kīlauea summit and the ERZ as the volcano was building up pressure. When displaying deformation covering both event (Figure 7), we can see that the intrusion of 2015 was minor in comparison to the 2018 event. Studying comparatively small events like the May 2015 intrusion is important in order to understand the plumbing system of the volcano and the large amount of data available from the HVO makes it possible to gain insight into the volcano even from non-eruptive events.

1.6 Research question

The previously mentioned objective can be formulated into the following main research question:

- *Which insights can we get from Sentinel-1 InSAR data and in-situ measurements concerning the location, geometry, mass change and evolution of the May 2015 event at the Southern caldera of Kīlauea volcano, Hawai'i?*

The combination of the data collected by HVO and the Sentinel-1a satellite will possibly provide additional insights and conformation to the Jo et al. [2015] research. Additionally, modelling of the intrusion might be able to provide quantitative estimates of the parameters describing the modelled intrusion. The research question can be divided into several questions each describing a smaller subsection of the research.

- *Do the GNSS, tilt, lava lake level and seismic activity data agree with each other on the timing, location, and evolution of the intrusion?*

The gravimetric surveys and the InSAR data have a poor temporal resolution. In contrast, the GNSS, tilt, lava lake level and seismic activity data is (nearly) continuous and provide a clear time-line of the surface deformation as well as subsurface activity. The time, location, and the evolution of the intrusion can be estimated or described from these observations if they show a strong correlation in time and space.

- *Does the deformation obtained from the InSAR data agree with the results from other surface deformation data sets?*

  The InSAR data provides an estimate of surface deformation for the entire area or interest. The pattern of surface deformation and its evolution through time as obtained from InSAR processing should agree with that obtained from the GNSS and tilt stations.

- *Are the gravimetric surveys able to constrain the location, geometry and volume change of the magmatic intrusion?*

  If the depth of the intrusion is not exceedingly deep ($\leq$ 10km), and the volume of the intrusion is sufficiently large, microgravity campaigns should show a pattern from which we might be able to put boundaries on the location, geometry and volume change of the intrusion. If however, the intrusion turns out to be very deep and/or the volume too small, we cannot provide an estimate of the intrusions' properties based on the microgravity survey.

- *Do the estimation of model parameters, describing the location, shape and size of the intrusion, from deformation and mass change models agree with each other and with the current understanding of the plumbing system of the volcano?*

  By modelling the possible geometry of the intrusion, we might be able to estimate the size and location of the intruded volume or mass. If the inversion of the model parameters from the observations is successful, the estimations on the size, location and shape of the deformation/mass change source can be linked to specific parts of the Kīlauea plumbing system in order to tell a complete story regarding the intrusion.

1.7 Novelty of the research

The research is novel because it looks at one of the first summit intrusions since the 'modern' monitoring era that includes data from high resolution SAR satellites. The research is novel in three ways:

- Gravimetry data were analyzed to gain insight into the mass changes in the area.
- Satellite-based data from Sentinel-1 with a high temporal resolution were used to detect surface deformation related to this event.
- The combination of ground based and satellite observations was used for the analysis of this event.

This research will provide valuable insight into the structure of the magmatic system underneath the Kīlauea summit. It will add a piece to the complex puzzle that is the subsurface of Kīlauea as it may support our current understanding of the plumbing system of the volcano, or it will help to further our understanding.

The upcoming chapter 2 provides background information on the various techniques and methods used for this work. Chapter 3 describes the data used in this work in detail. In chapter 4 the method of this research is explained in detail. Chapter 5 will go over the results objectively in preparation for chapter 6 - the discussion - where the meaning of the results will be dissected. Finally, in chapter 7 - the conclusion - the findings are discussed and the research questions are answered.

2 Background information

2.1 InSAR principles

2.1.1 Interferometric phase

The technology of InSAR has provided a powerful tool for analyzing surface displacement, also around volcanoes [Dzurisin, 2006]. InSAR uses data collected by SAR satellites like the Sentinel-1 satellite used in this research. These satellites send out a radar signal and receive the return signal after it has been reflected from the surface. Allowing the return signal to be received after the satellite has moved along its orbit effectively increases the aperture of the satellite. This in turn significantly improves the spatial resolution of the image.

The image acquired from the SAR satellite is focused and the data is provided in the form of a Single Look Complex (SLC) image. Each pixel of this image is represented by a complex value as shown by: (after [Samiei Esfahany, 2017])

$$P = Re(P) + jIm(P) = Ae^{j\phi}. \tag{2.1.1}$$

Where P is the complex value associated to the pixel, $Re(P)$ and $Im(P)$ are the real and imaginary parts of P, respectively. This encodes both amplitude A and phase ϕ information. The phase of the SLC image is ambiguous with respect to multiples of 2π. Ignoring atmospheric, scattering and other noise terms, the phase of the SLC pixel is related to the 2π-modulus of the two way distance between the satellite and the target as: (after [Samiei Esfahany, 2017])

$$\phi_{SLC} = W\Big(\frac{-4\pi}{\lambda} d(sat, target)\Big). \tag{2.1.2}$$

The wrapping operator $W(.)$ wraps the signal within the interval $[-\pi, \pi)$ [Samiei Esfahany, 2017], the transmitted radar signal wavelength λ, and the Euclidean distance between the satellite and the target $d(sat, target)$. The Sentinel-1a satellite has a 12 day repeat orbit [Babu and Kumar, 2019]. This means that the satellite returns and measures the same area every 12 days. The information provided by the difference in phase between the two SLC images can be used to get information on the position of the target or the deformation of the target that occurred between the two acquisitions [Samiei Esfahany, 2017].

These phase differences are collected in an interferogram which is produced by multiplying one SLC image with the complex conjugate of an aligned second SLC image. This process is described mathematically by:

$$I_{MS} = P_M P_S^* = A^M A^S \exp j(W(\phi_M - \phi_S)), \tag{2.1.3}$$

where * indicates the complex conjugate operation, sub- and superscripts M and S refer to the master and slave image, respectively. The convention is that the slave image is interpolated to align with the master image. It is common to discuss the interferometric phase which is the phase value of the complex-valued interferogram given by:

$$\phi_{MS} = W(\phi_M - \phi_S). \tag{2.1.4}$$

2.1.2 Range dependent interferometric phase

Without considering differences in atmospheric phase delay, scattering phase, noise phase, and the deformation of the target, the interferogram will still show phase differences between the two images. This is because these images are taken from slightly different geometries (e.g. with a non-zero interferometer baseline). Figure 8 shows the acquisition geometry of an interferogram.

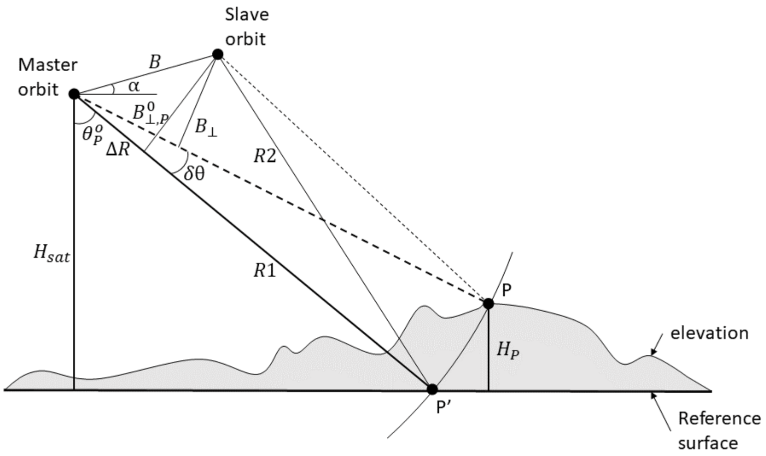

Figure 8: Interferogram acquisition geometry. The point P is located at a distance R_1 from the master orbit and at height H_P and can not be distinguished from point P' (at an angle of θ^o_P off nadir) on the reference surface by a single (master) acquisition. The change in look angle $\delta\theta$ and the off-horizontal baseline angel α can only be measured by introducing a slave orbit which is separated by baseline B, of which the projection perpendicular to $R1$ is called $B^0_{\perp,P}$. This results in a range difference between the slave and master orbits of ΔR. This together with the height of the satellite H_{sat} is used to compute H_P. Alternatively, if H_P is provided by an external source, the deformation of point P in the LOS direction of the master can be computed. Often, in the case of SAR satellites $||B|| \ll H_{sat}$. Illustration by author, adapted from [Hanssen, 2001].

Figure 8 shows the geometry of the interferogram acquisition. The point P is located on the surface at an elevation of H_P and a distance R_1 from the master orbit. The point P' is also a distance R_1 from the master orbit and therefore would have the same range related phase. The slave orbit is at a distance R_2 from point P'. Ignoring the phase contribution due to signal propagation delay, the range related phase recorded during the master and slave orbits is given by [Hanssen, 2001]:

$$\varphi_{1P'} = -\frac{4\pi R_2}{\lambda} + \varphi_{scat,1P} \text{ , and} \tag{2.1.5}$$

$$\varphi_{2P'} = -\frac{4\pi R_2}{\lambda} + \varphi_{scat,2P}, \text{ respectively.} \tag{2.1.6}$$

With λ as the wavelength of the radar signal. In the case of the Sentinel-1 satellites this is about 5.6 cm. The scattering phase contribution of both images is given by $\varphi_{scat,1P}$ and $\varphi_{scat,2P}$. The interferometric phase for point P' can therefore be written as

$$\phi_{P'} = \varphi_{1P'} - \varphi_{2P'} = -\frac{4\pi(R_1 - R_2)}{\lambda} + (\varphi_{scat,1P} - \varphi_{scat,2P}). \tag{2.1.7}$$

In the situation where the scattering phase contribution is the same for both acquisitions, i.e. $(\varphi_{scat,1P} - \varphi_{scat,2P}) = 0$, equation (2.1.7) can be written as:

$$\phi_{P'} = -\frac{4\pi\Delta R}{\lambda} = -\frac{4\pi}{\lambda} B\sin(\theta^\circ_P - \alpha), \tag{2.1.8}$$

with ΔR the difference in range to point P' from the master and slave orbits. This ΔR can also be expressed as $\Delta R = B\sin(\theta^\circ_P - \alpha)$, with θ°_P as the angle from nadir to the point P'. The point P' on the reference surface and the point P on the actual surface are equidistant to the master orbit but not to the slave orbit. This is because P is not located on the reference surface but instead at an height H_P away from this surface. This adds another component to the interferometric phase. This phase signal due to topography is referred to as ϕ_P^{topo}. The signal due to topography is described as [Hanssen, 2001]:

$$\phi_P^{topo} = -\frac{4\pi}{\lambda} \frac{B^{\circ}_{\perp,P}}{R_1 \sin\theta^{\circ}} H_P, \tag{2.1.9}$$

where $B^{\circ}_{\perp,P}$ is the perpendicular baseline between the master and slave acquisitions for point P'. The signal due to deformation is described in the LOS direction and is therefore given as a change in the range from the master orbit to the point P. On top of the signals from orbit geometry and topography, deformation of the surface between the two SLC acquisitions causes a third phase signal which comprises the final part of the interferometric phase that is not due to atmospheric signal delay or the scattering properties of the surface. This is referred to as the deformation phase ϕ_P^{def}. The deformation phase due to LOS deformation D_P is given by:

$$\phi_P^{def} = -\frac{4\pi}{\lambda} D_P. \tag{2.1.10}$$

The range dependent interferometric phase is effectively the superposition of three signals. Namely the signals from orbit geometry and topography as well as deformation that occurred in the time between the master and slave acquisition. The combination of these three components results in the range dependent interferometric phase given by:

$$\phi_P = \frac{4\pi}{\lambda} \left(B\sin(\theta_P^{\circ} - \alpha) - D_P - \frac{B^{\circ}_{\perp,P}}{R_1 \sin\theta^{\circ}} H_P \right). \tag{2.1.11}$$

One of the applications of SAR interferometry is to estimate the shape of the earth with respect to the selected reference surface. For this, the phase signal due to the orbit geometry is removed and the baseline is taken as large as possible to make the phase contribution from topography much larger than that of the possible deformation. The other major application of InSAR is to measure the deformation of the surface. For this, the signals due to the orbit geometry and due to the elevation of the surface with respect to the reference surface need to be removed. The orbit parameters are known and the phase signal can be estimated. The signal due to the topography can be obtained from an external Digital Elevation Model (DEM). The removal of both these unwanted signals results in the so called differential interferometric phase. This should in theory only contain the deformation phase signal. However, errors in the orbit calculation and in the DEM will propagate into the differential interferometric phase [Hanssen, 2001].

2.1.3 Errors in range dependent interferometric phase

The range dependent interferometric phase is not only a function of LOS deformation but also of relative satellite position (orbital geometry), topography, and the location of the phase center with respect to the center of the pixel. This introduces a number of error terms to the range dependent interferometric phase.

Firstly, inaccuracies in the orbit geometry express themselves as changes in baseline B and baseline angle from horizontal α. The resultant residual phase due to these inaccuracies is referred to as ϕ^{orb}. Secondly, changes in look angle can arise from errors in topography (DEM errors) as well as a difference between the center of the pixel and the phase center of the pixel. The phase center is the location within a pixel from which the combined contribution of all scatterers within that pixel originates (e.g. if the dominant scatter within a pixel is located near one of the corners of the pixel, the phase center is shifted from the assumed center of the pixel towards the corner with the dominant scatterer). The error in look angle is given by [Hooper et al., 2007]:

$$\Delta\theta = \frac{\Delta H sin(\theta) + \xi cos(\theta)}{R}, \tag{2.1.12}$$

where ΔH is the error in height with respect to the reference surface, θ is the angle of incidence at the surface from the center of the pixel, and ξ is the horizontal distance between the center of the pixel and the phase center of the pixel in range direction.

Finally, there is also an error in the azimuth direction due to a difference between the center of the pixel and the phase center in the azimuth direction. This results in a phase difference due to a change in squint angle [Hooper et al., 2007]:

$$\Delta\phi_v = \frac{2\pi}{v} F_{DC}\eta, \tag{2.1.13}$$

where $\Delta\phi_v$ is the difference in range dependent phase due to squint angle, v is the sensor velocity, F_{DC} is the difference in Doppler centroid frequency, and η is the horizontal distance between the center of the pixel and the phase center in azimuth direction. This term is expected to be small and is treated as noise [Hooper et al., 2007].

2.1.4 Interferometric phase

After coregistration, the interferometric phase of pixel x in interferogram i can be expressed as:

$$\phi_{x,i} = W(\varphi_{x,i}^{def} + \varphi_{x,i}^{atmo} + \Delta\varphi_{x,i}^{orb} + \Delta\varphi_{x,i}^{\theta} + \varphi_{x,i}^{noise}), \tag{2.1.14}$$

where the signal of interest $\varphi_{x,i}^{def}$ represents the phase change due to movement of the pixel in the LOS direction. The residual phase due to satellite orbit uncertainties is $\Delta\varphi_{x,i}^{orb}$ and $\Delta\varphi_{x,i}^{\theta}$ is the residual phase due to errors in look angle. There are two more terms, $\varphi_{x,i}^{atmo}$ is the phase signal due to differences in atmospheric delay of the signal between the two passes. This is mostly due to water vapor content in the troposphere and Total Electron Content (TEC) in the ionosphere [Hanssen, 2001] and is often the largest unwanted phase contribution. The last term, $\varphi_{x,i}^{noise}$, is the phase signal due to noise and is formed by variability in scattering properties of the pixel between passes, thermal noise, coregistration errors and uncertainty in the position of the phase center in the azimuth direction [Hooper et al., 2007].

2.2 InSAR time series

A collection of SLC images of the same target area taken at different times can form many different interferograms with one selected master image. This is called a Single Master (SM) stack. This results in phase differences associated with the deformation of the target area occurring between the acquisition time of the master and the slave image. Some of the pixels in the interferograms will contain a point like dominant scatterer which has a higher amplitude than the background scatterers and may result in a low variance in phase with respect to the movement of the background scatterers. This may allow for the estimation of the deformation signal [Hooper et al., 2007]. These pixels behave like time consistent point scatterers and are called Persistent Scatterers (PS). Analytically, these pixels have $|\varphi_{x,i}^{noise}|$ in equation (2.1.14) sufficiently small such that it does not dominate the interferometric phase. A group of adjacent pixels that together behave similarly throughout the stack are called Distributed Scatterers (DS). A visual representation of PS and DS pixels is given by [Samiei Esfahany, 2017](figure 2.6) is copied in figure 9.

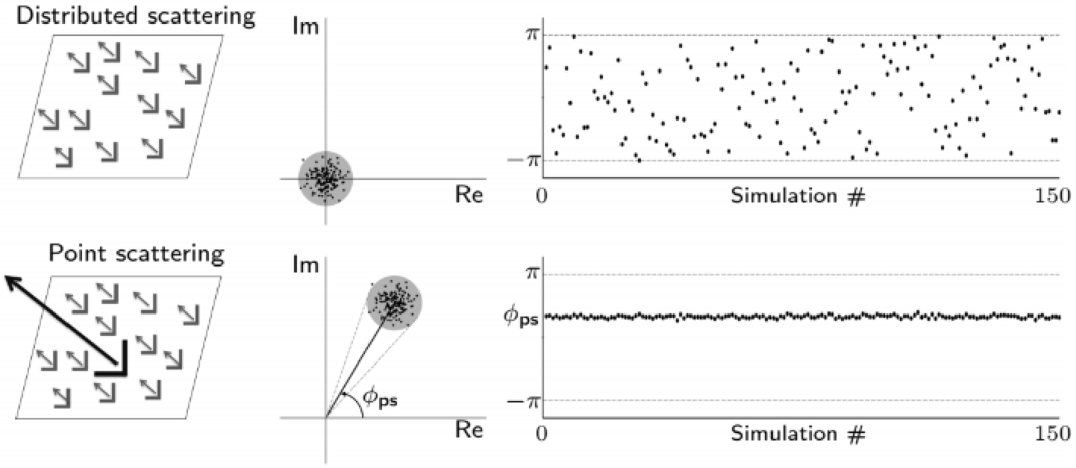

Figure 9: Distributed vs point scattering - Top row: a distributed scatterer resolution cell, bottom row: dominant point scatterer resolution cell. The plots on the left show a stylized arrangement of elementary scatterers within a resolution cell. The biggest object corresponds to the dominant point scatterer. The plots in the middle show the phasors corresponding to 150 simulations. In each simulation, the location of the scatterers (except the dominant scatterer) changed randomly. The plots on the right show the phase behavior of different scattering resolution cells for 150 simulations. It is clear how the large amplitude of the dominant scatterer influences the phase dispersion, while for the distributed scattering, phase values are randomly distributed between $[-\pi, \pi)$. For the point scattering case, they are distributed with much smaller dispersion around the phase of the dominant scatterer (ϕ_{ps}). Copied from Samiei Esfahany [2017], after [Hooper, 2006]

Both PS and DS can be used to create a time series of the deformation. However, it is expected that the area of interest, comprised mostly of solidified lava flows, will have a sufficient PS density to make use of Persistent Scatterer Interferometry (PSI).

The first step in creating a time series of deformation from InSAR is by creating a stack of interferograms. The method used in this research requires the collection of interferograms to be reference and coregistered to the same master image. The coregistration is important as it aligns the slightly different geometries of each SLC image to the same grid (i.e the grid of the master image). Coregistration is described by:

$$S_{coregi} = \frac{MS^{*}M^{*}}{MM^{*}} = \frac{MS^{*}M^{*}}{(A^{M})^{2}}, \tag{2.2.1}$$

where M and S refer to the master and slave SLC pixel values, resepctively, and A^M refers to the amplitude of the master SLC pixel values. With these coregistered SLC the single master stack of interferograms can be created.

This research uses the Stanford Method for Persistent Scatterer Interferometry (StaMPS) to estimate the phase change due to LOS deformation from a collection of interferograms referenced to the same master image. Such a collection is called a SM stack. The method identifies the pixels that behave like PS pixels; because for these pixels the noise term does not dominate over the deformation signal. The StaMPS is described in detail by Hooper et al. [2004, 2007].

From 2.1.4 we determined that the interferometric phase is comprised out of five components:

$$\phi_{x,i} = W(\varphi_{x,i}^{def} + \varphi_{x,i}^{atmo} + \Delta\varphi_{x,i}^{orb} + \Delta\varphi_{x,i}^{\theta} + \varphi_{x,i}^{noise}). \tag{2.2.2}$$

PS pixels are those for which $|\varphi_{x,i}^{noise}|$ does not dominate over the signal. The variation in the first four terms in equation 2.2.2 dominate the interferometric phase which makes the estimation of the noise term from the wrapped phase difficult. Because of this we try to estimate these four terms and subtract them from $\phi_{x,i}$ in order to get an estimate of the noise term $\widehat{\varphi}_{x,i}^{noise}$ which can be used for the selection of PS pixels. With $\widehat{\varphi}_{x,i}^{noise}$ we can re-estimate the first four terms and allows for a better estimation of $\widehat{\varphi}_{x,i}^{noise}$. This iteration is performed until values converge.

The first three terms and part of the fourth term in equation (2.2.2) are spatially correlated [Hooper et al., 2007]. Estimating the spatially correlated part of $\phi_{x,i}$ allows for the removal of this part of the interferometric phase and provides an estimate of the spatially uncorrelated part from which the noise term can be estimated and used for the selection of PS pixels.

The initial selection of PS pixels is performed using normalized amplitude dispersion. This is because temporal amplitude stability is a proxy for phase stability and phase stability can not be directly estimated from wrapped interferograms [Samiei Esfahany, 2017]. The normalized amplitude dispersion D_A is calculated by:

$$D_A = \frac{\sigma_A}{\mu_A} = \frac{\sigma_n}{\mu_A} = tan(\sigma_{\varphi}) \approx \sigma_{\varphi}, \tag{2.2.3}$$

where μ_A and σ_A are the mean and standard deviation of the amplitudes across the stack respectively. This proxy assumes that the signal remains constant across the stack and that the noise has a zero-mean circular complex Gaussian distribution. The threshold for D_A is taken to be 0.4 which results in the majority of pixels selected not being PS. This is done so that we can be sure that almost all actual PS pixels are selected.

StaMPS uses a combination of a low-pass filter and a band-pass filter that adapts to the phase gradient present in the data [Hooper et al., 2007]. Before filtering the amplitude of each pixel is weighted according to an estimate of the inverse square of the probability that that pixel is a PS pixel. This is done by setting the amplitude of each pixel to $1/[p(x \in PS)]^2$, where $p(x \in PS)$ is the probability of pixel x being a PS pixel. The probability that a pixel is a PS pixel cannot be determined directly from the wrapped interferometric phase. So, initially the pixels are weighted by setting the amplitude of the pixels to $1/D_A$.

2.2.1 Filtering towards residual interferometric phase

The weighted PS pixels are then down-sampled to a grid of 50 m to aid in the use of the two dimensional fast Fourier transform (2D FFT). Over this length-scale there is little variation in phase, which allows for effective down-sampling. If multiple PS pixels fall in the same grid cell, their complex values are summed [Hooper et al., 2007]. The 2D FFT is applied to a 32×32 grid of cells. The intensity of the 2D FFT is smoothed by convolution with a 7×7 pixel Gaussian window. This forms the adaptive part of the filter $H(u,v)$. The filter response is given by:

$$G(u,v) = L(u,v) + \beta\left(\frac{H(u,v)}{\bar{H}(u,v)} - 1\right)^{\alpha}, \tag{2.2.4}$$

where $G(u,v)$ is the combined low-pass and adaptive band-pass filter response, $L(u,v)$ is a fifth-order Butterworth filter with a cutoff wavelength of 800 m that acts as the low-pass filter. $\bar{H}(u,v)$ is the median of the adaptive band-pass filter response $H(u,v)$. α and β are adjustable weighting parameters that for our case are set to 1 and 0.3, respectively, u and v are the spatial coordinates of the filtering grid.

The result of the applied filter is $\phi_{x,i}^{corr}$, which represents the wrapped estimate of the spatially correlated part of the interferometric phase. Subtracting $\phi_{x,i}^{corr}$ from $\phi_{x,i}$ in equation (2.2.2) gives:

$$W(\phi_{x,i} - \phi_{x,i}^{corr}) = W(\varphi_{x,i}^{def,u} + \varphi_{x,i}^{atmo,u} + \Delta\varphi_{x,i}^{orb,u} + \Delta\varphi_{x,i}^{\theta,u} + \varphi_{x,i}^{noise,u}), \tag{2.2.5}$$

where φ^u represents the spatially uncorrelated part of φ. Since $\varphi_{x,i}^{def}$, $\varphi_{x,i}^{atmo}$, and $\Delta\varphi_{x,i}^{orb}$ are spatially correlated and will be filtered by $G(u,v)$, it is expected that $\varphi_{x,i}^{def,u}$, $\varphi_{x,i}^{atmo,u}$, and $\Delta\varphi_{x,i}^{orb,u}$ are small and their sum can be replaced with $\delta_{x,i}$ in equation (2.2.5) to give:

$$W(\phi_{x,i} - \phi_{x,i}^{corr}) = W(\Delta\varphi_{x,i}^{\theta,u} + \varphi_{x,i}^{noise,u} + \delta_{x,i}). \tag{2.2.6}$$

From equation (2.1.8) an approximate relationship between phase and change in look angle is found [Hanssen, 2001]:

$$\partial\varphi_{x,i}^{\theta} \approx -\frac{4\pi}{\lambda} Bcos(\theta - \alpha)\partial\theta = -\frac{4\pi}{\lambda} B_{\perp,x,i}\partial\theta_x \tag{2.2.7}$$

According to Hooper et al. [2007], as long as $\Delta\varphi_{x,i}^{\theta,u}$ contains the roughly the same frequency components for all i, the approximate relationship between $\Delta\varphi_{x,i}^{\theta}$ and $\Delta\theta_x$ hold true for $\Delta\varphi_{x,i}^{\theta,u}$ and $\Delta\theta_x^u$. Substituting $\Delta\varphi_{x,i}^{\theta,u}$ in equation (2.2.6) according to approximation (2.2.7) gives:

$$W(\phi_{x,i} - \phi_{x,i}^{corr}) = W(-\frac{4\pi}{\lambda} B_{\perp,x,i}\Delta\theta_x^u + \varphi_{x,i}^{noise,u} + \delta_{x,i}). \tag{2.2.8}$$

It is expected that $B_{\perp,x,i}$ does not correlate with $\varphi_{x,i}^{noise,u}$ or $\partial_{x,i}$. This allows us to estimate $\Delta\widehat{\theta}_x^u$ in a least squares sense. The contribution of the master image to $\varphi_{x,i}^{noise,u} + \delta_{x,i}$ is present in every interferogram and expresses itself as a constant offset which needs to be estimated by least squares inversion.

The estimate $\Delta\hat{\theta}_x^u$ is used to calculate $\Delta\widehat{\varphi}_{x,i}^{\theta,u}$ which is subtracted from equation (2.2.8) resulting in:

$$W(\phi_{x,i} - \phi_{x,i}^{corr} - \Delta\widehat{\varphi}_{x,i}^{\theta,u}) = W(\varphi_{x,i}^{noise,u} + \delta_{x,i}^{'}), \tag{2.2.9}$$

where $\delta_{x,i}^{'} = \varphi_{x,i}^{noise,u} + \delta_{x,i}) - \Delta\widehat{\varphi}_{x,i}^{\theta,u}$ [Hooper et al., 2007].

We can now construct a value for the variation of the residual phase of a pixel as expressed by equation (2.2.9):

$$\gamma_x = \frac{1}{N}\left|\sum_{i=1}^{N} exp[j(\phi_{x,i} - \phi_{x,i}^{corr} - \Delta\widehat{\varphi}_{x,i}^{\theta,u})]\right|, \tag{2.2.10}$$

where N is the number of interferograms in the stack.

2.2.2 PS probability

If we assume that the noise term of equation (2.2.2) is approximately equal to $\varphi_{x,i}^{noise,u}$ and that $\partial_{x,i}$ is sufficiently small, γ_x is an assessment of the phase noise level of the pixel and can act as an indicator to decide if that pixel is a PS pixel. There is an expected correlation between the value of γ_x and the probability that the pixel x is a PS pixel. A probability density function of γ_x, $p(\gamma_x)$, can be estimated by normalizing and binning the values of γ_x. If we then treat the selection of PS pixels as the union of two groups, group A only containing PS pixels and group B only containing non-PS pixels, we can express $p(\gamma_x)$ as the weighed sum of the probability density functions of the two groups

$$p(\gamma_x) = \kappa p_A(\gamma_x) + (1-\kappa)p_B(\gamma_x). \tag{2.2.11}$$

Here κ varies between 0 and 1. We need to estimate κ and $p_B(\gamma_x)$ in order to evaluate the probability of a pixel being a PS pixel. $p_B(\gamma_x)$ is evaluated by simulating 10^6 pseudopixels with random phase [Hooper et al., 2007] and following the method described above to estimate $p_B(\gamma_x)$. Hooper et al. [2004, 2007] found that $\gamma_x \leq 0.3$, $p_A(\gamma_x) \approx 0$. This implies that:

$$\int_0^{0.3} p(\gamma_x)d\gamma_x = (1-\kappa)\int_0^{0.3} p_B(\gamma_x)d\gamma_x. \tag{2.2.12}$$

The data is used to evaluate the left-hand side of the equation and the simulated pseudopixels are used to evaluate the right-hand side in order to get an estimate for κ. With this we are able to compute the probability that pixel x is a PS pixel:

$$P(x \in A) = 1 - \frac{(1-\kappa)p_B(\gamma_x)}{p(\gamma_x)}. \tag{2.2.13}$$

This probability is then used to weight the pixels before spatial filtering to estimate $\widehat{\varphi}_{x,i}^{noise}$ which then more accurately constrains $p(\gamma_x)$ from which we get a better estimate of the probability that a pixel is a PS pixel. This iterative process is continued until the change in the mean value of γ_x reaches 0.005.

2.2.3 Displacement time series estimation

After the most likely PS pixels have been selected we go back to the wrapped interferometric phase of equation (2.2.2) and only consider the selected pixels in order to estimate the phase due to deformation (the first term on the right-hand side of equation (2.2.2)). For this the interferometric phase needs to be unwrapped and the other terms on the right =-hand side need to be estimated. We already have an estimate for the spatially uncorrelated part of the look angle error, $\widehat{\varphi}_{x,i}^{\theta,u}$ and the spatially uncorrelated master phase contribution, $\widehat{\varphi}_x^{m,u}$. Both these estimates are subtracted from the interferometric phase before unwrapping resulting in:

$$W(\phi_{x,i}-\widehat{\varphi}^{\theta,u}_{x,i}-\widehat{\varphi}^{m,u}_{x}) = W(\varphi^{def}_{x,i}+\varphi^{atmo}_{x,i}+\Delta\varphi^{orb}_{x,i}+\Delta\varphi^{\theta,c}_{x,i}+\Delta\varphi^{noise}_{x,i}), \tag{2.2.14}$$

where the spatially correlated part of $\Delta\varphi^{\theta}_{x,i}$ is denoted by $\Delta\varphi^{\theta,c}_{x,i}$ and $\Delta\varphi^{noise}_{x,i}$ is the spatially uncorrelated noise term with the spatially uncorrelated master phase contribution removed (e.g $\Delta\varphi^{noise}_{x,i} = \varphi^{noise}_{x,i} - \widehat{\varphi}^{m,u}_{x}$).

The unwrapping is performed in three dimensions (two spatial dimensions and one temporal dimension) and the method is described in Hooper and Zebker [2007]. After unwrapping, the phase will be of the form:

$$\widehat{\varphi}_{x,i} = \varphi^{def}_{x,i}+\varphi^{atmo}_{x,i}+\Delta\varphi^{orb}_{x,i}+\Delta\varphi^{\theta,c}_{x,i}+\Delta\varphi^{noise}_{x,i}+2k_{x,i}\pi, \tag{2.2.15}$$

where $\widehat{\varphi}_{x,i}$ is the unwrapped value of $W(\phi_{x,i}-\widehat{\varphi}^{\theta,u}_{x,i}-\widehat{\varphi}^{m,u}_{x})$ and $k_{x,i}$ is the unknown integer ambiguity. If unwrapping is sufficiently accurate, kx,i will be the same for most x in interferogram i [Hooper et al., 2007].

The terms $\varphi^{atmo}_{x,i}$, $\Delta\varphi^{orb}_{x,i}$, $\Delta\varphi^{\theta,c}_{x,i}$, and $\Delta\varphi^{noise}_{x,i}$ can still obscure the signal of interest, $\varphi^{def}_{x,i}$. These terms contain a spatially correlated part which can be estimated in order to isolate the deformation signal. The uncorrelated part of the unwanted terms is modelled as noise in the deformation modelling. The spatially correlated part of the unwanted terms is further divided in a part which is expected to correlate in time and a part which is expected not to be. The contribution of the master to $\varphi^{atmo}_{x,i}+\Delta\varphi^{orb}_{x,i}+\Delta\varphi^{\theta,c}_{x,i}$ will be correlated in time and the slave contribution the $\varphi^{atmo}_{x,i}+\Delta\varphi^{orb}_{x,i}$ as well as $\Delta\varphi^{\theta,c}_{x,i}$ is expected not to correlate with time. These two parts are estimated separately using a combination of temporal and spatial filters.

The spatially correlated master phase contribution is estimated by low-pass filtering in time. An issue arises however, because the integer ambiguity, which - not being estimated - causes decorrelation in time for the whole interferogram. This makes temporal filtering inapplicable for the whole interferogram. However, neighboring PS pixels will most likely have the same value for $k_{x,i}\pi$. This allows us to use the phase difference between neighboring PS pixels, because it cancels the $2k_{x,i}\pi$ term in the majority of situations. A spatial network is made using Delaunay triangulation, taking the phase difference around each triangle in clockwise direction to use as input for the spatial filtering [Hooper et al., 2007]. The phase difference calculation is performed according to:

$$\Delta^{x2}_{x1}\widehat{\varphi}_{x,i} = \Delta^{x2}_{x1}\varphi^{def}_{x,i}+\Delta^{x2}_{x1}\varphi^{atmo}_{x,i}+\Delta^{x2}_{x1}\Delta\varphi^{orb}_{x,i}+\Delta^{x2}_{x1}\Delta\varphi^{\theta,c}_{x,i}+\Delta^{x2}_{x1}\Delta\varphi^{noise}_{x,i}, \tag{2.2.16}$$

where the phase differencing operation between PS pixels $x2$ and $x1$ is indicated by Δ^{x2}_{x1}. Low-pass temporal phase filtering is performed by convolution f the differenced phase with a Gaussian window of 730 days. This width is chosen as it is expected that deformation rate will vary within this time period and the master contribution is expected to remain constant over this time period. This filtering results in:

$$\mathscr{L}^{T}(\Delta^{x2}_{x1}\widehat{\varphi}_{x,i}) \approx \Delta^{x2}_{x1}\varphi^{def}_{i} - \Delta^{x2}_{x1}\varphi^{atmo,m} - \Delta^{x2}_{x1}\Delta\varphi^{orb,m}, \tag{2.2.17}$$

where $\mathscr{L}^{T}(\cdot)$ describes the low-pass filter operator. At the time of the master acquisition, $\varphi^{def}_{x} = 0$ for all x. This time therefore, gives us an estimate of $\Delta^{x2}_{x1}\widehat{\varphi}^{atmo,m} + \Delta^{x2}_{x1}\Delta\widehat{\varphi}^{orb,m}$. By means of least squares inversion the estimate of $\widehat{\varphi}^{atmo,m} + \Delta\widehat{\varphi}^{orb,m}$ can be retrieved. The slave contribution to the spatially correlated phase is estimated by subtracting the result from the low-pass filter from the differenced phase, effectively creating a high-pass filter in time. This is done because this signal is expected not to correlate with time. the slave contribution is estimated by:

$$\Delta^{x2}_{x1}\widehat{\varphi}_{i} - \mathscr{L}^{T}(\Delta^{x2}_{x1}\widehat{\varphi}_{i}) \approx \Delta^{x2}_{x1}\varphi^{atmo,s}_{i} + \Delta^{x2}_{x1}\Delta\varphi^{orb,s}_{i} + \Delta^{x2}_{x1}\Delta\varphi^{\theta,c}_{i} + \Delta^{x2}_{x1}\Delta\varphi^{noise}_{i}, \tag{2.2.18}$$

where the superscript s denotes the slave contribution to these terms. Again, by least squares inversion the slave contribution with respect to an arbitrary PS pixel can be estimated:

$$\left[\Delta^{x2}_{x1}\right]^{-1}\left(\Delta^{x2}_{x1}\widehat{\varphi}_{i} - \mathscr{L}^{T}(\Delta^{x2}_{x1}\widehat{\varphi}_{i})\right) \approx \varphi^{atmo,s}_{x,i} + \Delta\varphi^{orb,s}_{x,i} + \Delta\varphi^{\theta,c}_{x,i} + \Delta\varphi^{noise}_{x,i}, \tag{2.2.19}$$

where $\left[\Delta^{x2}_{x1}\right]^{-1}$ is the inverse phase differencing operator with respect to the reference PS pixel. The result of equation (2.2.19) is then spatially filtered by convolution with a two-dimensional Gaussian function with a width of 50 m. This width is selected to include all of the signal except for that in the direct vicinity of the individual PS pixel. The result of this filter is an estimate of $\widehat{\varphi}_{x,i}^{atmo,s} + \Delta\widehat{\varphi}_{x,i}^{orb,s} + \Delta\widehat{\varphi}_{x,i}^{\theta,c}$. With the results from the different spatial and temporal filters, equation (2.2.15) can be rewritten to provide an estimate of the deformation phase:

$$\varphi_{x,i}^{def} - \Delta\varphi_{x,i}^{noise} - 2k_{x,i}\pi \approx \widehat{\varphi}_{x,i} + \left(\widehat{\varphi}_{x}^{atmo,m} + \widehat{\varphi}_{x}^{orb,m}\right) - \left(\widehat{\varphi}_{x,i}^{atmo,s} + \Delta\widehat{\varphi}_{x,i}^{orb,s} + \Delta\widehat{\varphi}_{x,i}^{\theta,c}\right). \tag{2.2.20}$$

With sufficiently accurate unwrapping and by only looking at a small region of the interferogram scene, the contribution of $2k_{x,i}\pi$ reduces to zero and leaves only the phase due to deformation, spatially uncorrelated noise and unwrapping errors [Hooper et al., 2007].

The product of the StaMPS method is a time series of deformation phase and some of the unwanted phase terms that were estimated for each PS pixel in the interferogram stack. This time series information is used in the further analysis of the volcano deformation.

2.3 Gravimetry

Measuring local changes in gravity over time at a volcano provide a unique opportunity to get an indication of mass variation beneath the surface. This can provide evidence for mass accumulation, or drainage from subsurface reservoirs. Especially in combination with deformation measurements does the unique and great power of gravity measurement become clear. Gravity measurements can be used to detect activity volcanic activity that might otherwise be missed. An example of this is the filling or evacuation of void space [Dzurisin et al., 1980; Bagnardi et al., 2014], which would result in comparatively small surface deformation in relation to the mass accumulation or removal. Additionally, the combination of deformation and gravity data can provide constraints on the density of subsurface sources responsible for the geodetic unrest. Gravity measurements provide an estimate of the mass while deformation measurements provide an estimated volume, the division of the two properties give the estimated density of the added or removed mass.

The fact that the plumbing system of Kīlauea volcano contains many different elements (magma reservoirs, connecting conduits, and possible pathways, see Figure 6) makes gravity measuring an interesting tool to study the activity of this volcano. The movement of mass below the surface causes changes in the gravitational acceleration at the surface. Besides the movement of magma, other processes such as the variation of groundwater level contribute to a change in the gravity field [Carbone et al., 2017]. This can be derived from the law of gravitational force given by: (Discovered by Newton and mentioned in [Johannes and Smilde, 2009], among others)

$$\boldsymbol{F_g} = -G\frac{m_1 m_2}{|\boldsymbol{r}|^3}\boldsymbol{r}, \tag{2.3.1}$$

where $\boldsymbol{F_g}$ is the gravitational force acting on mass m_2 caused by m_1. G is the universal gravitational constant approximately equal to $6.67 \cdot 10^{-11} m^3 kg^{-1} s^{-2}$. The relative distance between the two masses is described by vector $\boldsymbol{r}$ and points from m_1 to m_2. The acceleration of the second point mass caused by the first point mass is given by $\boldsymbol{g}$:

$$\boldsymbol{g} = \frac{\boldsymbol{F_g}}{m_2} = G\frac{m_1}{r^3}\boldsymbol{r}. \tag{2.3.2}$$

Gravitational acceleration obeys the superposition principle, thus the gravitational acceleration of a test mass due to a collection of point masses is equal to the vector sum of the individual accelerations caused by the individual point masses [Johannes and Smilde, 2009]. However, this still uses a discrete distribution of mass in point masses. The same property can also be expressed for continuous space if it is described in terms of the density rather than the mass. The density ρ at a particular point described by vector r is defined by:

$$\rho(\boldsymbol{r}) = \frac{dm(\boldsymbol{r})}{dv}, \tag{2.3.3}$$

with dm as the mass element located within the volume element dv. The equation for gravitational acceleration can now be written as a volume integral: (After [Poisson and Will, 2014; Johannes and Smilde, 2009])

$$\boldsymbol{g}(\boldsymbol{r}) = -G\iiint_V \frac{\rho(\boldsymbol{r'})}{(|\boldsymbol{r}-\boldsymbol{r'}|)^3}(\boldsymbol{r}-\boldsymbol{r'})dv, \tag{2.3.4}$$

where $\boldsymbol{g}(\boldsymbol{r})$ is the gravitational acceleration vector at location $\boldsymbol{r}$ whereas $\boldsymbol{r'}$ denotes the position vector of a point inside the volume V.

It becomes apparent from equation (2.3.4) that a change in the distribution of mass or density can lead to a change in the gravitational acceleration vector at a particular point of interest.

Devices that measure the (plumb line component of the) gravitational force are called gravimeters and come in two general forms: absolute gravimeters and relative gravimeters. The absolute gravimeters measure the distance traveled by an object over time to determine the acceleration of the mass (i.e. gravity) - in free-fall - at that location [Faller, 2002]. More recently, an Absolute Quantum Gravitmeter (AQG) has appeared on the market which measures the distance travelled by a cloud of cold atoms using laser interferometry [Ménoret et al., 2018]. Relative gravimeters do not make a direct measurement of the acceleration but measure a proxy such as the changes in the dilation of a spring (supporting a mass) caused by changes in the gravity or the current required to generate the magnetic field that suspends a spherical test mass [Fores et al., 2016; Carbone et al., 2017]. The data which are analyzed in this work were measured using spring-based relative gravimeters.

As mentioned, the spring-based gravimeters measure changes in the dilation of a spring supporting a mass. The dilation of an elastic material due to an applied force is given by Hooke's law. The relative gravimeters usually only provide gravity measurements along one axis [Lederer, 2009]. If the gravimeter is properly level this would be the plumb line direction and Hooke's law simplifies to:

$$F = k(\Delta z), \tag{2.3.5}$$

where F is the force applied in the direction of dilation/contraction, Δz is the change in length of the spring and k is the proportionality constant more commonly known as the spring constant. This is the one-dimensional equivalent to the Young's modulus of the spring material.

The main force that is applied to the sensor contained within the gravimeter is the force due to the gravitational attraction between the Earth and the instrument. Relative gravimeters often use zero-length springs, as was first applied by LaCoste in 1935 [LaCoste, 1935], which allows for the replacement of Δz in equation (2.3.5) with $\boldsymbol{z}$, the vector describing the direction and change of length of the spring. This results in the following estimation of gravity by use of a spring:

$$|\boldsymbol{g}| = \frac{k}{m}\boldsymbol{z}. \tag{2.3.6}$$

Measurements of gravity are commonly given in milliGal ($mGal$) or even microGal(μGal) which are defined as 10^{-5} and 10^{-8} $m \cdot s^{-2}$, respectively.

2.3.1 Free-Air Gradient (FAG) correction

The gravity is measured in surveys often several months or years apart. Between surveys, the area of interest might have moved up or down. This effectively changes the distance to the center of mass of the Earth which changes the measured gravity. If the area has moved up, the distance to the center of mass of the Earth increases and the measured gravity decreases. We are interested in the change of gravity over time due to the movement of mass mass in the subsurface, also called 'microgravity'. The signal due to the vertical movement of the measurement location between surveys needs to be estimated and removed from the measured gravity change to arrive at microgravity values. Figure 10 shows the geometry of the situation.

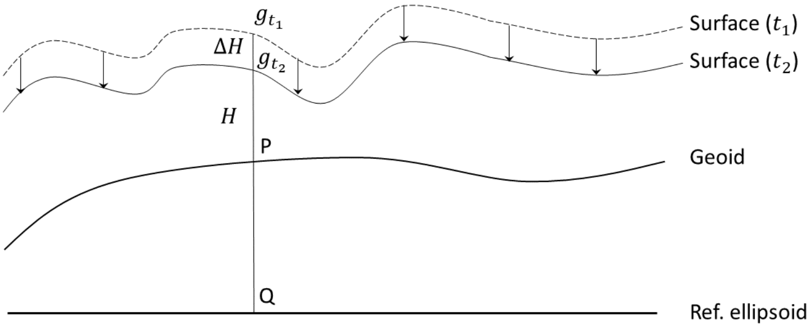

Figure 10: Geometry of Free-Air Gradient correction. With g_{t1} and g_{t2} indicating the value of gravity at the same location but at different times and elevation difference ΔH. Point Q is the orthogonal projection of the point on the surface onto the reference ellipsoid. Point P is the location where this projection crosses the Geoid. Illustration by author.

The gravity on the reference ellipsoid can be computed and is referred to as the normal gravity. The gravity $g(t_1)$ and $g(t_2)$ for times t_1 and t_2, respectively, can be written as:

$$g(t_1) = \gamma_P + \frac{\partial \gamma}{\partial n} H_1 + g_{mass1} \text{ and} \tag{2.3.7}$$

$$g(t_2) = \gamma_P + \frac{\partial \gamma}{\partial n} H_2 + g_{mass2}, \text{ respectively.} \tag{2.3.8}$$

With γ as the normal gravity at that location at the Geoid height and g_{mass} is the gravity signal measured due to anomalous mass in the subsurface. The difference in height between t_1 and t_2 is ΔH which makes the difference between the gravity values equal to:

$$\Delta g = g(t_2) - g(t_2) = g_{mass2} - g_{mass1} + \frac{\partial \gamma}{\partial n}(H_2 - H_1) = g^{res} + \frac{\partial \gamma}{\partial n} \Delta H. \tag{2.3.9}$$

The Free-Air Gradient is given by $\frac{\partial \gamma}{\partial n}$ and represents the change in normal gravity γ with respect to height n normal to the surface of the ellipsoid. For mid-latitudes the theoretical Free Air Gradient is -0.3086 $^{\mathrm{mGal}}/_{\mathrm{m}}$ [Johannes and Smilde, 2009].

The gravity measurements from equation (2.3.9) are with reference to the normal gravity at the Geoid height. However, the relative gravity measurements in the field are relative to the base station. This only changes the reference from γ_P to the gravity at the base station and adds a component caused by the vertical displacement of the base station between the two campaigns. The equation for the temporal difference in gravity at benchmark i ($\Delta^t g^{rel}_{BM,i}$) can be altered to: (adapted from Battaglia et al. [2018])

$$\Delta^t g^{rel}_{BM,i} = g^{rel}_{BM,i}(t_2) - g^{rel}_{BM,i}(t_1) = \frac{\partial \gamma}{\partial n} \Delta H_{BM,i} + g^{rel}_{BM,i} + \frac{\partial \gamma}{\partial n} \Delta H^{base} , \tag{2.3.10}$$

where Δ^t denotes a difference in time instead of space. As mentioned, the Free-Air Gradient $^{\partial \gamma}/_{\partial n}$ is generally equal to -0.3086 $^{mGal}/_{m}$ which together with the height change at benchmark location i ($\Delta H_{BM,i}$) gives the free-air anomaly. The relative gravity is determined with respect to the base station. Because of this, the vertical displacement of the base station is also included in the difference between relative gravity measurements. Locally determined Free-Air Gradient values like -0.3273 $^{mGal}/_{m}$ [Johnson, 1992] and -0.33025 $^{mGal}/_{m}$ [Kauahikaua et al., 2003] would not have a significant effect on the calculated residual gravity given the limited vertical displacement of the benchmarks between measurement campaigns. Bagnardi et al. [2014] states that in their research the use of locally determined Free-Air gradients would result in an effect of $< 4\mu Gal$ for about 0.20 m of vertical displacement. The vertical displacement observed by Bagnardi et al. [2014] is of similar magnitude to the vertical movement measured during our study period. Because of that we choose to use the theoretical Free-Air Gradient of $-0.3086\ ^{mGal}/_{m}$.

2.4 Volcano deformation modelling

The deformation patterns related to volcanic activity are often the result of subsurface pressure or volume changes in a volume with a geometry that can be approximated by a simple shape (i.e a sphere, disk, or dipping rectangular prism). The surface deformation according to pressure or volume changes of these simple shapes can be calculated with knowledge of the elastic properties (Poison's ratio and shear modulus) of the subsurface. Several models have been proposed describing different inflation/deflation geometries: spherical source [Mogi, 1958; McTigue, 1987], dipping oblate spheroid [Yang et al., 1988], rectangular dislocation [Okada, 1992] and a horizontal penny shaped crack [Fialko et al., 2001]. These shapes or geometries and their location are described by a set of parameters $\vec{d}$. These parameters vary per source geometry. An effective search for these parameters and their uncertainties is performed by Bayesian inversion as described in detail by Bagnardi and Hooper [2018]. This section provides a summary of the work by Marco Bagnardi and Andrew Hooper who provided the Geodetic Bayesian Inversion Software (GBIS).

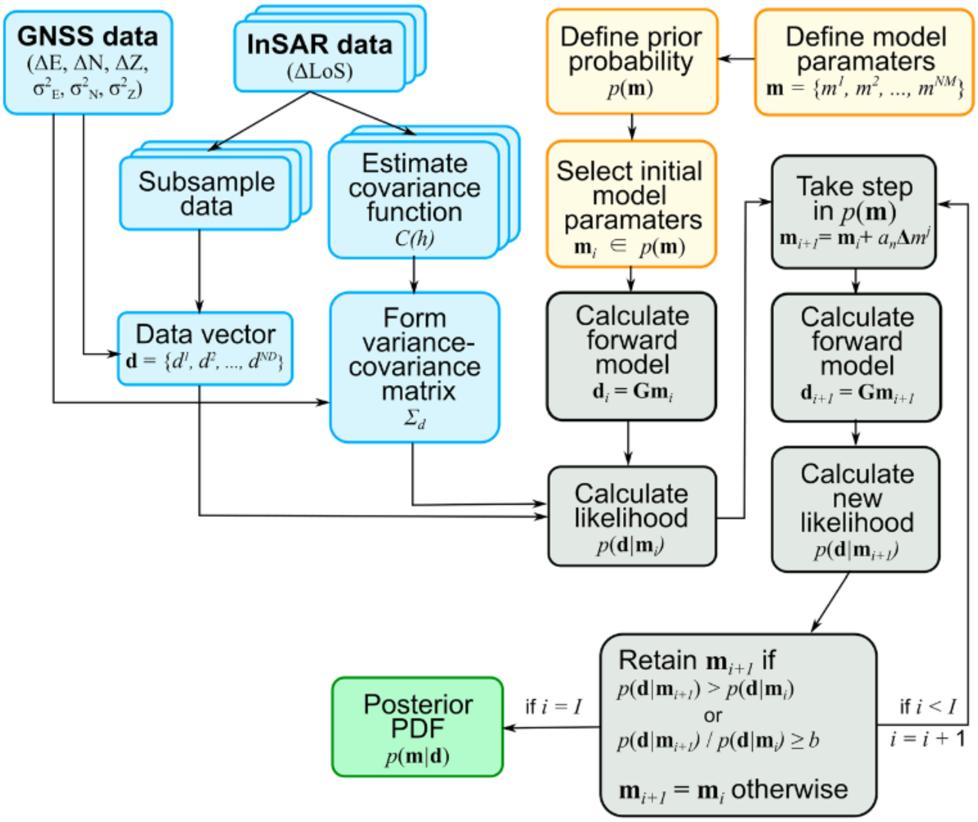

Figure 11: schematic overview of the GBIS method as described by Bagnardi and Hooper [2018]. The recursive loop is the Markov chain Monte Carlo method-Metropolis-Hastings iterative algorithm where b is a random value with a uniform distribution within the range $[0,1]$. A detailed explanation of each step is provided in Bagnardi and Hooper [2018] from which this figure is copied.

GBIS tries to estimate the parameters $\boldsymbol{m} = \{m^1, m^2, \dots, m^{NM}\}$ of the non-linear model $\boldsymbol{G}(\boldsymbol{m})$ that best describes observation vector $\boldsymbol{d} = \{d^1, d^2, \dots, d^{ND}\}$. The observation vector and the model are related by:

$$\boldsymbol{d} = \boldsymbol{G}(\boldsymbol{m}) + \boldsymbol{\varepsilon}. \tag{2.4.1}$$

Where ε are the residuals between the modelled deformation and the observations. The posterior PDF that describes how well a given set of model parameter $\boldsymbol{m}$ can explain the observation $\boldsymbol{d}$ based on the observation uncertainty and a-priori information is expressed as $p(\boldsymbol{m}|\boldsymbol{d})$ and is calculated according to:

$$p(\boldsymbol{m}|\boldsymbol{d}) = \frac{p(\boldsymbol{d}|\boldsymbol{m})p(\boldsymbol{m})}{p(\boldsymbol{d})}. \tag{2.4.2}$$

Where $p(\boldsymbol{d}|\boldsymbol{m})$ is the likelihood function of parameter vector $\boldsymbol{m}$ given observations $\boldsymbol{d}$ and is calculated from the residuals between the modelled deformation and the measured deformation. Prior information about the parameters is captured by $p(\boldsymbol{m})$ which is given as a joint PDF of the model parameters. The denominator $p(\boldsymbol{d})$ is a normalization constant used to bring the probability values within $p(\boldsymbol{d}|\boldsymbol{m})$ to within the interval $[0,1]$. The residuals are assumed to be multivariate Gaussian with zero mean and covariance matrix $\boldsymbol{Q}_{dd}$ (i.e $\in\sim N(\boldsymbol{0},\boldsymbol{Q}_{dd})$). The likelihood function $p(\boldsymbol{d}|\boldsymbol{m})$ is calculated by:

$$p(\boldsymbol{d}|\boldsymbol{m}) = (2\pi)^{-\frac{N}{2}}|\boldsymbol{Q}_{dd}|^{-\frac{1}{2}}exp[-\frac{1}{2}(\boldsymbol{d}-\boldsymbol{G}(\boldsymbol{m}))^T\boldsymbol{Q}_{dd}^{-1}(\boldsymbol{d}-\boldsymbol{G}(\boldsymbol{m}))], \tag{2.4.3}$$

where N is the total number of observations and $\boldsymbol{Q}_{dd}^{-1}$ is the inverse of the variance-covariance matrix acting as the weight matrix of the residuals.

Assuming independence of the model parameters, the probability of the parameter vector ($p(\boldsymbol{m})$) is given by the multiplication of the probabilities of the individual model parameters:

$$p(\boldsymbol{m}) = \Pi_{i=1}^{N}Mp(m^i). \tag{2.4.4}$$

In our case, prior information about the model parameters is only available in terms of upper and lower bounds for the possible source geometries as taken from literature. Outside of these bounds $p(m^i) = 0$ while the remaining possible values are equally probable. A detailed explanation of the iterative process and the selection and control of the step size is given by Bagnardi and Hooper [2018] who provided the software.

2.4.1 Down-sampling of InSAR data

The InSAR data acquired from StaMPS contains approximately $2\cdot10^5$ PS pixels per stack. To aid computational efficiency, this data is reduced using an adaptive quadtree sampling, described as the gradient based method in Decriem et al. [2010]. This algorithm recursively divides the image in four equally sized regions and checks whether the phase variance in each region exceeds a predefined threshold value. If the phase variance of a region is above the threshold, it is further divided into four regions until the phase variance of each region is below the threshold. The phase value of all points within each polygon is averaged and assigned to the polygon centroid. Small polygons containing two or less data points are removed because the deformation gradient in this area is likely due to errors in phase unwrapping during StaMPS processing. The resulting sampling is densest where the gradient in phase is the highest and excludes regions with a very low density of PS pixels which vary significantly in phase.

3 Instrument network and data description

This chapter describes the data used in this study. The fact that, around the time of the May 2015 event, a suite of instruments recorded a broad range of measurements allows us to study the event in great detail. The data can be placed in one of four categories: 1) seismic data (Section 3.1), 2) deformation data (Section 3.2), visual observations 3.3, and 3) micro-gravity data (Section 3.4). The second category is further divided into ground observations (section 3.2.1), including GNSS and tilt measurements, and space-based InSAR observations (section 3.2.2). All ground observation data is made available though the HVO and InSAR data used was either obtained by Mike Poland of the USGS in the case of the CSK and TSX data, or from the Alaska Satellite Facility (ASF) in the case of the Sentinel-1 data.

The correlation between the timing of the observation, made with different data sets, and the different stages of the May 2015 event is of great importance. Therefore, all data were split into three main intervals coinciding with the different stages of the event as shown in Table 2.

Table 2: Stages of the May 2015 event by start and end date.

Name of stage		Name of sub-stage	Stage start date [yyyy-mm-dd]	Stage end date [yyyy-mm-dd]	Duration [days]
Pre-event			2015-01-01	2015-04-20	110
Event			2015-04-21	2015-05-18	28
	Stage A	Summit inflation/lava lake rise	2015-04-21	2015-04-29	9
	Stage B	Lava lake at crater edge	2015-04-30	2015-05-09	10
	Stage C	Summit deflation/lava lake drop	2015-05-10	2015-05-12	3
	Stage D	Southern caldera inflation and lava lake drop	2015-05-13	2015-05-18	6
Post-event			2015-05-19	2015-05-31	105

An interval of about three and a half months is taken before and after the event to show pre- and post-event stability. The May 2015 event itself, can be subdivided further into four different stages: A) Summit inflation and rise of lava level (from 21-04-2015 to 29-04-2015), B) lava lake at crater edge (from 30-04-2015 to 09-05-2015), C) summit deflation and drop of lava level (from 10-05-2015 to 12-05-2015), and D) Southern caldera inflation (from 13-05-2015 to 18-05-2015). These shorter intervals are not desirable for time series data with a temporal resolution of ≥ 1 day like GNSS and InSAR time series will not benefit from an analysis of a two day long time interval. In those cases the entire time series is analyzed and, where possible, related to the stages of the May 2015 event.

3.1 Seismic activity

Seismic activity is one of the go-to information sources for observing volcanic activity. With a sufficient number of seismographs located in the vicinity of the volcano, it is possible to detect the timing and the location of earthquakes [McNutt, 2002]. Kīlauea's monitoring network includes a vast array of seismographs for the detection of tremors and earthquakes as well as more advanced signal processing to invert the sub-surface velocity field [Chouet, 2003]. The location of the seismographs is presented in Figure 12.

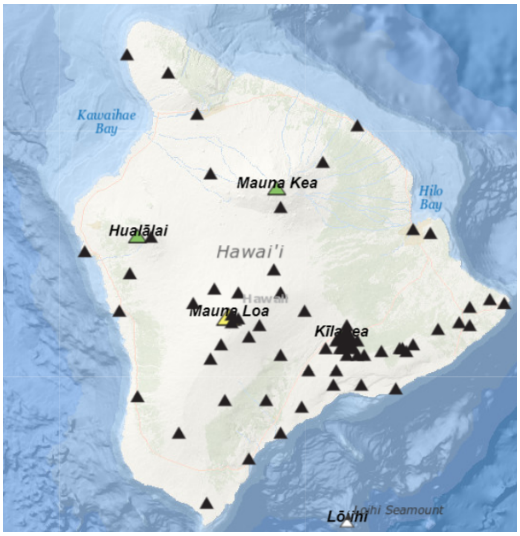

Figure 12: Map of the Big Island showing the locations of all seismographs (black triangles) as well as the summits of the volcanoes (colored triangles). Map obtained from HVO.

Seismic activity related to volcanism is divided into two categories: i) volcanic earthquakes caused by the brittle fracturing of rock by the pressure of magma forcing its way through the rock, or ii) tremors, caused by the movement of the resonance of the gas or magma itself as it rapidly rises to the surface or even the slow movement of the magma [Babb et al., 2011]. The subsurface location where an earthquake or tremor occurs is called the hypocenter, its projection on the surface is referred to as the epicenter. The timing, location and magnitude of the earthquakes and tremors have been recorded by the HVO and are used in this work as an independent set of observations to confirm the location of the inflation source. Additionally, the hypocenter data provide a more detailed time resolution when compared to gravimetry, InSAR, and GPS time-series. This time resolution can be used to narrow down the exact timing of events.

3.2 Surface deformation

It is well known that volcanoes deform in association with eruptive activity. Measurements of surface deformation can be performed by leveling, Electronic Distance Measurement (EDM), triangulation (also called tachymetry or total station measurements), and tilt measurements [Dzurisin, 2006]. This work uses tilt, GNSS and InSAR data to determine the ground deformation of Kīlauea volcano.

3.2.1 Ground observations

3.2.1.1 Tilt measurements

Tilt is the change in surface gradient with respect to a defined initial gradient. This change can be measured by tiltmeters which can record a change in surface gradient below 1 microrad or 1 mm elevation change over 1 km lateral distance. A sudden change in tilt can be the result of an earthquake whereas a gradual tilt change is indicative of subsurface processes such as magmatic inflation/deflation. Five electronic borehole tiltmeters, located at the summit, were actively recording during the 2015 event. The tilt meters are located in a borehole 3-6 meters deep encased in sand in order to be isolated from anthropogenic noise source. The location of these tiltmeters is shown in Figure 14.

The tilt measurements have a temporal resolution of 1 minute. This is much more than required to investigate the May 2015 event. Because of this, the data is reduced by decimation with an interval of 360 minutes. Meaning that only one out of every 360 measurements is used in the following analysis.

3.2.1.2 GNSS time series

GNSS measurements provide the only way to measure 3D displacement over time using one sensor. The GNSS sensor receives the signal from multiple GNSS satellites. This allows the sensor to compute its position relative to the reference ellipsoid. Changes in this position indicate displacement and/or deformation of the surface. The GNSS network on Kīlauea measures the North, East and Up components in the International Terrestrial Reference Frame 2000 (ITRF2000). Additionally, the NUVEL 1-A plate motion is removed from the GNSS positions, resulting in the pacific place reference frame, also seen as a reference frame local to Hawai'i [Baker and Amelung, 2012].

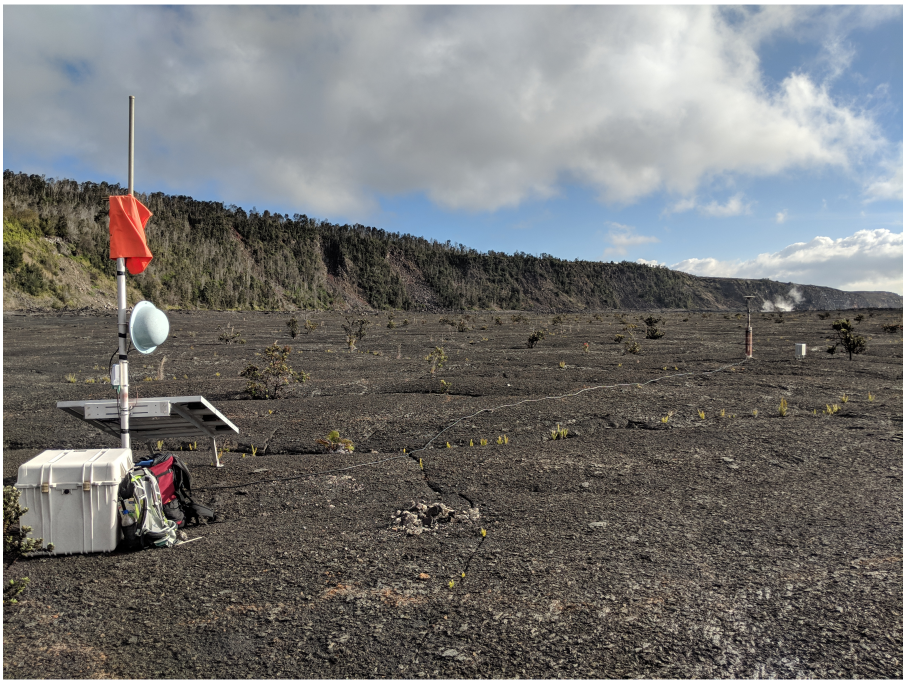

Figure 13: Picture of the BRYL GNSS station located on the eastern side of the Kīlauea summit caldera.

Eleven GPS stations located at the summit were active during the May 2015 event, Figure 13 shows one of those stations. Another one of those station, PUHI, was only active from the 15^{th} of May. The location of the GPS stations is shown in Figure 14.

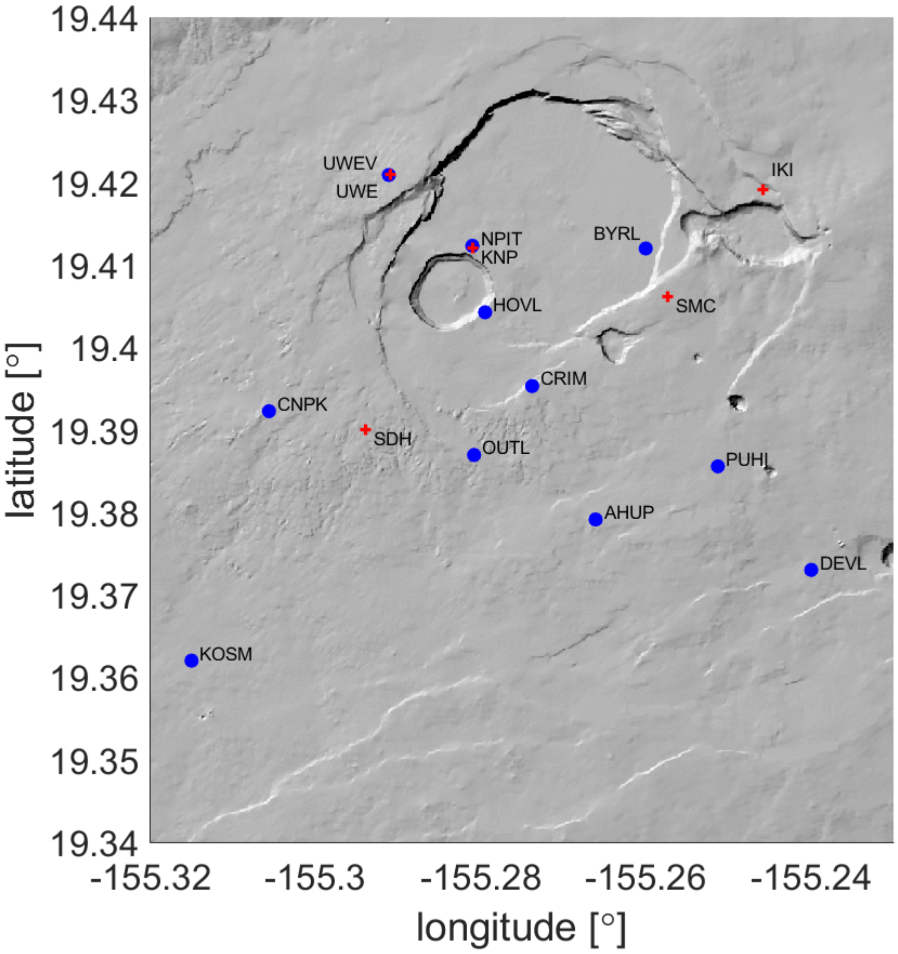

Figure 14: map of the Kīlauea summit area showing the location of tilt measuring instruments (red crosses) and GPS stations (blue circles). The names of the instrument locations is given by three-letter codes indicating tilt instruments and four-letter codes indicating GPS stations.

The GNSS time series data that is used has a temporal resolution of 1 day which is gathered by averaging the position over the day. This makes it hard to analyze time intervals of only a couple of days. Because of that, it is decided that for the GNSS time series, the periods from Summit inflation up to Southern caldera inflation are analyzed as one time period of the event. GNSS is also used in relation to InSAR to link the interferograms to the GNSS measured deformation. In those cases, the GNSS position at the dates of the interferometric pair are chosen.

Additionally, for the Free-Air Gradient correction needed in the micro-gravity analysis, 24 GNSS stations are used to calibrate the interferograms to the surface deformation as measured by the GNSS stations. A map of these station is found in Figure 15

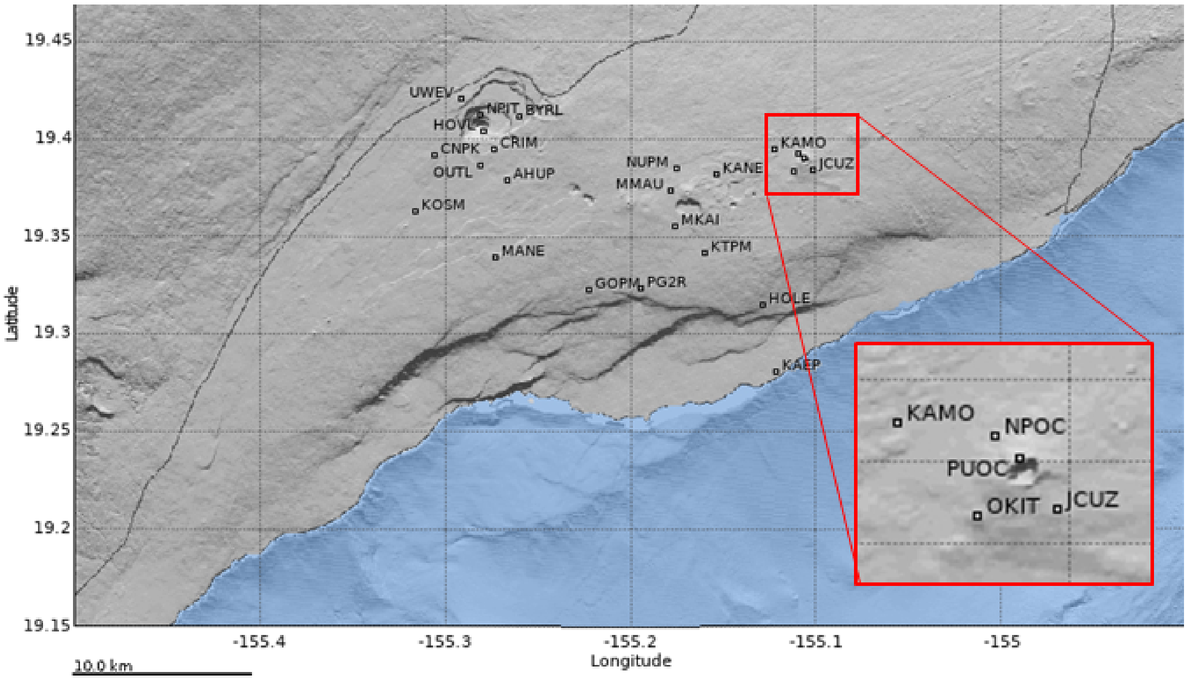

Figure 15: Map displaying the location of GNSS stations used for the Free-Air Gradient correction. Inset is shown for clarity.

3.2.2 Satellite observations

InSAR has proven to be a very effective tool for analyzing volcano deformation [Dzurisin, 2006]. It provides a few clear advantages over other measurement techniques. The primary advantage is that with InSAR the deformation of an entire area can be obtained whereas ground-based techniques can only obtain deformation of a few discrete points. Additionally, the use of InSAR data does not require the purchase, maintenance and replacement of instruments thereby avoiding the need for people in close proximity to the volcano and creating a safer working environment. The main disadvantages of InSAR are the poor time resolution compared to an instrument which measures continuously and the fact that deformation can only be measured in LOS direction which does not provide the same information as 3D deformation data. On top of that, deformation data obtained from interferograms are not necessarily referenced to a surface point with known deformation making it impossible to extract geo-referenced deformation data without consulting a-priori information about the deformation.

For this research, data from three different SAR satellites is used. For the Free-Air Gradient (FAG) correction needed in the micro-gravity analysis, three interferograms from CSK and one from TerraSAR-X (TSX) are used. These interferograms have been created, unwrapped and coregistered by Mike Poland from the USGS. More information on these interferograms can be found in Section 4.4.4. For analysis of surface deformation directly associated with the May 2015 event, data from the Sentinel-1a satellite is used. The SLC data was obtained from the ASF. Both ascending and descending acquisitions are used for the analysis. All SLC images are vertical-vertical (vv) polarized, meaning that the signal passes through a filter that vertically polarizes the radar signal both in sending and receiving the signal. The sentinel-1 acquisitions used were all taken in Interferometric Wide Swath mode. A list of all acquisition dates is presented in Table 3.

Table 3: Acquisition dates and baseline information of the Sentinel-1 data between 1st Jan 2015 and 31st Oct 2015 used in this research. (All dates are in yyyy-mm-dd format and according to Universal Time Corrected (UTC) time)

Ascending stack			Descending stack		
Acquisition dates	Perpendicular baseline (m)	Temporal baseline (days)	Acquisition dates	Perpendicular baseline (m)	Temporal baseline (days)
2015-01-06	0	0	2015-01-03	0	0
2015-02-11	191	36	2015-01-15	-197	12
2015-05-06	52	120	2015-01-27	-100	24
2015-05-18	85	132	2015-02-08	-154	36
2015-05-30	6	144	2015-02-20	-43	48
2015-06-11	62	156	2015-03-04	-108	60
2015-06-23	28	168	2015-03-16	-81	72
2015-07-05	85	180	2015-03-28	-162	84
2015-07-17	139	192	2015-04-09	-267	96
2015-07-29	71	204	2015-04-21	-241	108
2015-08-22	27	228	2015-05-03	6	120
2015-09-03	104	240	2015-05-15	-158	132
2015-09-15	133	252	2015-05-27	-75	144
2015-10-09	100	276	2015-06-08	-69	156
2015-10-21	92	288	2015-07-02	-15	180
			2015-07-14	-163	192
			2015-07-26	-68	204
			2015-08-07	-136	216
			2015-08-19	-159	228
			2015-08-31	-113	240
			2015-09-12	-126	252
			2015-09-24	-141	264
			2015-10-06	-136	276
			2015-10-18	-95	288
			2015-10-30	-87	300

Normally, the Sentinel-1 satellite would take an acquisition of the same area every 12 days. However, due to small changes in the orbit, the area that is visited can shift a bit along the orbit path. This is the main reason why some acquisitions, which should normally be 12 days apart, are missing. These missing images do not contain our region of interest. The outline of the used acquisitions is shown in Figure 16.

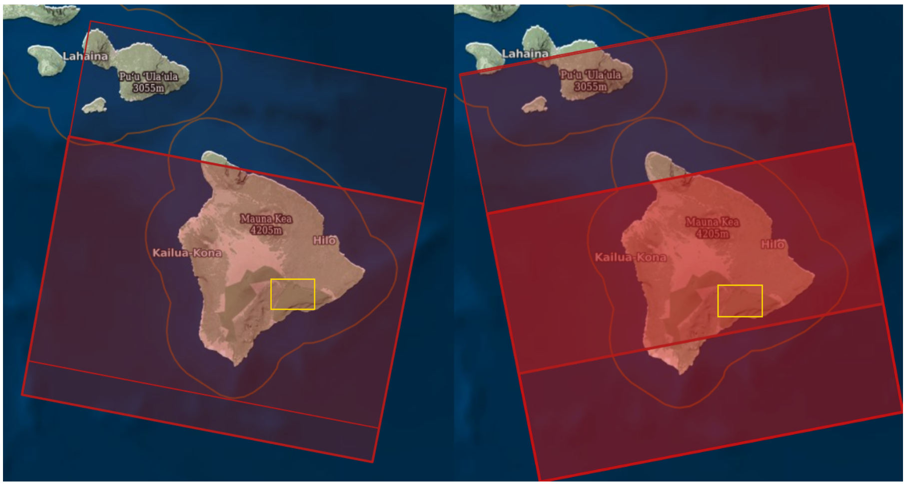

Figure 16: Ground-cover of the used Sentinel-1 acquisitions, split in descending acquisitions (left) and ascending acquisitions (right). The yellow rectangular box indicates the area of interest which is covered by both the ascending and descending image stacks. The ascending stack is composed of the available frames 58 and 60 of track 124 and the descending stack is composed of the available frames 525 and 527 from track 87.

Besides the difference in acquisition dates, the time of acquisition within a given data is also different for the ascending and descending orbits. The ascending acquisitions are taken at about 4:30 am UTC and descending acquisitions are taken at about 4:20 pm UTC. Converting this into the local time (Hawai'i Standard Time (HST)), we get 6:20 am HST for the descending stack and and 6:30 pm HST of the previous day for the ascending stack.

3.3 Visual observations

Kīlauea volcano is one of only a handful of volcanoes worldwide which, from time to time, houses a lava lake. Most recently the lava lake was present from 2008 to 2018. This 140 m by 220 m lake provides a direct insight into the magma reservoir that it is connected to. Variation in the pressure of the connected reservoir will lead to changes in the lava level. In the case of Kīlauea the lava lake is thought to be connected to the Halema'uma'u reservoir and small variations in the lava level correlate well with tilt measurements which have been used by Anderson et al. [2015] to estimate the size and location of the Halema'uma'u reservoir. These events are called Deflation-Inflation or DI events and are a common occurrence at Kīlauea with over 500 such events occurring between 2000 ad 2013 alone [Anderson et al., 2015]. However, it is not only pressure variation in the reservoir that leads to variation in the lava level. Patrick et al. [2016a] found that the lava level is also influenced by outgassing fluctuations.

Figure 17: Thermal camera positioned at the edge of the Halema'uma'u crater observing the lava lake. The edge of the Overlook crater, the crater which houses the lava lake within the Halema'uma'u crater is highlighted for clarity. Edited from Poland and Carbone [2016].

Figure 17 shows the thermal camera that measures the lava level by detecting sudden changes in the thermal response in a vertical band of pixels to find the edge of the crater in which the lava lake sits as well as the top of the lava lake itself. This crater is referred to as the 'Overlook crater'. The difference in pixels between the rim of the Overlook crater and the top of the lava lake is calibrated with less frequent laser range finding instruments and photogrammetry [Patrick et al., 2016b]. This measurement is then converted to meters above sea level.

3.4 Microgravity surveys

Relative gravity campaigns can be used to assess the gravity change due to changes in the subsurface mass distribution. The changes are also referred to as microgravity changes or just microgravity. Three such campaigns were performed in May/June 2012, October/November 2012, and September 2015. For each campaign, gravity was measured at about 50-55 locations. Two Scintrex CG-5 gravimeters were transported from benchmark to benchmark in a double loop pattern. One such pattern is shown in Figure 18.

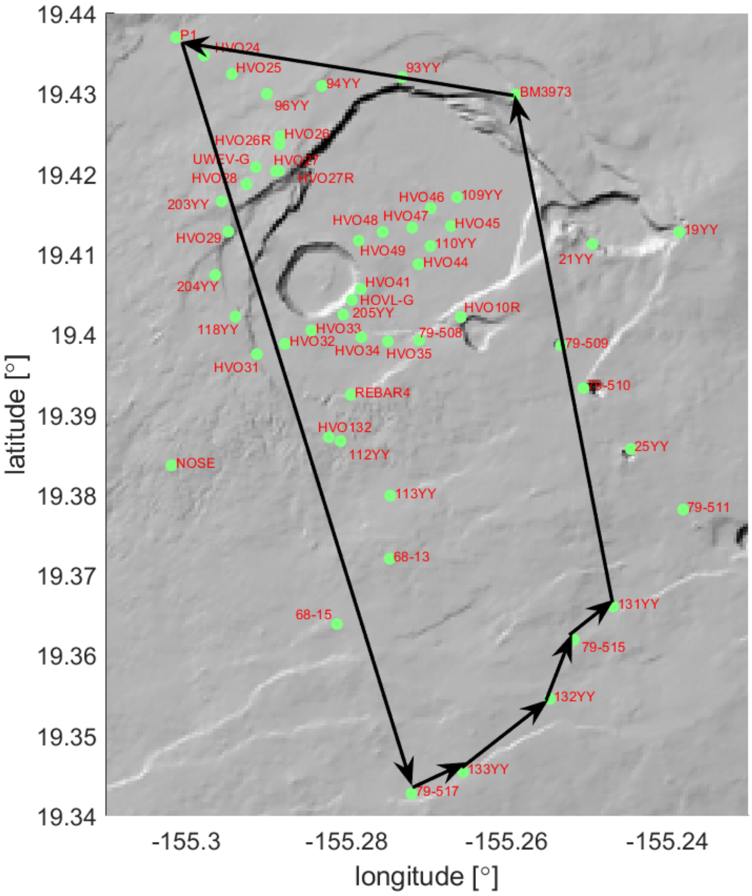

Figure 18: Map showing the location of the gravimeter benchmarks (green dots) and the double loop measured on November 5^{th} 2012 (black arrows). The same loop is measured twice in one session to ensure that each benchmark is visited two times and the base, P1, three times.

The double loop pattern and the use of two gravimeters allows to correct for tares in the data which can happen if the instrument is tilted by over 6° between measurements [Reudink et al., 2014]. The gravimeters measure the plumb line gravity component at a benchmark by completing five readings which each last 60-s. After the 5-min measurement session, the data is reviewed and if the variation about the mean is no more than 5 μGal, the data is kept and the instruments are moved to the next benchmark. However, if the readings do not settle towards a mean, or if the spread is more than 5-10 μGal, the readings were repeated until five consecutive 60-s readings met the criteria. This practice is common in microgravity surveys in volcanic areas [Battaglia et al., 2018; Poland and de Zeeuw-van Dalfsen, 2019].

4 Methods

Visual observations, seismic, deformation and microgravity data of interest were acquired from the HVO and InSAR data downloaded from the ASF. The InSAR and microgravity data require further processing, all other data can be visualized as they are. This chapter describes the methodology of the InSAR and microgravity data set beyond the information provided in Chapter 2. Starting with the InSAR deformation data and modeling in Sections 4.1 and 4.3, respectively. This is followed by a detailed description of the gravity data processing and modelling in Sections 4.4 and 4.5, respectively.

4.1 LOS offset

The acquisition dates of the ascending and descending stack are not the same. Therefore, a direct comparison between the individual interferograms is not possible. Especially the data gap in the ascending stack between 2015-02-11 and 2015-05-06 does not aid in the analysis of the surface deformation structure. The interferometric phase of the PS pixels is filtered according to the StaMPS method. This results in phase values per acquisition that are dominated by deformation with respect to the assumed zero deformation master acquisition. The time series of these phase values helps to understand the evolution of the deformation in the region. Figure 19 shows the time series of LOS displacement for 5000 PS pixels of the descending stack.

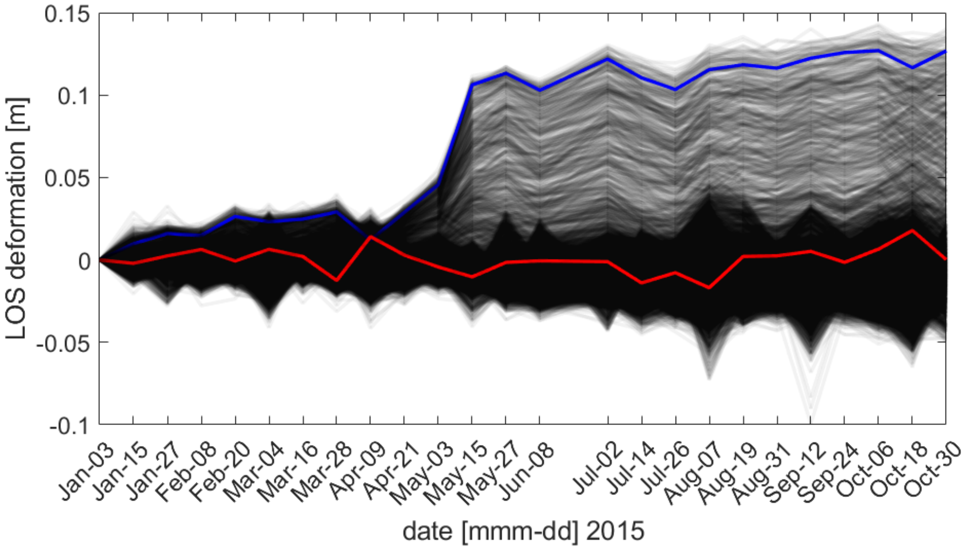

Figure 19: Time series of LOS deformation of 5000 PS pixels from the descending stack. Two time series of random pixels with differing deformation evolution have been highlighted in red and blue.

This analysis shows that most PS pixels behave similarly to the red highlighted pixel and have a roughly zero mean LOS deformation. However, a selection of pixels show a pattern more akin to the blue highlighted PS pixel. This latter set of pixels transition between two relatively stable periods over the period from April 9th to June 8th with varying amounts of total offset between the two stable periods. This offset can be estimated for each pixel since the transition period seems to be the same for each pixel. This estimation goes according to:

$$\begin{bmatrix} \hat{\varphi}_x^{zero} \\ \hat{\varphi}_x^{offset} \end{bmatrix} = (\boldsymbol{A}^T \boldsymbol{W} \boldsymbol{A})^{-1} \boldsymbol{A}^T \boldsymbol{W} \hat{\boldsymbol{\varphi}}_x^{def}, \tag{4.1.1}$$

where $\hat{\boldsymbol{\varphi}}_x^{def}$ is a vector containing the estimated unwrapped deformation phase of PS pixel x for all interferograms in the stack. The deformation phase is given by approximation (2.2.20). The estimated parameter $\hat{\varphi}_x^{offset}$ is the phase difference between the two stable states and $\hat{\varphi}_x^{zero}$ is the phase of the stable states compensated for the offset. Weight matrix $\boldsymbol{W}$ is the inverse of a diagonal matrix filled with the variance of the coherence of all PS pixels per interferogram. Design matrix $\boldsymbol{A}$ has the following from:

$$\boldsymbol{A} = \begin{array}{c} \\ \text{Stable} \\ \text{Period 1} \\ \text{Transition} \\ \text{Period} \\ \\ \text{Stable} \\ \text{Period 2} \\ \\ \end{array} \begin{bmatrix} 1 & 0 \\ \vdots & \vdots \\ 1 & 0 \\ 0 & 0 \\ \vdots & \vdots \\ 0 & 0 \\ 1 & 1 \\ \vdots & \vdots \\ 1 & 1 \end{bmatrix}. \tag{4.1.2}$$

This phase offset is converted to LOS displacement using equation (2.1.10). This estimation does not use the SM stack phase associated to the transition period. Thereby the only assumption that is made regarding the deformation is that all PS pixels have transitioned from one stable state to another and the offset is determined per pixel. The standard deviation of this offset is computed as the standard deviation of the model residuals for each pixel. The transition period is different for the ascending and descending stacks. The ascending stack has a transition period from 2015-02-11 to 2015-06-11 and the descending stack has a transition period from 2015-04-09 to 2015-06-08. The stable periods on either side of the transition still include these boundary dates. The initial stable period for the ascending stack only includes two acquisitions. This is primarily because there is no ascending acquisitions taken over Hawai'i between 2015-02-11 and 2015-05-06, when deformation had already started according to GNSS, tilt and the descending InSAR data stack. This research only uses the acquisitions taken by the Sentinel-1 satellite between 2015-01-01 and 2015-10-31. It might be possible to improve the phase offset estimation by extending the time period of interest to before 2015-01-01 and after 2015-10-31, assuming the stable periods remain stable beyond the time frame of interest to this research.

4.2 GNSS offset

The GNSS data is provided as a time series of displacement, much like the InSAR deformation phase time series. So as with the InSAR deformation, the displacement of each GNSS station from the first stable period to the second is computed. Only for the GNSS stations two columns are added to matrix (4.1.2) which include for the first stable period the time to the start of the transition and for the second stable period the time from the end of the transition. This allows for the estimation of the long-term velocity of the GNSS stations during the stable periods. The matrix for the calculation of GNSS offset and the velocities in the stable periods is given by:

$$\boldsymbol{A}_{GNSS} = \begin{array}{c} \\ \text{Stable} \\ \text{Period 1} \\ \text{Transition} \\ \text{Period} \\ \\ \text{Stable} \\ \text{Period 2} \\ \\ \end{array} \begin{bmatrix} 1 & 0 & t - t_{start} & 0 \\ & \vdots & \vdots & \\ 1 & 0 & t_{start} - t_{start} & 0 \\ 0 & 0 & 0 & 0 \\ \vdots & \vdots & & \\ 0 & 0 & 0 & 0 \\ 1 & 1 & 0 & t_{end} - t_{end} \\ \vdots & \vdots & & \\ 1 & 1 & 0 & t - t_{end} \end{bmatrix}. \tag{4.2.1}$$

Where t_{start} and t_{end} refer to the start and end times of the transition period, respectively. variable t is the time relative to the start or end time of the transition period for measurement having occurred before of after the transition, respectively. For each of the East, North and Up components of every GNSS station used the offset and velocities are calculated by:

$$\begin{bmatrix} \widehat{disp}_i^{stable1} \\ \widehat{disp}_i^{offset} \\ \widehat{velo}_i^{stable1} \\ \widehat{velo}_i^{stable2} \end{bmatrix} = (\boldsymbol{A}_{GNSS}^T \boldsymbol{A}_{GNSS})^{-1} \boldsymbol{A}_{GNSS}^T \boldsymbol{u}_i, \tag{4.2.2}$$

where $\boldsymbol{u}_i \in \{East, North, Up\}$ is the East, North or Up displacement time series of GNSS station i. Parameter $\hat{\boldsymbol{disp}}$ containing the estimated displacement value of stable period 1 and the estimated offset that occurred over the transition period, respectively. The East, North or Up velocity estimation of GNSS station i concerning the two stable periods is given by $\hat{\boldsymbol{velo}}$. The uncertainty of the displacement offset is set to be equal to the standard deviation of the residuals of the model compared to the displacement time series.

4.3 Volcano deformation source modelling using GBIS

With the use of the GBIS software - described in Chapter 2.4 - the sources of the surface deformation estimated by inverse modeling of the source parameters from the InSAR phase and GNSS offset data. Table 1 hints at the activity of two sources, one in the Summit caldera causing variation in radial tilt measurements and one towards the south of the caldera. A review of the magma storage areas of Kīlauea volcano as given by [Poland et al., 2014] would suggest these sources are the Halema'uma'u reservoir and the South Caldera reservoir.

4.4 Residual gravity estimation

There have been multiple relative microgravity campaigns to measure the gravity changes surrounding the Kīlauea summit [Bagnardi et al., 2014; Carbone et al., 2017]. Here we analyze, two campaigns in 2012 and one in 2015 shortly after the intrusion. For these measurements, two Scintrex CG5 relative gravimeters were used, their serial numbers ending in 578 (CG-578) and 579 (CG-579). These two instruments have previously and since been used to measure the relative microgravity changes at Mount Saint Helens, Washington [Battaglia et al., 2018], at Kīlauea, Hawai'i [Bagnardi et al., 2014; Carbone et al., 2017], and at Yellowstone NP, Wyoming [Poland and de Zeeuw-van Dalfsen, 2019]. The processing of the gravimetric data will follow a similar structure to that of Battaglia et al. [2012] with alterations made regarding the stochastic model. The processing steps are visualized in Figure 20.

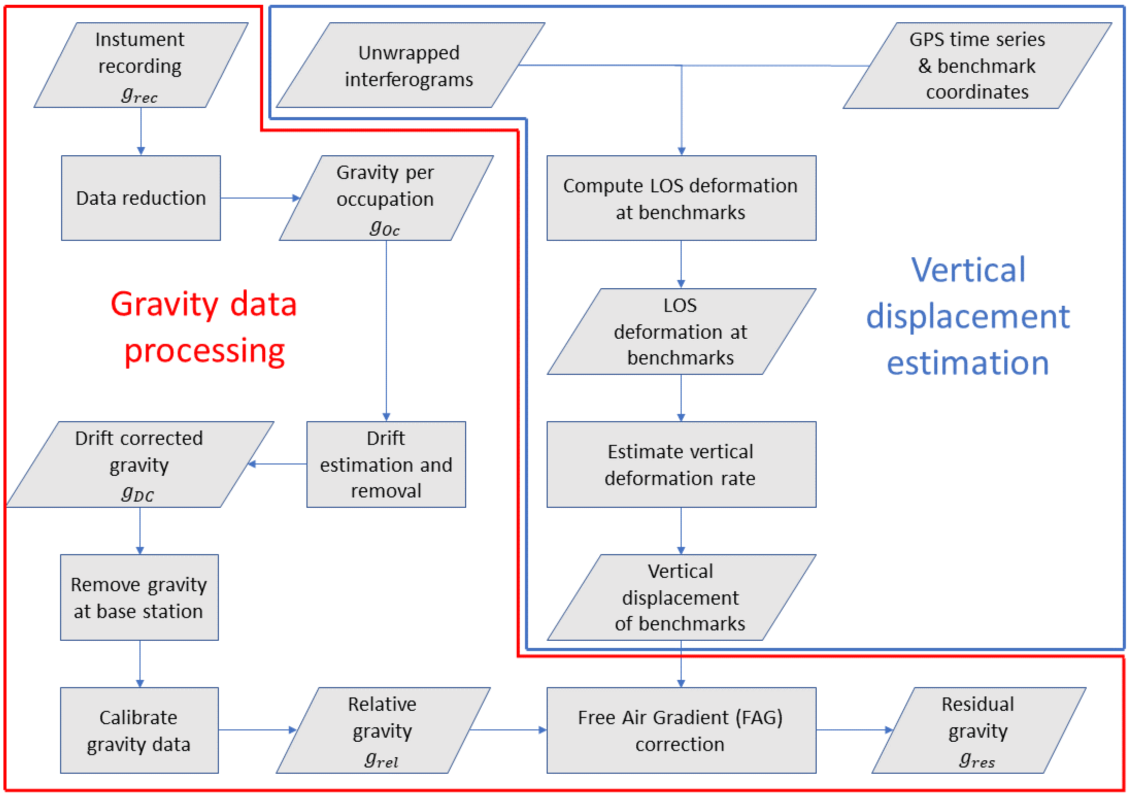

Figure 20: Flowchart of the gravimetric data processing chain. The flowchart is split in a gravity data processing chain (red) and a vertical displacement estimation chain (blue).

This chapter will follow the flowchart starting with the gravity data processing chain. The raw gravity data from the instrument has already been corrected for solid and ocean tide gravity signals which would otherwise dominate the recordings.

Besides that, the gravity signal from a single 60-s recording is comprised of the following contributions:

$$g_{BM}^{Re}(t) = g_{BM}(t) + g^{drift}(t) + noise. \tag{4.4.1}$$

The gravity reading $g_{BM}^{Re}(t)$ at benchmark BM is the summation of the gravity at the benchmark g_{BM} at time t, the contribution due to instrument drift $g^{drift}(t)$ and noise. The instrument drift is assumed linear over a time span of ¡ 1 day [Battaglia et al., 2018; Poland and de Zeeuw-van Dalfsen, 2019].

4.4.1 Gravity data reduction

If the gravity survey is done over a period of relatively low volcanic unrest, it can be assumed that over small time periods (1-10 minutes), the instrumental drift is neglectable since the drift rarely exceeds magnitudes of a couple of mGal per day. This removes the drift contribution from equation (4.4.1) only leaving the noise term which is assumed to be Gaussian distributed with zero mean. Doing multiple measurements of the gravity in such a small time frame allows us to perform a weighted average of these measurements to get a more accurate result of the gravity per occupation of the benchmark.

$$\hat{g}_{BM,i}^{Oc,j}(t_{i,j}) = \overline{g_{BM,i}^{Re,Oc,j} + noise}, \tag{4.4.2}$$

where $\hat{g}_{BM,i}^{Oc,j}(t_{i,j})$ is the weighted average gravity value at benchmark i during occupation j assigned to weighted average time $t_{i,j}$. All gravity readings of one occupation of a benchmark are given by $g_{BM,i}^{Re,Oc,j}$ with the line representing mean of the values. The values are weighted with the inverse square of the standard deviation of the gravity values measured during one 60-s reading.

4.4.2 Drift estimation and removal

The drift is assumed to be linear in time over the course of one double loop measurement sequence. For the drift estimation, first the gravity at each benchmark is estimated and removed from $\hat{g}_{BM}^{Oc}(t)$. This removes the gravity offsets between bases and only shows the contribution due to drift. The gravity at each benchmark is given by:

$$\underbrace{\begin{bmatrix} g_{Base,Oc_1} \\ g_{BM_1,Oc_1} \\ \vdots \\ g_{BM_n,Oc_1} \\ \vdots \\ g_{BM_N,Oc_1} \\ g_{Base,Oc_2} \\ g_{BM_1,Oc_2} \\ \vdots \\ g_{BM_n,Oc_1} \\ \vdots \\ g_{BM_N,Oc_2} \\ Base,Oc_3 \end{bmatrix}}_{\boldsymbol{g}_{BM}^{Oc}} = \underbrace{\begin{bmatrix} 1 & 0 & 0 & & \cdots & 0 \\ 0 & 1 & 0 & & \cdots & \vdots \\ \vdots & \ddots & \ddots & \ddots & & \vdots \\ 0 & \cdots & 0 & 1 & 0 & \cdots \\ \vdots & & & \ddots & \ddots & \ddots \\ 0 & & \cdots & & & 1 \\ 1 & 0 & 0 & & \cdots & 0 \\ 0 & 1 & 0 & & \cdots & \vdots \\ \vdots & \ddots & \ddots & \ddots & & \vdots \\ 0 & \cdots & 0 & 1 & 0 & \cdots \\ \vdots & & & \ddots & \ddots & \ddots \\ 0 & & \cdots & & & 1 \\ 1 & 0 & 0 & & \cdots & 0 \end{bmatrix}}_{\boldsymbol{B}} \underbrace{\begin{bmatrix} g_{Base,drift} \\ g_{BM_1,drift} \\ \vdots \\ g_{BM_n,drift} \\ \vdots \\ g_{BM_N,drift} \end{bmatrix}}_{\boldsymbol{g}_{BM,drift}}, \tag{4.4.3}$$

where $\boldsymbol{g}_{BM,drift}$ contains the gravity values per benchmark used for the drift estimation. The weighted least squares estimation is given by:

$$\hat{\boldsymbol{b}}_{BM,drift} = (\boldsymbol{B}^T \boldsymbol{W} \boldsymbol{B})^{-1} \boldsymbol{B}^T \boldsymbol{W} \boldsymbol{g}_{BM}^{Oc}, \tag{4.4.4}$$

with weight matrix W being a diagonal matrix filled with the inverse square of the standard deviation of $\boldsymbol{g}_{BM}^{Oc}$ as calculated in the previous section. The residuals are an estimation of the drift contribution according to equation:

$$\boldsymbol{g}^{drift} \approx \boldsymbol{g}^{Oc}_{BM} - \hat{\boldsymbol{b}}_{BM,drift}. \tag{4.4.5}$$

When combined with the time of measurement, this residual can be used to compute the drift rate δ. The drift contribution is of the from: $\boldsymbol{g}^{drift}(t_i) = \delta t_i + c$. where t,i is the weighted mean time assigned to $\boldsymbol{g}^{Oc}_{BM,i}$ and c is the drift value at $t = 0$. Before estimation of the drift rate, the mean of the time vector is removed. This minimizes the error in the drift correction due to the uncertainty of the drift rate. The drift contribution is estimated by:

$$\underbrace{\begin{bmatrix} g_{Base,Oc_1} - \hat{g}_{Base,drift} \\ g_{BM_1,Oc_1} - \hat{g}_{BM_1,drift} \\ \vdots \\ g_{BM_i,Oc_1} - \hat{g}_{BM_i,drift} \\ \vdots \\ g_{BM_N,Oc_1} - \hat{g}_{BM_N,drift} \\ g_{Base,Oc_2} - \hat{g}_{Base,drift} \\ g_{BM_1,Oc_2} - \hat{g}_{BM_1,drift} \\ \vdots \\ g_{BM_i,Oc_1} - \hat{g}_{BM_i,drift} \\ \vdots \\ g_{BM_N,Oc_2} - \hat{g}_{BM_N,drift} \\ g_{Base,Oc_3} - \hat{g}_{Base,drift} \end{bmatrix}}_{\boldsymbol{g}^{Oc}_{BM} - \hat{\boldsymbol{g}}_{BM,i,drift}} = \underbrace{\begin{bmatrix} t_{Base,Oc_1} - \bar{t} & 1 \\ t_{BM_1,Oc_1} - \bar{t} & 1 \\ \vdots & \vdots \\ t_{BM_i,Oc_1} - \bar{t} & 1 \\ \vdots & \vdots \\ t_{BM_N,Oc_1} - \bar{t} & 1 \\ t_{Base,Oc_2} - \bar{t} & 1 \\ t_{BM_1,Oc_2} - \bar{t} & 1 \\ \vdots & \vdots \\ t_{BM_i,Oc_2} - \bar{t} & 1 \\ \vdots & \vdots \\ t_{BM_N,Oc_2} - \bar{t} & 1 \\ t_{Base,Oc_3} - \bar{t} & 1 \end{bmatrix}}_{\boldsymbol{C}} \underbrace{\begin{bmatrix} \delta \\ c \end{bmatrix}}_{\boldsymbol{d}}, \tag{4.4.6}$$

where $\boldsymbol{g}^{Oc}_{BM} - \hat{\boldsymbol{g}}_{BM,drift}$ are the residuals between the gravity values per occupation of the benchmark and the estimated gravity at the benchmark used for drift estimation. The drift parameters δ and c are given in $\boldsymbol{d}$ which is estimated using the weighted least squares method of equation (4.4.4) only now with design matrix C instead of B and instead of the gravity values per occupation, their residuals. The same weight matrix is used. The uncertainty in the drift parameters (e.g. σ_δ and σ_c) is given by the square-root of the diagonal entries of the variance-covariance matrix of $\hat{\boldsymbol{d}}$. This matrix is computed by:

$$(\boldsymbol{C}^T\boldsymbol{W}\boldsymbol{C})^{-1}\boldsymbol{C}^T\boldsymbol{W}\boldsymbol{Q}_{res,res}\boldsymbol{W}\boldsymbol{C}(\boldsymbol{C}^T\boldsymbol{W}\boldsymbol{C})^{-1}, \tag{4.4.7}$$

where $Q_{res,res}$ is the variance-covariance matrix of the residuals (e.g. $\boldsymbol{g}^{Oc,j}_{BM,i} - \hat{\boldsymbol{g}}_{BM,i,drift}$). The estimated drift contribution is given by: $\hat{\boldsymbol{g}}^{drift} = \boldsymbol{C}\boldsymbol{d}$. An example of the estimated drift from CG5-578 on 2015-09-17 is given in Figure 21.

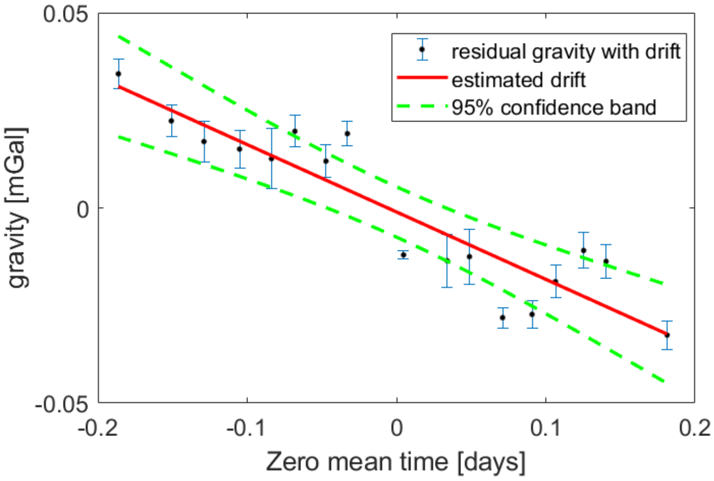

Figure 21: Drift estimation from CG5-578 on 2015-09-17. The residuals and their uncertainty are given in black, the estimated drift contribution is presented in red with the 95% confidence band indicated be the dashed green lines.

There is still observable deviation from the estimated drift. This could be due to nonlinear components in the remaining drift. for example, subtle changes in behavior of the instruments because of transport and use, imperfect temperature regulation of the sensor, and/or changes in the environmental conditions [Poland and de Zeeuw-van Dalfsen, 2019]. The estimated drift contribution is removed from $\boldsymbol{g}^{Oc,j}_{BM,i}$ and the values from all occupations of that benchmark over the double loop are averaged. This results in the drift corrected gravity or $\boldsymbol{g}^{DC}_{BM,i}$. The uncertainty of the drift corrected gravity is given by:

$$\boldsymbol{\sigma}_{\substack{DC\\BM,i}} = \sqrt{\boldsymbol{\sigma}^2_{g^{Oc,j}_{BM,i}} + \sigma_\delta^2 \cdot (t-\bar{t})^2 + \sigma_c^2}. \tag{4.4.8}$$

4.4.3 Relative gravity calculation

Two steps remain for the computation of the relative gravity. i) conversion of the drift corrected gravity to drift corrected gravity relative to the main base station, and ii) the calibration of the relative gravity values. In order to convert the drift corrected gravity values to drift corrected gravity relative to the main base station, the mean value of the gravity at the base station $\bar{g}^{DC}_{Base}$ is subtracted from the gravity values of benchmarks that were measured in a loop with the main base station.

In our case the main base station is 'P1' located a few km Northwest from the caldera (see Figure 18). Most benchmarks were measured in a loop with 'P1', however, in 2012 some station located on the caldera floor were measured from benchmark 'HVO41' instead. This was due to inconvenient and long travel times between those benchmarks and 'P1'. For these benchmarks the gravity value at 'HVO41', from when it was used as a base station, is subtracted and the gravity relative to 'P1' at 'HVO41' (taken from a different loop with 'P1'as the base station) is added to the relative gravity values such that each benchmark now has a drift corrected gravity value relative to 'P1'. The gravity value of 'P1' is set to 0 mGal.

The two gravimeters have been calibrated by the instrument manufacturers. However, an additional calibration of these instruments is performed by repeated occupations of three calibration lines: Mauna Loa (Hawai'i, USA), Mount Hood (Oregon, USA), and Mount Hamilton (California, USA) [Battaglia et al., 2018]. Battaglia et al. [2018] found, with the use of the method described by Valliant [1991], that a single scaling factor (0.99976 ± 0.00004 for CG-578 and 0.99935 ± 0.00003 for CG-579) can be used to adjust the gravity values of each gravimeter. The drift corrected relative gravity values are calibrated according to these constants resulting in $g^{rel}_{BM,i}$, the calibrated drift corrected relative gravity at benchmark i.

4.4.4 Estimate vertical displacement at gravimetry benchmark

To do the FAG correction, the vertical displacement at each benchmark between the two compared surveys need to be known. The only external information required is the height change at the measurement sites between the two campaigns. This can be achieved by co-locating the measurement locations with GNSS stations recording the vertical movement at that location. Alternatively, differential interferograms can be used to determine the vertical displacement of the benchmarks which do not have coincident GNSS time series [Bagnardi et al., 2014]. Even though there were multiple continuous GNSS stations active between 2012 and 2015, these are in most cases not co-located with a visited gravity benchmark. Therefore, the deformation of the area is estimated from the TerraSAR-X (TSX) and CosmoSky-MED (CSK) satellites which are X-Band SAR satellites that have been operational over the 2012-2015 interval.

Multiple interferograms with sufficient coherence are taken to estimate the vertical displacement rate. The information on the SLC acquisitions is presented in Table 4.

Table 4: Meta data for vertical correction InSAR Acquisitions.

satellite	asc/desc	master date	slave date	heading (°)	inc. angle(°)
CSK	asc	2012-11-08	2015-09-14	-10.525	38.77
CSK	asc	2012-09-21	2015-10-04	-10.525	38.77
CSK	desc	2012-09-12	2015-10-07	-169.60	41.34
TSX	desc	2012-10-25	2015-10-19	-169.44	31.17

The deformation rate is calculated because the interferograms span slightly different time intervals. Integration of this deformation rate through time will determine the total deformation that occurred between the gravimetry campaigns in 2012 and the campaign in 2015.

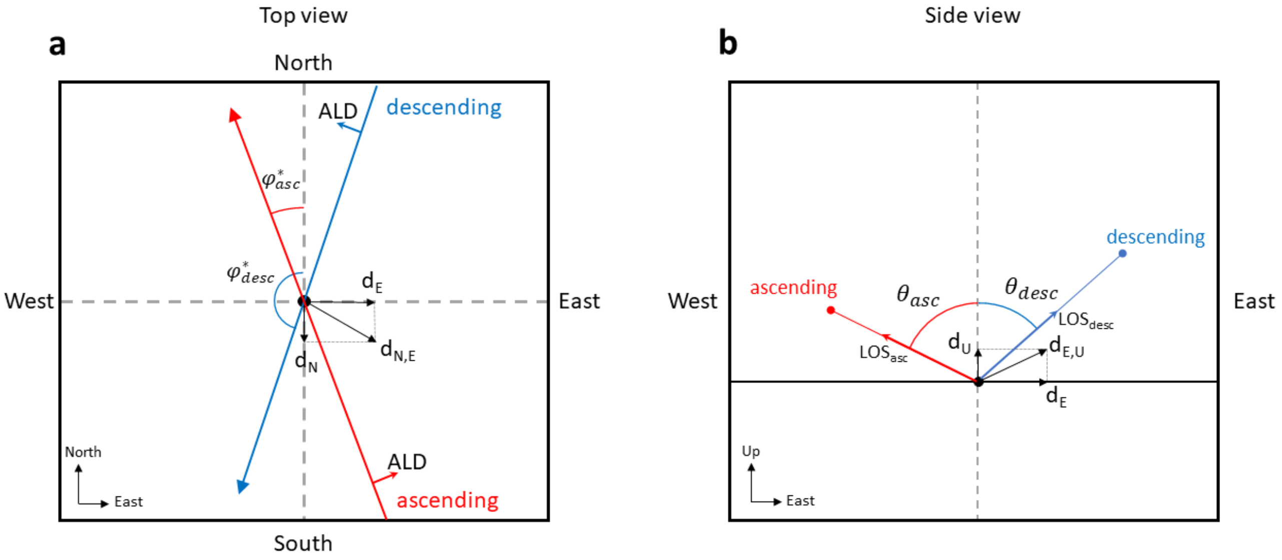

Figure 22: Geometry of 3D surface deformation estimation using SAR satellites. Right-looking satellites indicated by the Azimuth Looking Direction (ALD). The ascending and descending tracks are given in red and blue respectively. They have heading φ and incidence angle θ. Note that the heading is generally measured clockwise from North while the counterclockwise heading φ^* is visualized for clarity (for the calculation the heading as described by Table 4 need to be used). The deformation d of a surface point is decomposed in three principle directions (North, East, and Up). The measured LOS deformation is the projection of the deformation onto the LOS vector going from the surface point to the satellite. (Illustration by author, adapted from [Pepe and Calò, 2017])

Figure 22 shows the geometry of ascending and descending interferogram pairs needed to determine three dimensional (3D) deformation of a point on the surface. What is shown by the differential interferograms is the LOS deformation. Using both ascending and descending interferogram pairs allows for the estimation of the deformation along three principle directions. The LOS deformation relates to the geometry according to: (after [Pepe and Calò, 2017])

$$d_{LOS} = \boldsymbol{d} \cdot \boldsymbol{LOS} = d_{Up}\cos(\theta) + d_{East}\big(-\sin(\theta)\cos(\varphi)\big) + d_{North}\big(\sin(\theta)\sin(\varphi)\big), \tag{4.4.9}$$

with d_{LOS} as the projection of the deformation vector $\boldsymbol{d}$ onto the LOS direction $\boldsymbol{LOS}$. The deformation vector is composed of three components: d_{Up}, d_{East}, and d_{North}. The LOS deformation as presented by the interferograms are relative to a different point for each image. GPS time series from 24 stations on the Southern flank of Kīlauea are used to connect the interferograms to the measured displacement in the area. The displacement, between the interferogram acquisition dates, of the GPS stations is projected onto the LOS of the interferogram. Additionally, the LOS deformation of the interferograms is interpolated to the GPS locations. Then a single offset function is used to estimate the offset that needs to be applied to that interferogram according to:

$$d_{LOS}^{GPS} = d_{LOS}^{ifg} + c, \tag{4.4.10}$$

where d_{LOS}^{GPS} is the vector of LOS displacement of the GNSS stations, and d_{LOS}^{ifg} is the LOS deformation according to the interferogram. The offset parameter c is estimated using least squares estimation in order to correct every pixel of the interferogram by:

$$d_{LOS}^{ifg,new} = d_{LOS}^{ifg} + c, \tag{4.4.11}$$

with $d_{LOS}^{ifg,new}$ as the GNSS corrected LOS deformation of the interferogram. Figure 23 shows a visual representation of this correction.

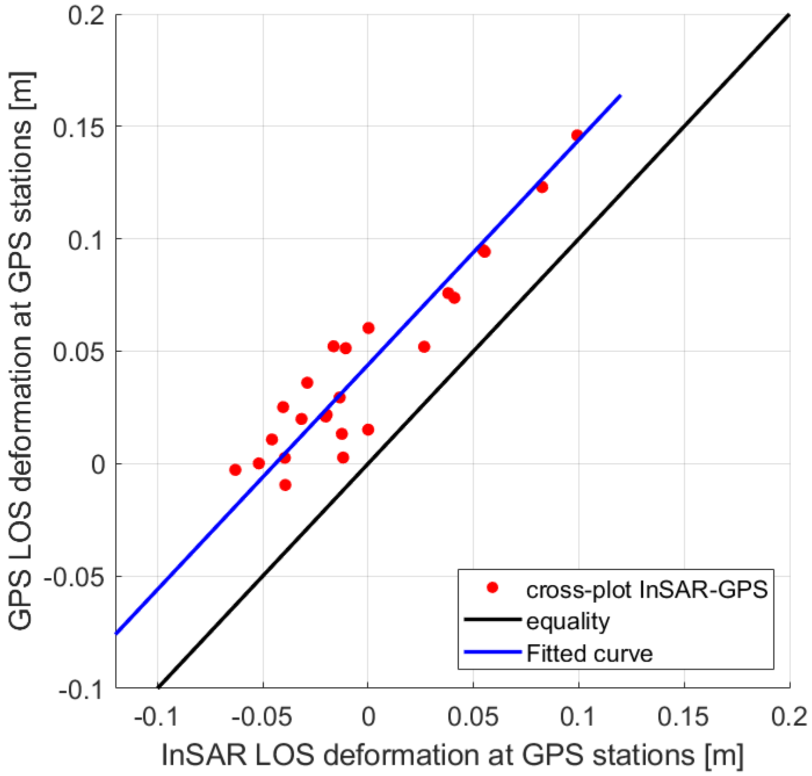

Figure 23: Cross-plot for the LOS displacement as given by InSAR (interpolated to the GNSS locations) and the LOS displacement as measured by the GNSS stations (red dots). The black line indicates equality and the blue line shows the correction function for the interferogram.

It is however, the deformation rate that we intend to estimate. This is done by dividing the total deformation over the time period in days (Δt):

$$E\left\{\frac{\partial d_{LOS}}{\partial t}\right\} = \frac{d_{LOS}}{\Delta t} = \frac{d_{Up}}{\Delta t}\cos(\theta) + \frac{d_{East}}{\Delta t}\big(-\sin(\theta)\cos(\varphi)\big) + \frac{d_{North}}{\Delta t}\big(\sin(\theta)\sin(\varphi)\big). \tag{4.4.12}$$

For each pixel in the interferograms, the LOS deformation rate is used to estimate the 3D deformation rate according to least squares estimation. The vertical component is then spatially interpolated to the gravimeter benchmarks and the free air correction is applied as:

$$g^n_{res} = \Delta^t g^n_{rel} - 0.3086 \cdot \Delta H^n, \tag{4.4.13}$$

with $\Delta^t g^n_{rel}$ as the relative gravity difference at benchmark n between two campaigns in mGal and ΔH^n the vertical displacement at benchmark n in meters.

4.4.5 Uncertainty in vertical displacement estimation

The uncertainty of the microgravity measurements themselves are roughly 10-15 μGal. Given that gravity changes approximately 3.086 μGal per cm, the uncertainty of the vertical displacement should not go beyond 3-4 cm. We calculate the vertical displacement from interferograms which were taken from different slave and master dates. The estimation of the deformation rate is most accurate if the deformation rate is approximately constant across the master date and slave date intervals. GNSS time series in the region show that the displacement rate was approximately constant during the slave date interval. However the displacement rate during the master date interval did not remain constant. This was due to inflation of the Halema'uma'u reservoir [Bagnardi et al., 2014]. Additionally, the interferogram deformation contains contributions due to atmospheric signal delay, orbit errors, elevation errors, unwrapping errors and errors introduced by interpolating the four interferograms onto the same grid. These error contributions increase the uncertainty of the estimated vertical displacement. Looking at Figure 23, the variation of the GNSS-InSAR cross-plot values (red points) about the corrected line (blue) is about 1.5 cm. Bagnardi et al. [2014] had similar results with the height observations from a single micro gravity survey at 1 cm bringing the uncertainty in height difference to 1.41 cm. Here we calculate the uncertainty in the deformation rate by computing the standard deviation of the residuals between the GNSS LOS displacement and the corrected interferogram LOS deformation and assigning this as the 1 σ uncertainty for the weighted least squares displacement rate calculation at the gravimetry benchmarks. The mean uncertainty in vertical displacement rate at the benchmarks is approximately $1.75 \cdot 10^{-5} {}^{m}\!/_{day}$. which , over the course of three years (2012-2015) becomes 1.9 cm uncertainty in the total displacement.

4.5 Mass point source modelling

For the mass point source model is, like the name suggests, a model of the gravity by mass addition in the subsurface from a point source for which the mass change, location and depth can be estimated. This is done by creating a minimization problem. The gravimeters can only measure the vertical gravity component. Thus the measured gravity change at point (x,y,z) due to a point source, located at position $(x_s, y_s, -d)$, is given by equation (2.3.2):

$$\Delta g(x,y,z) = \frac{G\Delta m(z+d)}{\left((x-x_s)^2+(y-y_s)^2+(z+d)^2\right)^{\frac{3}{2}}}. \tag{4.5.1}$$

Ignoring instrument noise and external factors, the gravimeter should measure this change exactly given the mass was added such that the center of mass of this added mass is located at $(x_s, y_s, -d)$. Note that there is the assumption that the volume of the mass change is approximately spherical or that the length scale of the volume is many times smaller than the distance to the benchmarks from which the relative gravity was measured. The value to minimize is the weighted sum of squared residuals. The residuals e are computed by: (adapted from [Heliker et al., 2003])

$$e_i(\Delta m, x_s, y_s, d) = \frac{G\Delta m(z_i+d)}{\left((x_i-x_s)^2+(y_i-y_s)^2+(z_i+d)^2\right)^{\frac{3}{2}}} - g_{res}(x_i, y_i, z_i). \tag{4.5.2}$$

These residuals are are a function of the unknown parameters and are weighted with respect to the variance values of the observations $\sigma_{g_i}^2$. These variance values form the diagonal of weight matrix $\boldsymbol{W}$.

The minimization problem, to estimate unknown parameter $\hat{\boldsymbol{x}} = \{\hat{\Delta m}, \hat{x_s}, \hat{y_s}, \hat{d}\}$, is formally expressed as:

$$\hat{\boldsymbol{x}} = \underset{\Delta m, x_s, y_s, d}{\operatorname{argmin}} \{f(\Delta m, x_s, y_s, d) = \boldsymbol{e}\boldsymbol{W}\boldsymbol{e}^T\}. \tag{4.5.3}$$

The minimization is performed by varying the unknown parameters Δm, x_s, y_s, and d. From an initial guess of these parameters. As an initial guess, the values provided by [Jo et al., 2015] are used. The initial guess of the mass change is given by the multiplying the volume change given by [Jo et al., 2015] with the average density of uncompressed magma 2600 ${}^{kg}\!/_{m^3}$ [Fujii and Kushiro, 1977]. The internal MATLAB function fminsearch is used to perform the minimization by way of the Nelder-Mead simplex algorithm as described by Lagarias et al. [1998]. This is the same method as used by [Bagnardi et al., 2014] in their analysis of the microgravity changes at Kīlauea from 2010 to 2012.

The gravity data available is from June 2012, October/November 2012 and September 2015. We are only interested in the May 2015 event, so for comparison between the 2012 and September 2015 surveys, a second point source is added at the depth and location of the Halema’uma’u reservoir as found by Bagnardi et al. [2014]. The mass change of this source is still estimated because the mass addition found by Bagnardi et al. [2014] might have continued between November 2012 and September 2015. Without gravity surveys between these two dates, we cannot guarantee the complete separation of these two events.

5 Results and implications

This chapter presents the results of the research and describes them in detail. The main attention is focused on the link between the observations and the characteristics of the May 2015 intrusion.

First, the seismic activity, tilt, lava level and GPS time series are discussed over the entire time period (January through August of 2015) and linked to the timing and evolution of the May 2015 event and where possible each of the stages as described previously in chapter 3. The subsequent subsections discuss each of the data sets separately. Data sets that are not suited to follow this approach such as InSAR deformation and micro-gravity will be discussed separately.

5.1 Time series comparison

According to observations and the initial data review by the HVO, the May 2015 event occurred between 2015-04-21 and 2015-05-18. Over this time period, the tilt and the lava level varied significantly (see Table 1). To get a better understanding of the activity and the evolution of the event, a time series comparison of Earthquake occurrences, selected GNSS and tilt stations, lava level and InSAR deformation is presented in Figure 24.

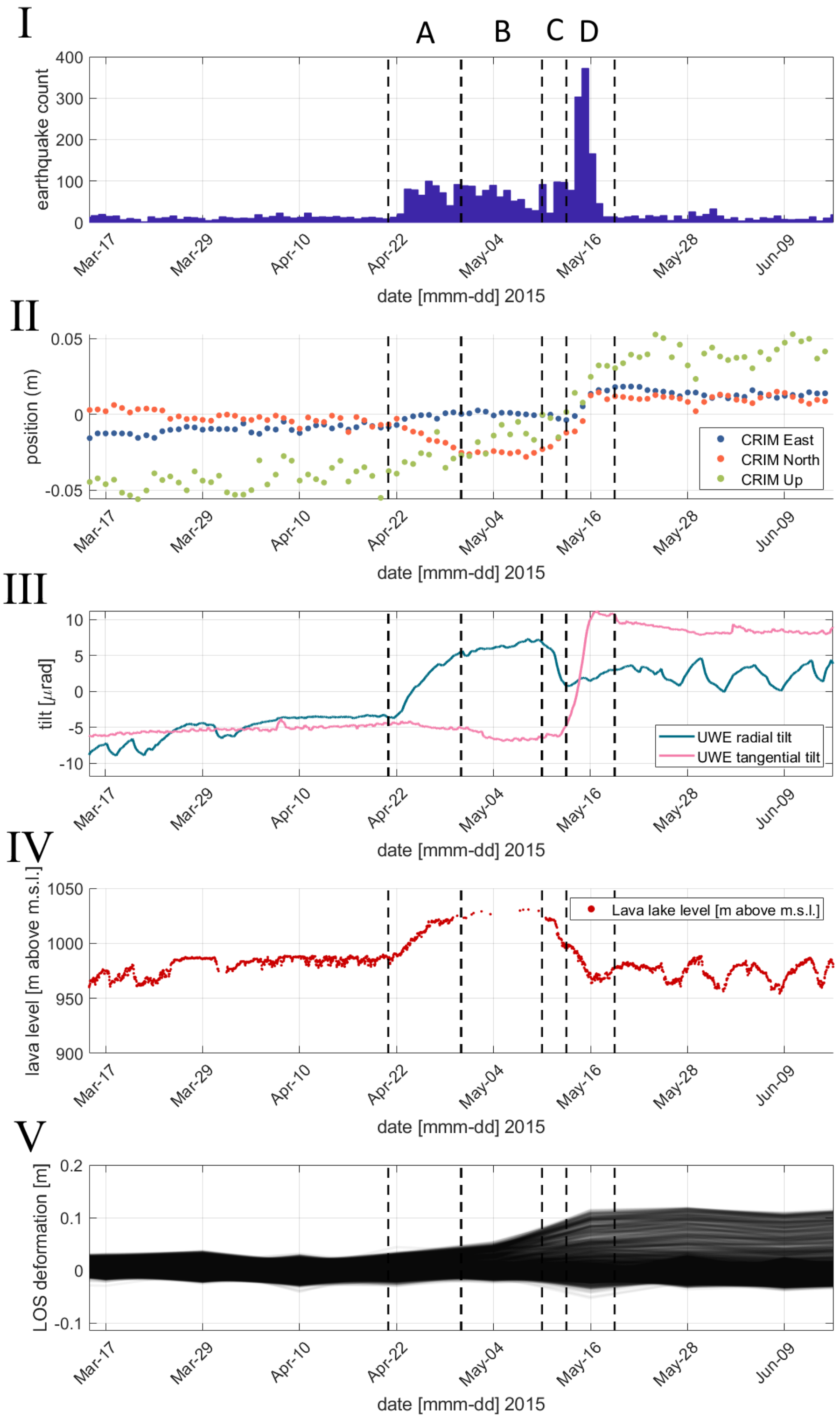

Figure 24: Time-series from 15-Mar-2015 to 15-Jun-2015 of a selection of data showing timing and evolution of the May 2015 event. I) Histogram of earthquake and tremor occurrences II) East, North, and Up position of the CRIM GNSS station. III) The radial and tangential tilt of the UWE tilt station. IV) Lava level above m.s.l. as measured by a laser ranging instrument. V) LOS displacement of 5000 randomly selected PS pixels of the descending InSAR stack. GNSS station CRIM is located approximately 1 km Southeast of the Halema'uma'u lava lake and tilt station UWE is located near the HVO building approximately 1.5 km North of the Halema'uma'u lava lake. Stages A though D are shown with vertical dashed lines

From top to bottom we see that the Earthquake activity was elevated over this period especially around 2015-05-15. Next we see that the GNSS station CRIM moved nearly 10 cm up from the beginning of stage A to the end of stage D. With movement towards the Southeast in stage A and to the Northeast during stage D. The UWE tilt station shows that the tilt in the region is already somewhat variable. The radial tilt is taken in the direction of the Halema'uma'u lava lake [Anderson et al., 2015] and it is set up in such a way that it reacts to changes in the HMMR and/or the lava lake. The radial tilt increases during stage A and drops during stage C, settling at a higher value that the start of stage A. The tangential tilt normally shows little variation but has a sharp increase during stage D. Hinting at activity originating from at least two different locations. The lava level of the Halema'uma'u lava lake also shows a clear high lava rise and fall over the four stages. The rise occurs primarily during stage A and the fall is split between stages C and D. The time series displacement of the PS pixels shown in Figure 24 E show that, over the same time period as the other plots, the area has deformed in the direction of LOS of the descending InSAR stack.

All of these time series indicate that the activity of the May 2015 event started around 2015-04-21 and ended some time around 2015-05-18. The radial and tangential tilt of the UWE station, the different displacement directions of the CRIM GNSS station and the distribution of earthquake occurrences through time over stages A to D show that at least two different phases can be identified during the May 2015 event.

5.1.1 Seismic activity

The seismic activity at the Kīlauea summit area is nearly always relatively shallow (depth $\leq$ 10km) and is mostly linked to activity of the magmatic system of the volcano. Other seismic activity is causes by tectonic movement, slipping of the Southern flank into the ocean or deeper magmatic processes related to the subsurface structure presented in Figure 3. Changes in seismicity are one of the primary indicators of subsurface movement of magma [Klein et al., 1987]. An analysis of the timing, depth, location and magnitude of the seismic activity might lead to an estimation of the location, size and evolution of an intrusion. The shape of a magmatic intrusion is linked to the sub-surface stress field [Fossen, 2016]. Sudden changes in the stress field by the release of built-up stress are expressed in tremors and earthquakes.

From Jan 1^{st} 2015 to August 31^{st} 2015 5852 earthquakes were recorded within the rectangular box bounded by corners 19.44° N,-155.40° E and 19.28° N,-155.15° E, of which nearly half occurred within stages A though D. This rectangular box (also the extend of Figure 25) is the area of interest for the seismic activity as it focuses on the Kīlauea summit area as well as the SWRZ and the Upper East Rift Zone (UERZ). It also includes the Southern flank which shows earthquake activity related to slipping of this flank towards the ocean. The Summit and the rift zones are proposed magma storage areas (see Figure 6) and seismic activity in these regions is most likely linked to volcanic unrest.

As shown in Figure 24 the background seismic activity is $<$10 earthquakes per day. The seismic activity stayed above this background level for the entirety of the May 2015 event. The highest rate of earthquakes recorded occurred on the 14^{th} and 15^{th} of May where over 350 earthquakes were recorded per day (more than 40 times higher than the background level). This activity is coincident with the Southern caldera inflation stage of the May 2015 event.

The histograms allow for a clear understanding of the timing of the May 2015 event. However the location of the event cannot be assessed from these histograms. To gain understanding on the prevailing locations of the earthquakes, a map with the density of earthquakes within the Mar 15^{th} and Jun 15^{th} 2015 time interval is shown in Figure 25.

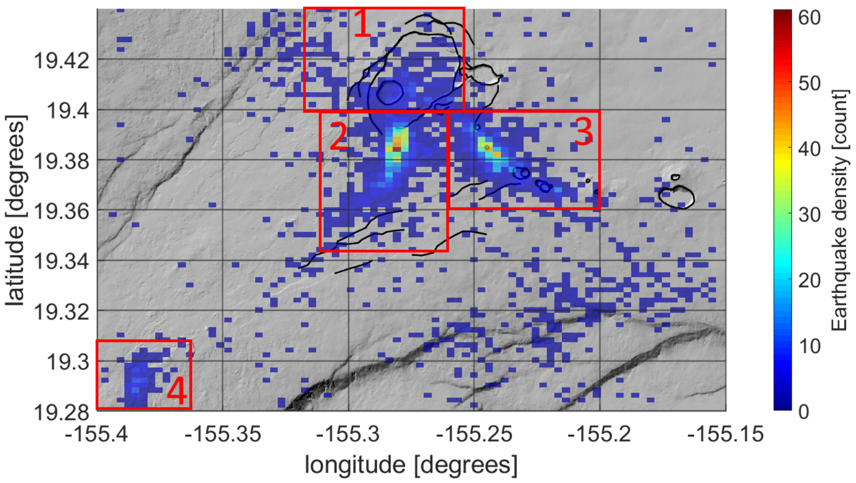

Figure 25: Map showing the density of the earthquake occurrences between Mar 15^{th} and Jun 15^{th} 2015 on a shaded relief map of the region with characteristic features highlighted in black. Four red boxes indicate regions with high seismic activity 1: Summit caldera, 2: Southern caldera and upper SWRZ, 3: Upper ERZ, and 4: Lower SWRZ (pu'ukou).

Analysis of Figure 25 shows the existence of four main regions where seismicity is significantly higher than the surroundings. These regions are highlighted in the figure. The earthquakes occur most often at the location of either a expected magma chamber (summit and Southern caldera), or the two rift zones. This indicates that volcanic processes are the likely cause of these earthquakes and tremors. Each of the four regions has the highest level of seismic activity at a different moment of the May 2015 event as shown in Figure 26.

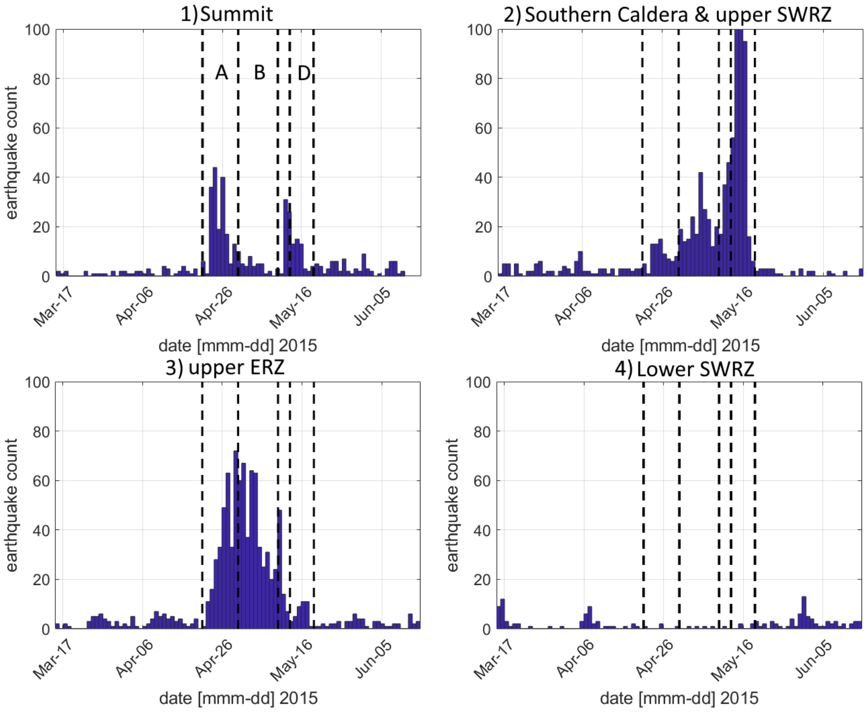

Figure 26: Histogram of the activity in 1) the summit caldera, 2) Southern caldera and upper SWRZ, 3) upper ERZ, and 4) lower SWRZ (pu'u kou). The stages of the May 2015 event are indicated with dashed black lines.

In the summit region, the seismic activity occurs primarily during stages A and C and correlate with inflation and deflation of the summit cladera, respectively according to the events listed in Table 1. The Southern caldera and upper SWRZ shows elevated activity throughout all stages, however, through stages C and D the number of earthquakes per day shoots up to 400 on May 15^{th} (off the scale) This coincides with inflation of the Southern caldera. The seismic activity in the upper

ERZ builds up during stage A and drops over the course of stage B and C. This activity falls neatly between the first spike in activity at the summit and the spike in activity in the Southern caldera /upper SWRZ. The lower SWRZ shows almost no activity during the May 2015 event. However, several weeks after the May 2015 event, around May 30th there was a small spike in activity. According to Poland et al. [2014] The activity of the Pu'u kou region is not associated with intrusions in the SWRZ and the Pu'u kou region is generally seismically active. The SWRZ stops just short of this region. If magma had flowed all the way down the SWRZ it would have past the KOSM GNSS station which shows no significant displacement between the end of stage D and the May 30th.

It is clear that the most significant seismic activity occurred on 14 and 15 May 2015 in the Southern caldera and upper SWRZ region. looking at Figure 25 we can see that the activity is centered around the Southern caldera with a tail leading into the upper SWRZ. The depth of the earthquakes and tremors can be used to identify the subsurface sources of activity. The depth of seismic activity is assessed by making a time-depth density plot which shows the density of earthquake and tremor occurrences over time and depth.

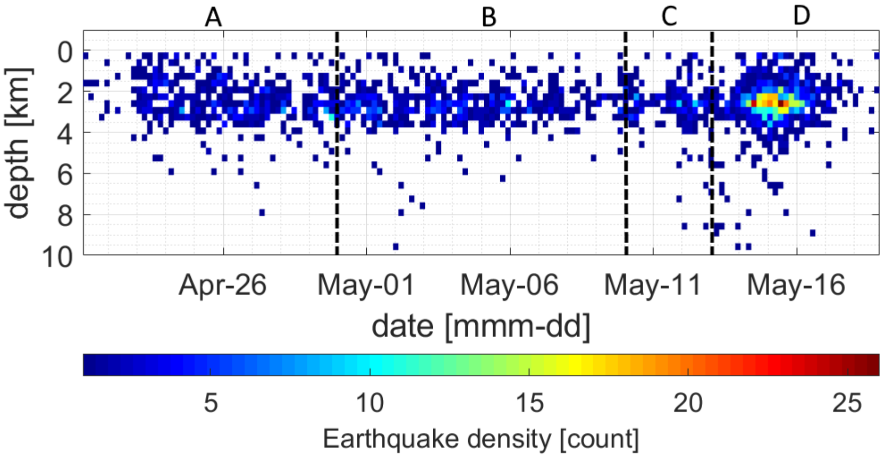

Figure 27: Time-depth density plot from Apr 21st to May 18th. The dashed black lines indicate the stages as indicated by the letter above each section.

Figure 27 shows us that nearly all of the activity occurred between 2 and 5 km depth. The peak of seismic activity during stage D (which took place in the Southern caldera) is highest at a depth of approximately 2.6 km. At the start of stage A we see slightly more earthquakes occur between 0 and 2 km depth than in stages B and C. This is also the period of lava level rise (see Figure 24. The lava level dropped during stage C where, especially on the 12th of May 2015 we see seismic activity ranging from the surface to about 4 km depth. This activity seems to reflect the movement of magma away from the HMMR toward greater depths causing seismic tremors.

5.1.2 GNSS

As mentioned in Section 3.2.1 the GNSS position is computed once per day for multipe stations around the summit of Kīlauea volcano. Figure 28 shows the displacement of GNSS stations CRIM and CNPK. The CRIM GNSS station is located about 1.5 km Southeast of the lava lake and the CNPK GNSS station is located approximately 3 km Southeast of the lava lake (see Figure 14). Both stations show a clear response to the different stages of the May 2015 event.

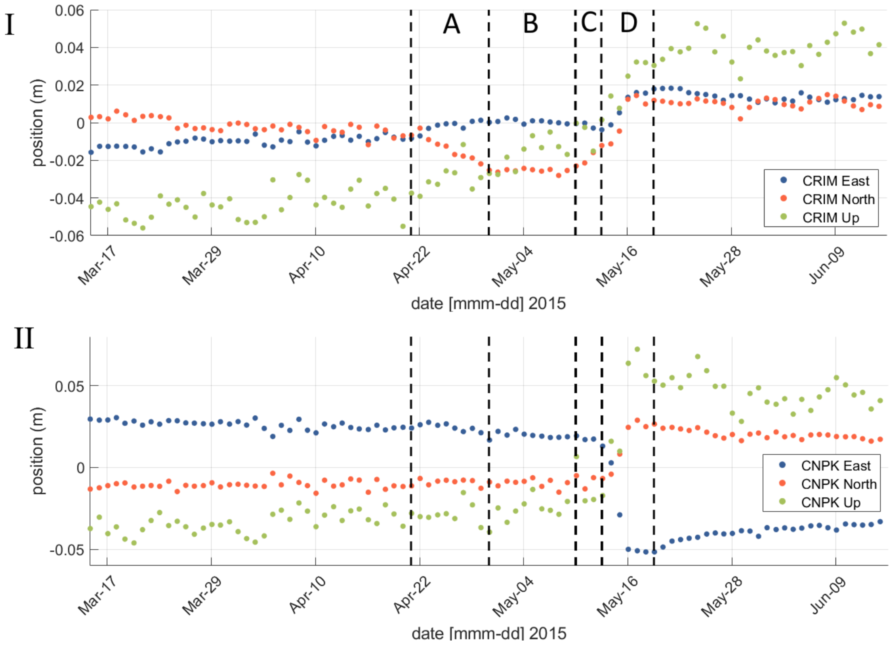

Figure 28: Displacement of I) the CRIM GNSS station and II) the CNPK GNSS station. The displacement is separated in three orthogonal components: East, North and Up. The stages of the May 2015 event are separated by dashed black lines.

The CRIM station is located just south of the Halema'uma'u vent and generally moves towards the Southeast. This is caused by the fact that the Southern flank of the volcano slowly slips into the ocean combined with the general inflationary trend of the Kīlauea summit. Tectonic plate movement has been removed for the GPS displacement measurements [Baker and Amelung, 2012]. During stage A of the May 2015 event, the CRIM GNSS station moved towards the South by 2.5 cm. There is also movement toward the east of about 1 cm and the station has moved up by about 1.5 cm. This coincides with the increase of radial tilt of the UWE tilt station and a rise in lava level (see Figure 24) as well as movement away and up from the lava lake as observed by GNSS station CRIM. The same GNSS station only uplifts another 2 cm during stage B. In stage C we see an inversion of the movement from stage A, now moving towards the lava lake. The CRIM GNSS station is located on the other side of the Halema'uma'u crater from the UWE tilt station and moves away from the lava lake, just like the UWE tilt station tilts away from the lava lake during stage A and both move/tilt toward the lake during stage C. This indicates that the source of this movement lies roughly in between these two stations, exactly where both the lava lake and the HMMR are located.

GNSS station CNPK does not move much during stages A though C, however, during stage D the station is moved significantly towards the WNW while also being uplifted by 7-8 cm over the same period. GNSS station CRIM is moved toward NE during this stage and is uplifted by approximately 3 cm. According to Table 1 this is most likely related to the inflation of the Southern caldera region. If the movement of the GNSS stations is caused by inflation, they move radially outward from the center of inflation. Uplift decreases further from the source as displacement is shifted from upward to laterally outward from the source. Assessing the displacement pattern of the GNSS stations indicated in Figure 14 we are able to assess whether the pattern resembles that due to inflation. The displacement rate of the GNSS stations in the summit region is shown in Figure 29.

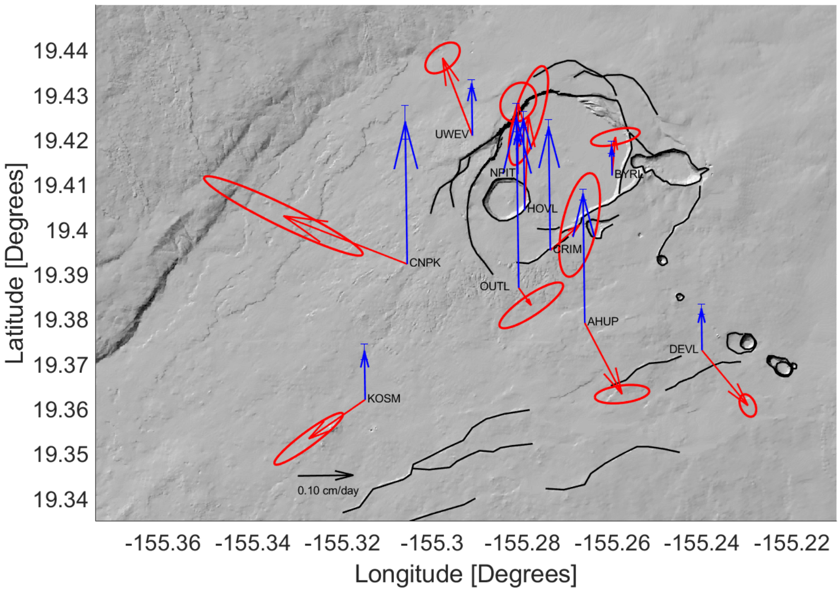

Figure 29: Displacement rate map from GNSS stations near the summit and southern caldera from April 21st to May 18th. The red arrows show the horizontal displacement rate with their 95% confidence ellipses. The blue arrows indicate the vertical displacement rate with the error bar at the top of the arrow indicating it's 1σ uncertainty.

All stations at the Kīlauea summit have moved outwards from the southern caldera during the May 2015 event. Additionally, in the southern caldera the uplift is highest and tapers off with distance from this region. From the OUTL station, which is located near the center of the Southern caldera, we observe that the lateral movement is significantly smaller than that of station CNPK. This is exactly what would be expected as displacement pattern caused by a growing upside-down bowl. Figure 29 shows the displacement signal for stages A through D. The movement that occurred during each of the stages is different. Recreating Figure 29 for the individual stages will unveil the deformation pattern of each stage. Figure 30 shows the GNSS displacement rate pattern for each of the stages.

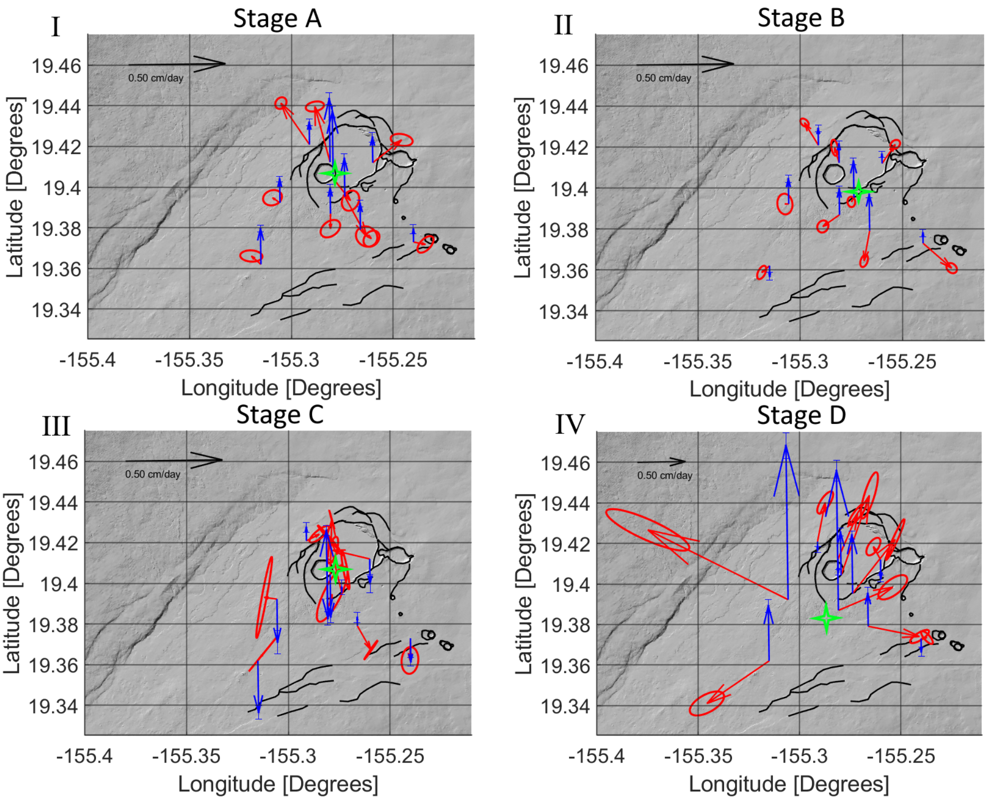

Figure 30: Displacement rate estimation of each stage. The horizontal displacement is given by the red arrows and their 95 % uncertainty ellipses. The vertical displacement is given by the blue arrows with have 1 σ uncertainty. The green four-pointed star in each of the maps indicates the visually estimated center of inflation/deflation. Note that the scale of the arrows is halved for stage D because of the significantly larger displacement rate.

The spatial pattern of displacement for each of the stages separately also resemble inflation/deflation bowls. For stages A, B and D the stations have moved up and away from the green star indicating inflation centered around the star. During stage C, the stations moved down and toward the star indicating deflation. The pattern of stage C is less clear than that of the other stages. This is partly because of the overlapping inward pointing arrows and partly because the displacement rate estimation over the 3 day duration of the stage is prone to short time scale signals in the noise. The location of the green stars shows that the inflation center of stage A is in the same location as the deflation center of stage C. This location on the East side of the Halema’uma’u crater rim is the proposed location of the Halema’uma’u reservoir [Cervelli and Miklius, 2003; Baker and Amelung, 2012; Bagnardi et al., 2014; Poland et al., 2014; Anderson et al., 2015; Patrick et al., 2015; Jo et al., 2015; Wauthier et al., 2019]. The Halema’uma’u reservoir is the most likely source of the inflation during stage A and the deflation during stage C. During stage B the inflation is centered around a point roughly 1.5 km Southeast of the lava lake, close to the CRIM GNSS station. This is the proposed location of some magma storage area [Baker and Amelung, 2012]. The location matches particularly well with the proposed Keanakāko’i reservoir in Poland et al. [2014]. The inflation center of stage D is located in the Southern caldera region and the displacement rate during this stage is significantly higher than that of the other stages. Inflation of the Southern caldera reservoir would result in such a displacement pattern and is therefore the likely source of inflation during this stage. The centers of inflation/deflation also correlate with increased seismic activity around that location (see Figure 26) The inflation center of stage B is located between the Southern caldera region, the summit, and the upper ERZ. The upper ERZ, southern caldera region, and to a lesser extend the summit all were seismically active during this stage, so possible magma movement in these regions could have contributed to the observed displacement pattern.

5.1.3 Tilt

Tilt is measured at multiple locations surrounding the Kīlauea summit. Two stations in particular, the UWE and SDH stations, show a clear response to the multiple stages of the May 2015 event. The SDH tilt station is located approximately 1.2 km Southwest from the Halema’uma’u lava lake on the Western edge of the Southern caldera region (see Figure 14). The tilt measurements of station UWE and SDH are shown in Figure 31

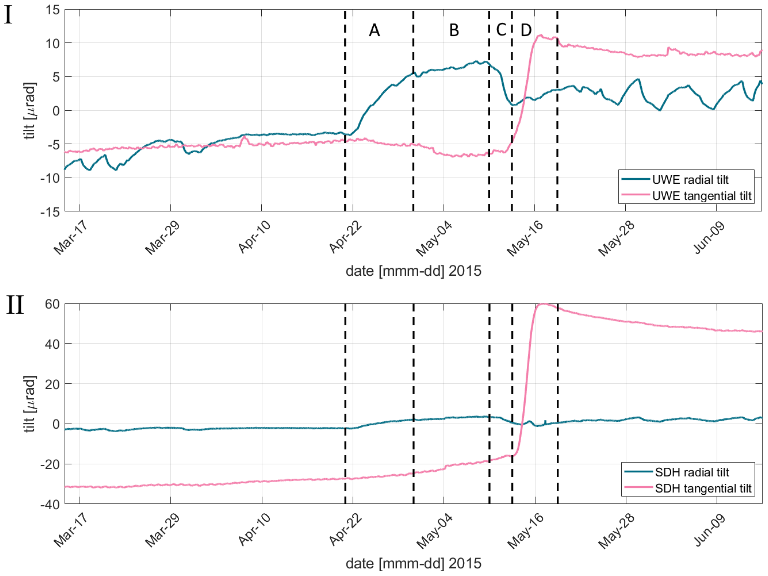

Figure 31: Radial and tangential tilt of I) the UWE tilt station and II) the SDH tilt station. The stages of the May 2015 event are separated by dashed black lines. Note that the vertical scale is different for each station.

Most of the stages of the May 2015 event are described by the inflation or deflation of certain regions. The tilt instruments are oriented such that the radial tilt is positive when the summit caldera inflates. This is clearly observed in the radial tilt of the UWE station during stage A, stage C shows an decrease of radial tilt indicating summit caldera deflation. Before and after the May 2015 event, the UWE radial tilt shows several saw tooth like patterns. These are Deflation-Inflation (DI) events which have been linked to pressure changes of the Halema'uma'u reservoir and the movement of magma to or from this reservoir [Anderson et al., 2015]. The radial tilt of the SDH station also shows inflationary tilt during stage A and deflationary tilt during stage C but the amount of tilt is significantly smaller compared to the UWE station. This indicates that the UWE station is closer to the source of inflation and deflation of stages A and C compared to the SDH station. This behavior of the radial tilt is exactly as expected from inflation/deflation as indicated in Figure 30. The tangential tilt of both stations shows a significant increase during stage D. Outside of this stage, the tangential tilt shows little to no response to the activity. This indicates that the activity of stage D happened at a different location compared to that of stages A and C which happened at roughly the same location. While the radial tilt of the UWE station was much higher than that of the SDH station, the reverse is true for the tangential tilt. The tangential tilt of the SDH station increases by about 75 μrad whereas this is only 16 μrad for the UWE station. This tells us that the source of this tilting is closer to the SDH station than the UWE station. The tangential tilt of the SDH station is measured as positive if the downward gradient towards the Northwest increases. This means that the source of inflation is towards the Southeast of the SDH tilt station. This again lines up with the inflation center of stage D as indicated by Figure 30.

5.1.4 Lava level

The lava level at the Halema'uma'u vent fluctuated significantly during the May 2015 event as evidenced by the observations made by the HVO in Table 1. The lava level data can give useful information as to how the changes at the surface are linked to the storage system of the volcano. The variation of the lava level has already been shown in Figure 24, but a closer look at the variation that occurred just over the time span of the may 2015 event might reveal more details.

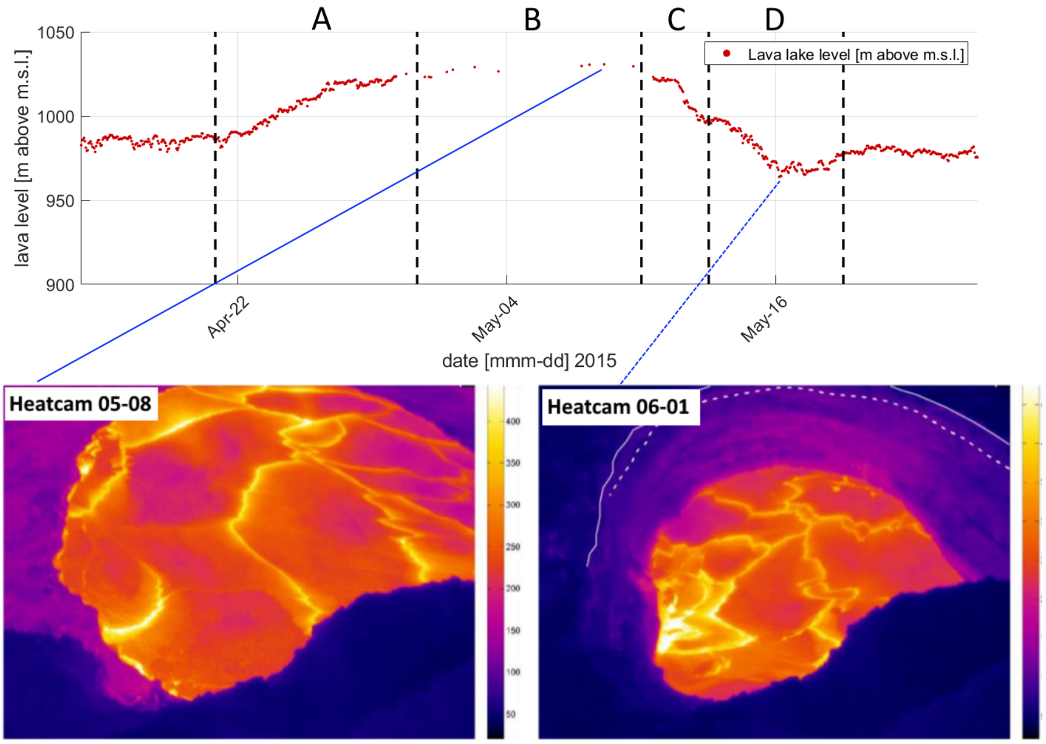

Figure 32: Lava level variation from 15-04-2015 to 25-05-2015. The stages of the May 2015 event are separated by dashed black lines. Two images from the thermal camera are shown: May 8th 2015 (left) and June 1st 2015 (right) which had a comparable lava level to May 16th 2015. The images are related to the time series by the blue lines. The thermal camera images are obtained from the HVO with consent from M. Poland (USGS).

Figure 32 shows that data is sparse during stage B this might be because at times when the lava lake is at the edge of the overlook crater, the edge detection software used to detect the top of the lava lake and the rim of the overlook crater cannot detect two edges, but only one. This results in a non-measurement. Alternatively, Fumes from the lava lake could have obscured the view of the thermal camera, equally resulting in a non-measurement. From visual observations it is known that the lava level during stage B remained within several meters of the overlook crater, overflowing multiple times (see Table 1).

The lava level drops about 20 meters in a single day during stage C and remains just below 1000 m above m.s.l. for approximately one day. Then in stage D the lava level drops a further 30 meters in about 2 days. The lave level correlates very well with the radial tilt of the UWE station. This is specially clear in Figure 24 where the DI event shown in the radial tilt have a near one-to-one correspondence to lava level variations. This second drop in lava level during stage D is not present in the radial tilt of the UWE station. However, the second drop does have an anti-correlation with the the increase of tangential tilt of both the UWE and SDH tilt stations. This suggests that the first drop is related to the deflation of the summit whereas the second drop is related to the inflation of the Southern caldera.

5.2 InSAR deformation

5.2.1 Individual interferograms: a snapshot of deformation

In contrast to continuous GNSS and tilt which measure the deformation at one location per instrument, InSAR data is taken over a much broader area visible to the satellite as it flies over. This allows for the assessment of deformation over the entire area of interest. Single interferograms provide an insight into the deformation between the two passes. In areas where deformation is significantly large it will dominate the interferometric phase and can be used to assess the location and spatial pattern of deformation. The periods of deformation described in Table 2 do not perfectly overlap with the acquisitions of the InSAR satellite given in Table 3. However, some image pairs do roughly align with these stages. Figures 33 and 34 show the deformation signal captured by the individual interferograms over the May 2015 event.

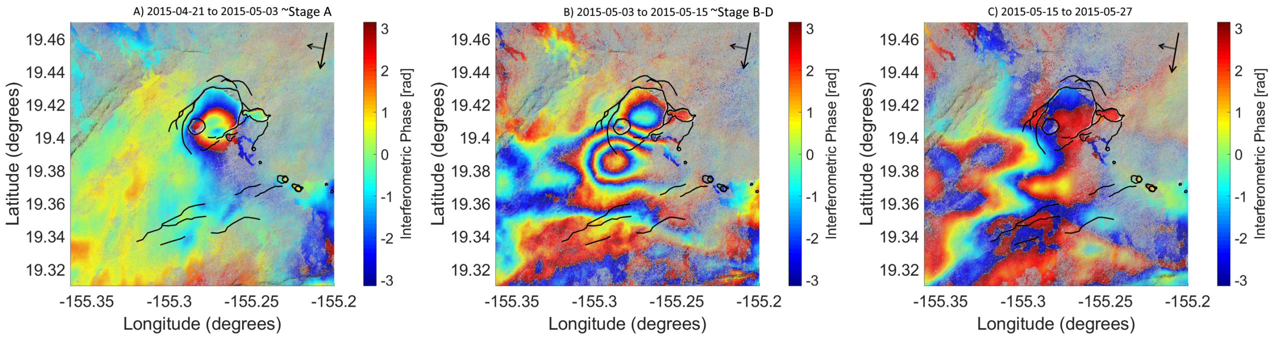

Figure 33: Individual wrapped interferograms from the descending orbit over period, A) 2015-04-21 to 2015-05-03 (roughly aligned with stage A), B) 2015-05-03 to 2015-05-15 (a combination of stages B-D), and C) 2015-05-15 to 2015-05-27 (after the major deformation). The transparency of the interferometric phase is scaled to the coherence value of each pixel. Each cycle of the phase corresponds to 2.8 cm LOS deformation. The flight direction and looking direction are indicated by the black arrows in the top right corner of each interferogram. Characteristic surface features of the volcano have been highlighted.

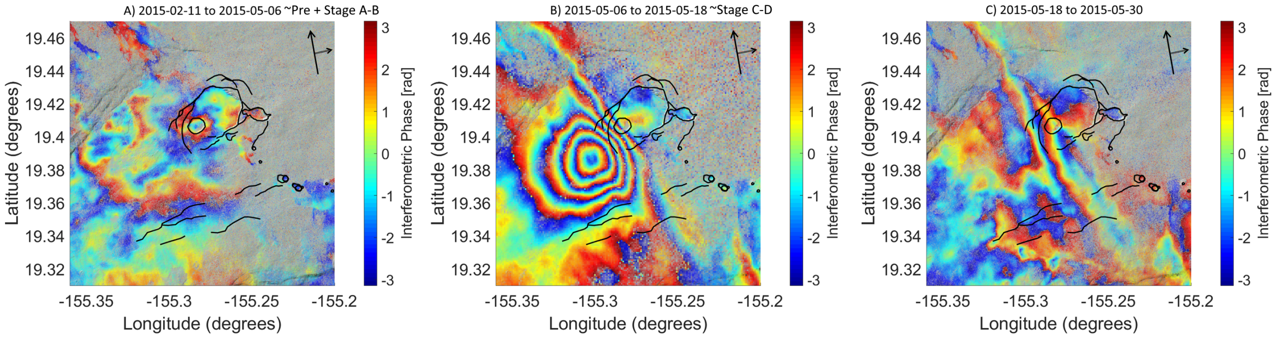

Figure 34: Individual wrapped interferograms from the ascending orbit over period, A) 2015-02-11 to 2015-05-06 (most of the pre-event stage and stages A-B), B) 2015-05-06 to 2015-05-18 (roughly aligned with stages C-D), and C) 2015-05-18 to 2015-05-30 (After deformation). The transparency of the interferometric phase is scaled to the coherence value of each pixel. Each cycle of the phase corresponds to 2.8 cm LOS deformation. The flight direction and looking direction are indicated by the black arrows in the top right corner of each interferogram. Characteristic surface features of the volcano have been highlighted.

The interferograms depicted in Figure 33 and Figure 34 still contain phase contributions from atmosphere, topography and orbit uncertainties/errors. However, looking at both figures, the deformation signal clearly dominates in the summit and Southern caldera for interferogram B. In the case of the Southern caldera deformation in interferogram B, going from the edge of the map to the central ring, the phase is always decreasing. This indicates that relative to the edge of the image, between the two satellite passes used for this interferogram, the Southern caldera has moved closer to the satellite, suggesting surface uplift. Following the same approach, the summit caldera has moved closer to the satellite in interferogram A and has moved away from the satellite in interferogram B for both the ascending and descending stacks. This suggest surface uplift of the summit during the periods from interferograms A and subsidence during the periods of interferograms B. The location and the amount of deformation in both figures (obtained by counting the phase cycles to the center of deformation) agrees with the displacement pattern observed by the GNSS stations (see Figure 30). In both figures, interferogram C does not show the same deformation signals. This is expected as, according to Figure 24, only a small amount of deformation was expected to occur after May 16th. Because of this, the interferometric phase of interferogram C is most likely not dominated by the deformation, but rather by phase changes due to atmospheric disturbances.

The areas where the interferometric phase is (nearly) transparent have low coherence values which indicate that the amplitude of the pixel changed significantly between the two satellite passes. The normalized amplitude dispersion (Equation (2.2.3)) is used as an initial PS pixel indicator. So these areas with low coherence will most likely not contain many PS pixels and will not be used for the deformation modelling.

5.2.2 InSAR phase offset and GNSS displacement offset

As noted previously the acquisition dates of the ascending and descending stacks are not exactly the same. So using multiple different interferograms (which span different dates and therefore might not include the same deformation) is undesirable when estimating the source of a single deformation event. As shown in Figure 24 some the PS pixels within the area transition from one stable state to another and this offset in phase over the transition is estimated (see Section 4.1). The LOS offset between the two stable periods for the ascending and descending stacks are shown in figure 35

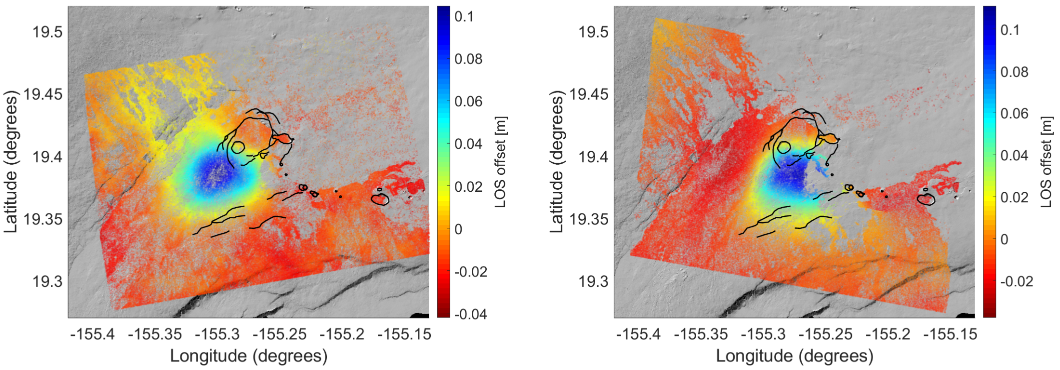

Figure 35: LOS offset between 2015-02-11 and 2015-06-11 for the ascending stack (left) and between 2015-04-09 and 2015-06-08 for the descending stack (right). The black lines indicate characteristic surface features of Kīlauea volcano.

Figure 35 shows that the area just south of the summit has moved a maximum of about 11 cm in the LOS direction of the master image within the associated stack. The mean angle of incidence is about 36 and 32 degrees, respectively. This results in a maximum uplift of approximately 13 cm. This is comparable to the 8-10 cm uplift observed from GNSS station CNPK (see Figure 28 located a short distance away from the maximally uplifted region.

In addition to the InSAR phase offset, the GNSS offset is also used for the deformation modelling. The GNSS displacement offset is also computed from the time series data according to Section 4.2. The North, East and Up displacement offsets from April 21st to May 18th 2015 is shown in Table 5.

Table 5: GNSS displacement offset and uncertainty (unc.) of stations located near the summit and southern caldera region of Kīlauea volcano.

Station name	North offset(1σ unc.) [mm]	East offset(1σ unc.) [mm]	Up offset(1σ unc.) [mm]
APUH	-62.4 (13.5)	38.2 (6.4)	92.7 (14.9)
BYRL	26.1 (3.4)	11.7 (3.3)	18.5 (8.1)
CNPK	29.8 (4.4)	-62.5 (8.9)	71.8 (13.8)
CRIM	12.5 (6.3)	20.5 (2.9)	80.7 (12.2)
DEVL	-24.8 (4.4)	25.0 (4.4)	19.5 (9.0)
GOPM	-12.6 (5.1)	4.9 (3.0)	6.0 (8.7)
HLNA	-6.9 (3.4)	-0.5 (2.7)	2.1 (8.9)
HOVL	49.9 (8.0)	5.8 (2.5)	66.2 (9.7)
KAON	-8.8 (4.4)	-0.2 (3.7)	5.1 (10.1)
KOSM	-18.9 (4.2)	-31.2 (4.6)	36.3 (9.7)
MALU	-4.6 (2.5)	2.7 (2.2)	-0.5 (7.2)
MANE	-29.2 (5.3)	4.7 (2.8)	7.0 (8.6)
NPIT	45.9 (4.6)	-0.6 (2.9)	40.9 (9.2)
OUTL	-8.7 (3.0)	10.1 (3.6)	99.6 (15.4)
UWEV	44.7 (4.5)	-15.0 (3.6)	24.8 (8.1)

5.2.3 Deformation source modelling

From the previously discussed results, two deformation sources have been identified. One on the Eastern side of the Halema'uma'u crater and one in the South caldera region. These sources have been identified in literature as the HMMR and the SCR, respectively. The HMMR has been described as a small shallow source 1 km below the East rim of the Halema'uma'u crater [Heliker et al., 2003; Poland et al., 2014; Anderson et al., 2015; Wauthier et al., 2019]. The SCR is placed at roughly 3 km depth just south of the summit caldera [Heliker et al., 2003; Poland et al., 2014; Wauthier et al., 2019]. The geometry of the HMMR is often modelled as a spherically expanding/contracting source (Mogi or McTigue) and the SCR has been modelled as either spherical or elliptical sources for inflation and deflation as well as a sill-like source for the inflation event of 2006 [Baker and Amelung, 2012; Poland et al., 2014; Jo et al., 2015]

The observed uplift and subsidence at the location of the HMMR is significantly smaller in magnitude than the uplift above the SCR. The signal from the SCR overpowers that of the HMMR, so the contribution of the SCR inflation needs to be estimated and removed before the source parameters of the HMMR can be estimated. The deformation pattern from Figure 35 shows one large significantly uplifted and roughly circular area. This indicates that the source of this inflation is most likely roughly circular as observed from the LOS of the satellites. This excludes the possibility that this deformation was caused by a fault or a rectangular dike with a high dip angle. It is however still possible that the source geometry is best estimated by i) a Mogi, ii) a McTigue, iii) a spheroidal shape or iv) nearly horizontal rectangular sill . Given that the expected depth is more than 2 km, the Mogi and McTigue sources will behave similarly [McTigue, 1987]. Therefore, a McTigue source is not tested. The Mogi source geometry is the most comparable to the point source mass addition model used for the microgravity modelling. The spheroidal source was previously used by Jo et al. [2015] for determining the source of the inflation and in other research the SCR has been modelled using a sill-like source geometry [Baker and Amelung, 2012; Jo et al., 2015]. For our research the Mogi, spheroid, and sill source geometries are tested. For the modelling, the location is given in latitude and longitude and depth is given in meters below the surface. No elevation data is supplied to (or can be processed by) the GBIS software, so it assumes all data (InSAR and GNSS) is located on a flat plain.

The HMMR has only really been modelled by either a Mogi or a McTigue geometry. The depth of this source is expected to be less than 2 km. The volume of this reservoir however is often set in the vicinity of 1 km^3 [Bagnardi et al., 2014; Poland et al., 2014; Delaney et al., 1998]. In this research, a Mogi source is used to model the summit deflation after the deformation in the South caldera region is already estimated.

5.2.3.1 South caldera reservoir modelling

Mogi source modelling

The inflation of the South caldera is initially modelled by a Mogi source which can be seen as a volume change occurring at a particular point in the subsurface. The model parameters are described in the following table.

Table 6: Optimal Mogi model parameters and 95% confidence interval for N=1000000 simulations.

longitude (degrees)	latitude (degrees)	Depth (m)	Volume change (m^3)
-155.2840 (-155.2850, -155.2829)	19.3862 (19.3853, 19.3872)	3369.86 (3220.69, 3547.97)	5.38831e+06 (4.88239e+06, 5.94e+06)

Figure 36 shows the joint empirical probability distribution of the latter 900000 model realizations. The first 100000 are skipped to remove the effect of burn-in when the model has not converged to a single solution.

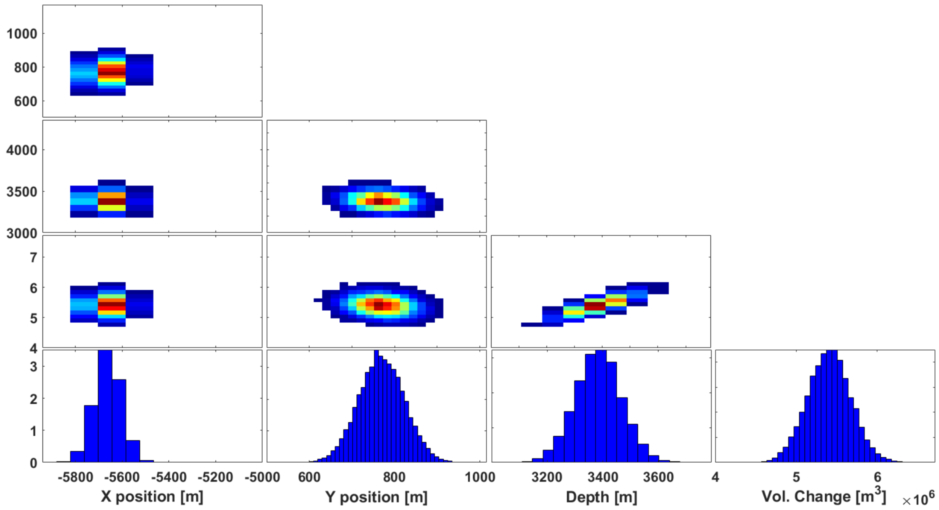

Figure 36: Empirical joint probability distribution for the Mogi model realizations

The figure shows that all parameters have an approximate normal distribution and the only observable correlation is between depth and volume change which is to be expected since a small but shallow source would yield roughly the same result as a large but deep source.

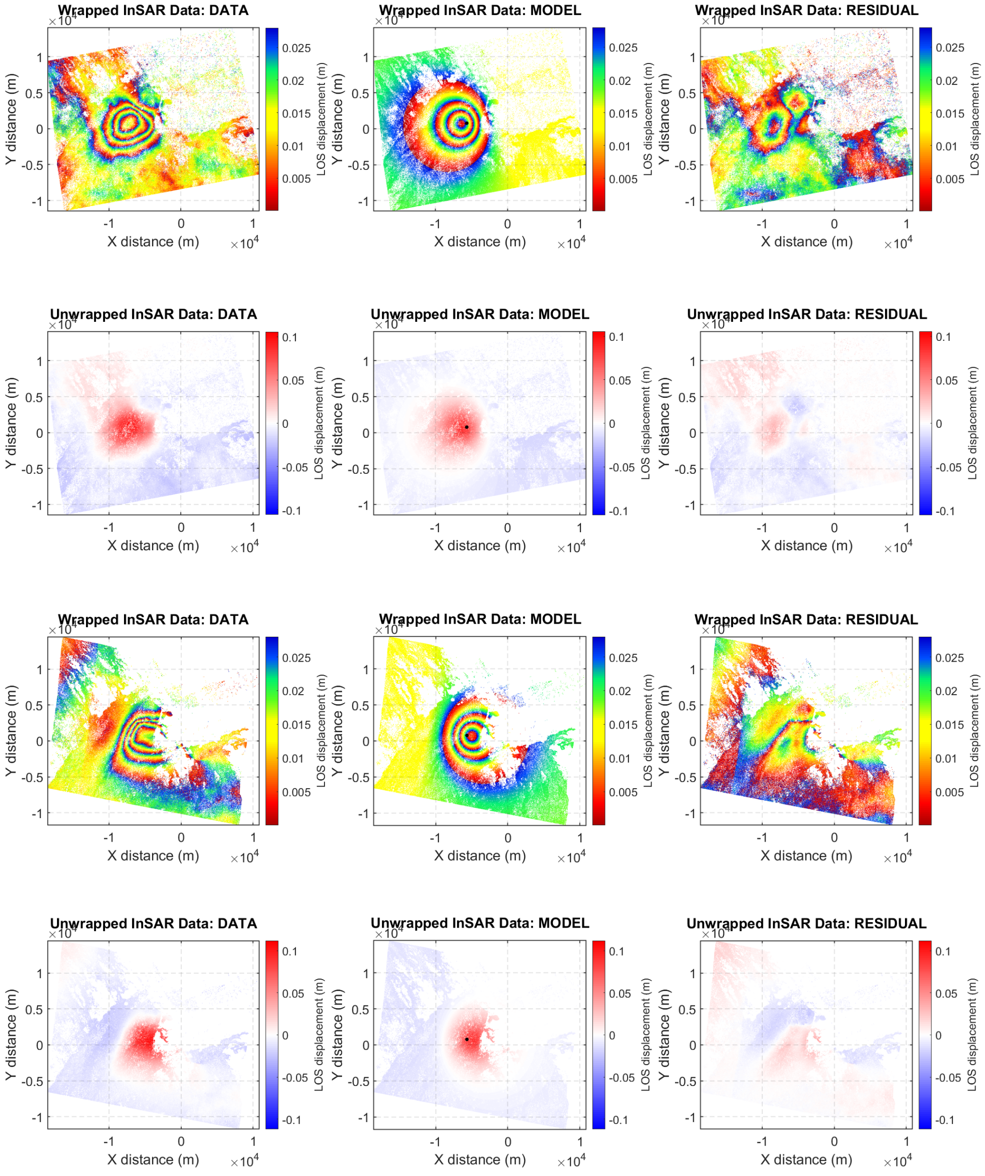

Wrapped InSAR Data: DATA

Wrapped InSAR Data: MODEL

Wrapped InSAR Data: RESIDUAL

Unwrapped InSAR Data: DATA

Unwrapped InSAR Data: MODEL

Unwrapped InSAR Data: RESIDUAL

Wrapped InSAR Data: DATA

Wrapped InSAR Data: MODEL

Wrapped InSAR Data: RESIDUAL

Unwrapped InSAR Data: DATA

Unwrapped InSAR Data: MODEL

Unwrapped InSAR Data: RESIDUAL

Figure 37: InSAR LOS offset, modelled offset and residuals for the ascending stack (up) and descending stack (bottom). The black dot in the middle column shows the location of the best Mogi source. The coordinates are in meters relative to -155.23○ E 19.38° N

The best fit Mogi model (Figure 37) is a good approximation for the deformation. However, two remaining signals are present in the residuals. The first is a region directly West of (0,0). This region has moved toward the LOS of the satellite in the ascending track and away from the LOS of the descending track. This would indicate that this area moved west compared to the rest of the frame. However, a more probable explanation comes from the fact that the two phase offset interferograms do not share exactly the same time span. Therefore, it could be the case that this region has moved during the time periods that fall outside of the shared time span. The second region of deformation that is present in the residuals is a small area NW of (0,0). This region has moved away from the LOS in both images. This suggests this area has subsided with respect to the rest of the image and is most likely the result of deflation of the Halema'uma'u reservoir (HMMR), which is discussed later in this chapter.

Sill like rectangular opening (Okada) model

A horizontal rectangular opening was used to model the 2006 inflation event [Baker and Amelung, 2012; Poland et al., 2014]. Baker and Amelung [2012] Found a poorly constrained sill-like source at 3.6 km (95% Confidence interval 2.9–4.2 km) while the distributed openings presented by Poland et al. [2014] put the optimal source depth at 3 km. Jo et al. [2015], when modeling the May 2015 event, also modelled a (near) horizontal rectangular opening. They found the best solution for the SCR at a depth of 4.25 km but rejected the model because of the multi-modal distribution of the parameters. For our modelling the sill-like source resulted in the following optimal solution and confidence intervals.

Table 7: Optimal Sill-like model parameters and 95% confidence interval for N=2000000 simulations. The latitude and longitude refer to the mid-point of the horizontal edge.

Length (m)	Width (m)	Depth (m)	Dip (°)	Strike (°)	Lon. (°)	Lat. (°)	Opening (m)
674.6 (250.4, 1457.4)	4869.6 (4235.7, 5399.0)	3992.8 (3803.8, 4282.7)	-2.0 (-5.5, 1.4)	-10.5 (-17.3, -1.8)	-155.263 (-155.266, -155.260)	19.390 (19.386, 19.392)	1.82 (0.7, 4.9)

Table 7 shows that the optimal Sill is located at a depth of 4 km with a 95% confidence interval of 3.8-4.3 km. This is towards the deep end of the estimate by Baker and Amelung [2012] for a source at roughly the same location. It is however far off the 3 km estimate from Poland et al. [2014] and even further removed from the 2 km depth found by Myer et al. [2008]. This shows that the depth of the inflation source is poorly contained or that the intrusions in this area can occur over a broad range of depths. The 675-by-4870 meter optimal rectangular opening is oriented 10 degrees west of North and dipping only slightly below horizontal. The volume of this rectangular opening is given by $vol = length \cdot width \cdot opening$, which for the optimal case is $5.98 \cdot 10^6 m^3$. This volume change is quite close to that from the Mogi model. Each of the parameters is reasonably well fitted apart from the length and the opening. This becomes much clearer when examining the joint PDF of the parameter solutions.

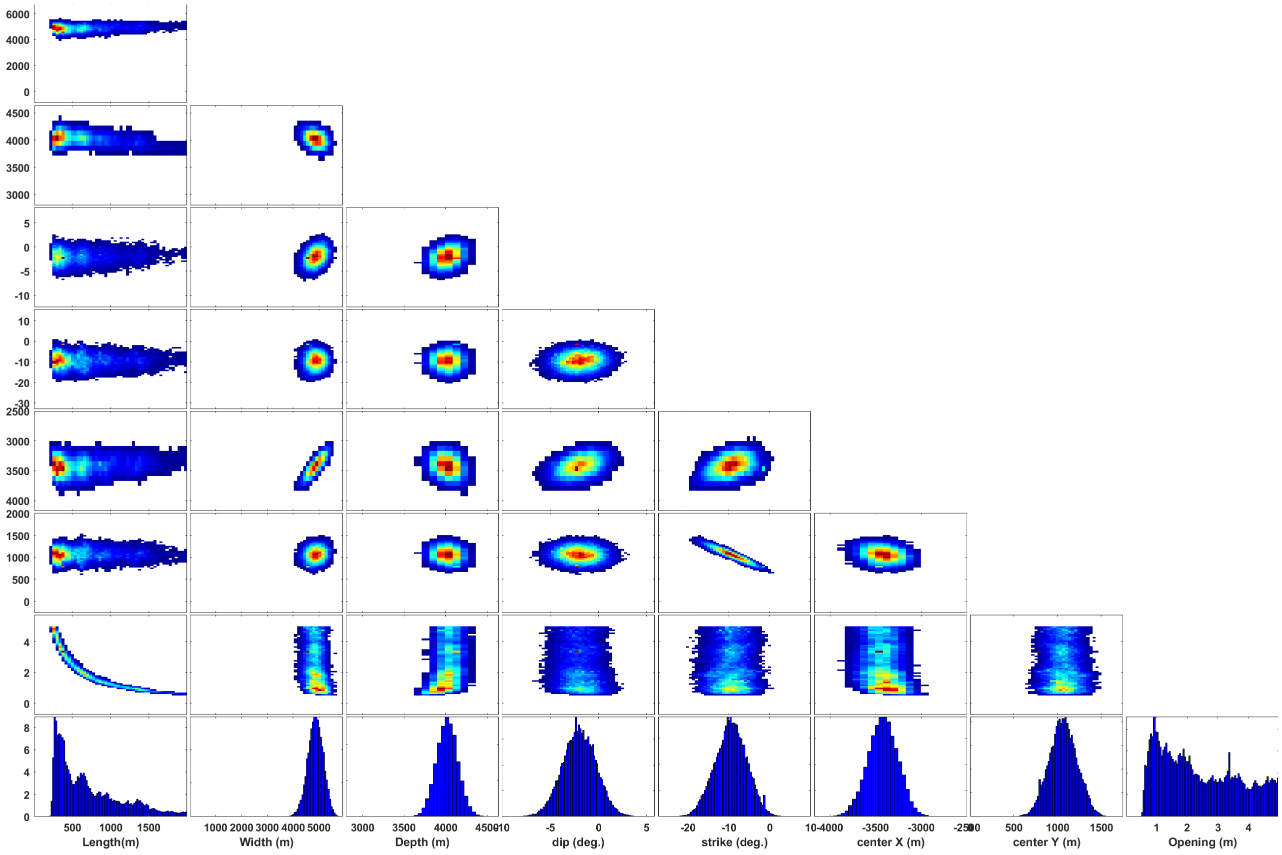

Figure 38: joint pdf of the Sill-like source geometry.

From the histograms in the bottom row it is clear that the solutions for the opening and length of the sill are not normally distributed like the other parameters. There seems to be a correlation between these two parameters where a shorter length better fits a larger opening. This seems to be a response to keep the total volume change, given by $length \cdot width \cdot opening$, approximately constant. From the joint PDF of the length and opening the most likely solution seems to be located somewhere close to the inflection point which aligns with the optimal solution found. The modelled and residual phase of the optimal Sill model is shown in Figure 39.

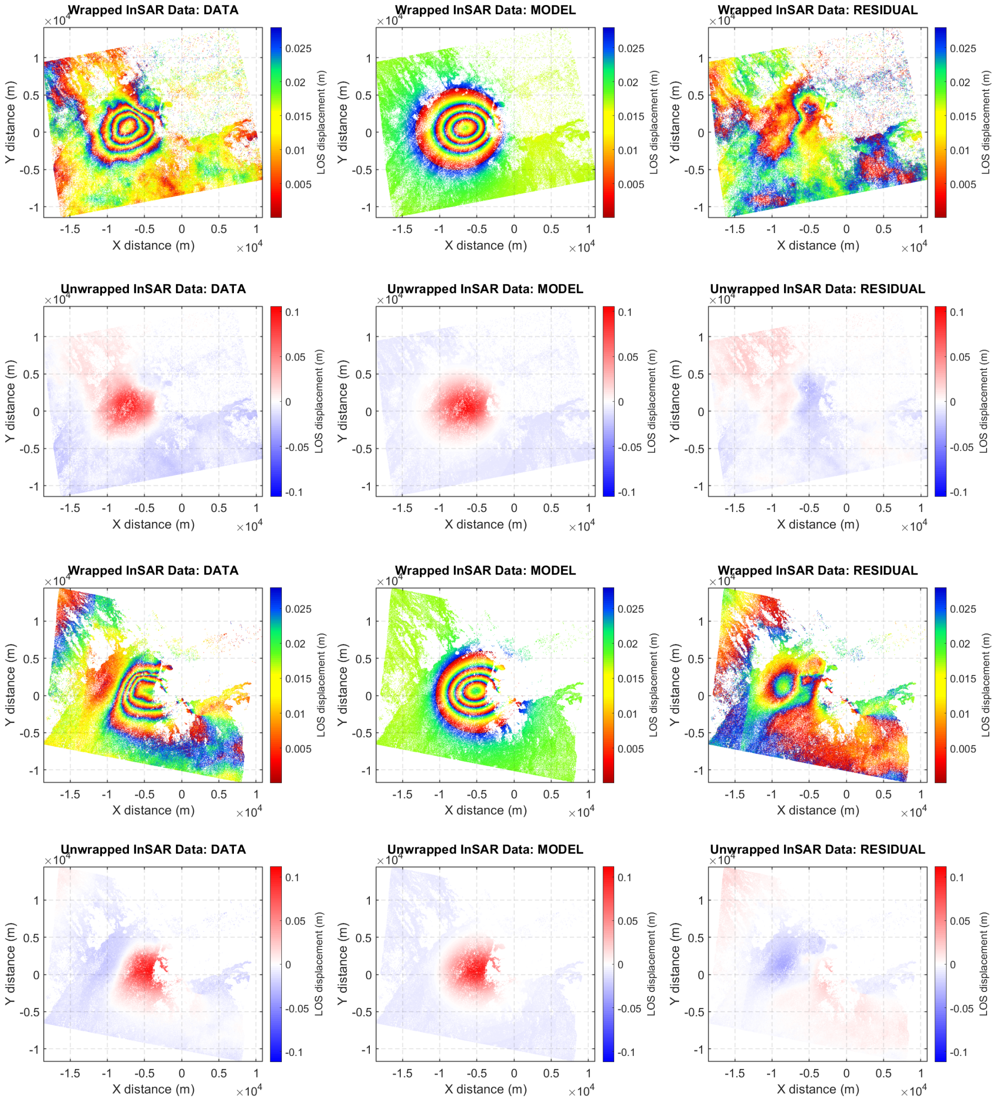

Figure 39: InSAR LOS offset, modelled offset and residuals for the ascending stack (up) and descending stack (bottom). The coordinates are in meters relative to -155.23○ E 19.38° N

In comparison to Figure 37, the sill model is an improvement from the Mogi model, as the deformation pattern is able to capture some of the oblong shape present in the InSAR phase offset images. However, the two patterns in the residual phase do remain present. The region to the West of (0,0) shows less residual phase in both ascending and descending residual interferograms and the region SW from (0,0) remains approximately the same.

Spheroidal source modelling

A spheroidal model has been used before to model inflation and deflation from 1975-1980 [Yang et al., 1992]. The source fitted by Yang et al. [1992] is located at 2.6 km depth below the Southern caldera region. Jo et al. [2015] fitted a spheroidal source to the May 2015 event and placed their source at 2.8 km depth. It was one of their most certain estimations with and 1σ uncertainty of only 12 m. Table 8 shows the optimal spheroidal model parameters and their 95% confidence intervals.

Table 8: Optimal spheroidal model parameters and 95% confidence interval for N=3000000 simulations.

Lon. (°)	Lat. (°)	Depth (m)	Major axis (m)	$^b/_a$ (-)	strike (°)	plunge (°)	$^{\Delta P}/_{\mu}$ (-)
-155.2872 (-155.2889, -155.2849)	19.3857 (19.3844, 19.3867)	2832.05 (2646.23, 3074.66)	3686.92 (3194.31, 4289.17)	0.496 (0.148, 0.681)	249.7 (241.0, 258.2)	2.342 (-3.314, 8.091)	1.15e-04 (4.11e-05, 1.46e-03)

Our optimal spheroidal model is also located at a depth of 2.8 km, however with a confidence interval of 2.65 km to 3.07 km. The size of the spheroidal chamber of Jo et al. [2015] is comparable to our optimal source. The major axis of our source is however oriented closer to the E-W direction that that of Jo et al. [2015] which was oriented NE-SW. The dimensionless pressure change can be converted to an approximate volume change by ([Battaglia et al., 2013]):

$$\Delta V \approx abb\frac{\Delta P}{\mu}(\frac{(\frac{a}{b}).^2}{3} - 0.7\frac{a}{b} + 1.37), \tag{5.2.1}$$

which, at $7.80 \cdot 10^6 m^3$, is slightly larger than the volume changes inferred by the Mogi and sill models as well as that found by Jo et al. [2015] for a similar spheroidal model. The joint PDF of the model parameters is given in Figure 40.

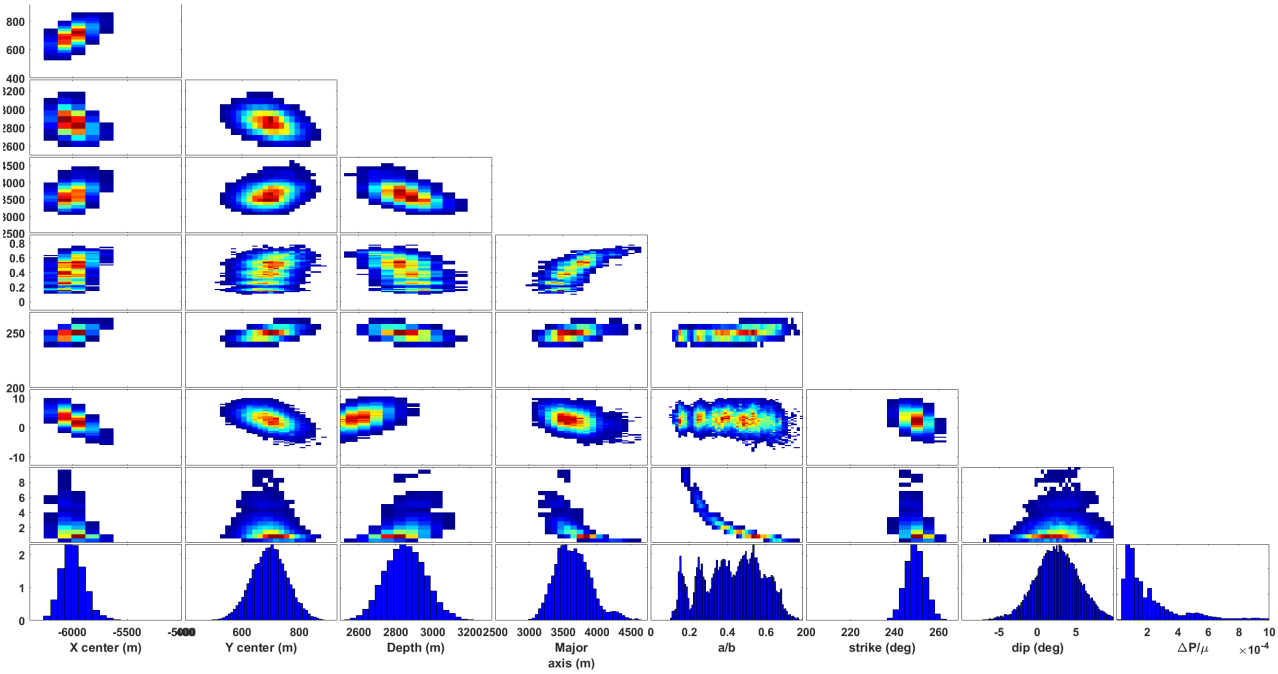

Figure 40: joint pdf of the spheroidal source geometry.

Out of all histograms of the parameters, the ratio between the major axis and minor axis of the spheroidal source ($^b/_a$) has multiple peaks. However, the overall shape of the histogram point out that the most likely ratio is in the vicinity of 0.5. There is also a strong correlation between the dimensionless pressure change ($^{\Delta P}/_{\mu}$) and the major-minor axis ratio. From the joint PDF it becomes clear that a small pressure change and an axis ratio close to 0.5 are the most probable. Our optimal spheroidal model does indeed have an axis ratio close to 0.5 and a small dimensionless pressure change. The modelled and residual phase is shown in Figure 41.

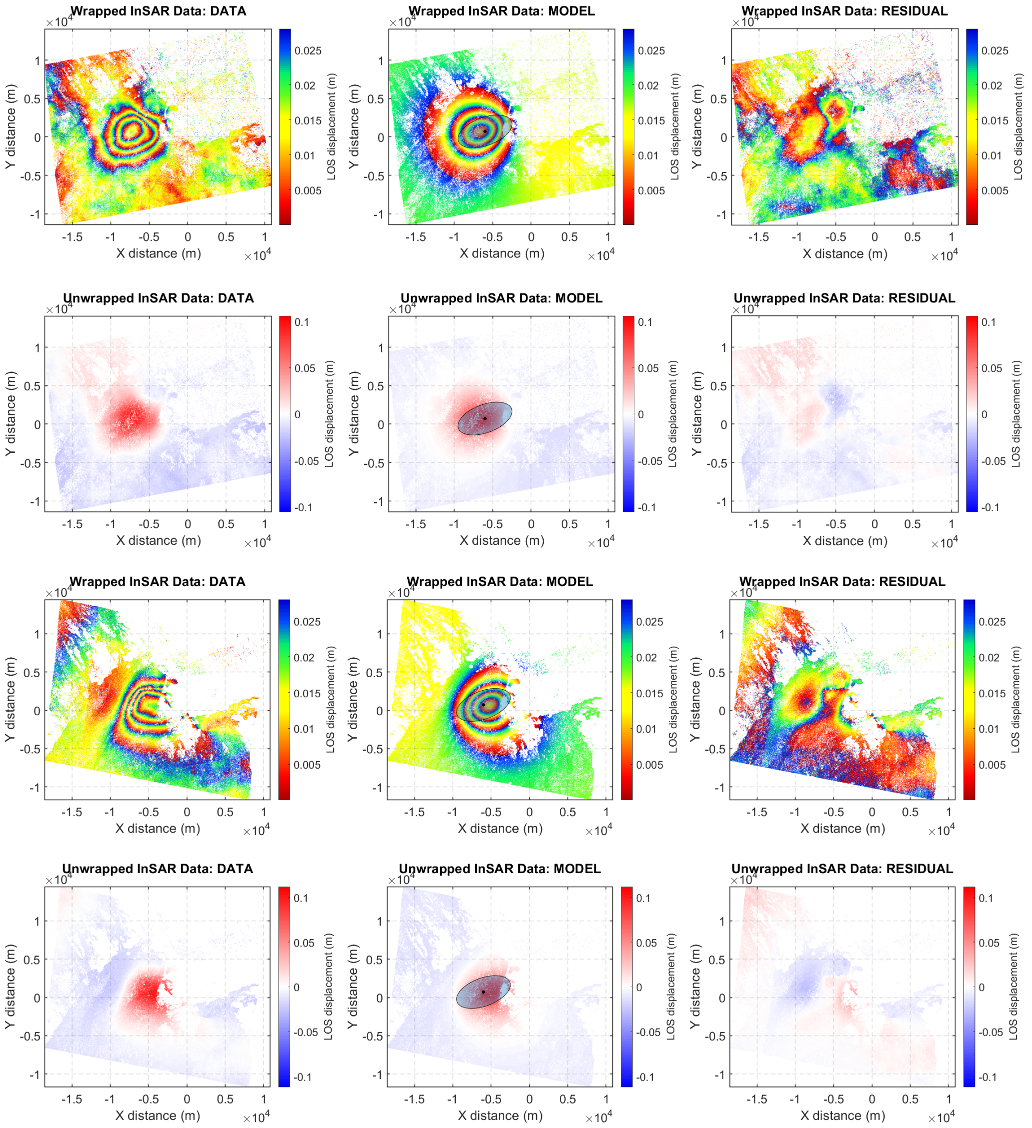

Figure 41: InSAR LOS offset, modelled offset and residuals for the ascending stack (up) and descending stack (bottom). The surface projection and center of the spheroidal source are indicated in the central images. The coordinates are in meters relative to -155.23○ E 19.38° N

The modelled phase from the optimal spheroidal source is almost exactly the same as that from the optimal sill-like source geometry, capturing the same oblong shape of the deformed region and retaining the same deformation areas in the residual phase. However, between the sill-like source geometry and the spheroidal source geometry, the parameters of the spheroidal source geometry are better constrained and the spheroidal source has fewer parameters with a multi-modal probability distribution.

The sum of squared errors (SSE) -with the error being the residual phase- is used to assess which model geometry fits best. The SSE of the models is 39.15, 46.72, and 35.19 for the Mogi, sill-like and spheroidal model geometries respectively. This shows that the fit of the sill-like model geometry is significantly worse than the other two models. The spheroidal model performs the best.

GNSS displacement comparison

Besides the interferometric phase offset, the GNSS displacement offset from Table 5 is used to estimate the deformation source parameters. The differences in Horizontal displacement between the tested models is shown in Figure 42.

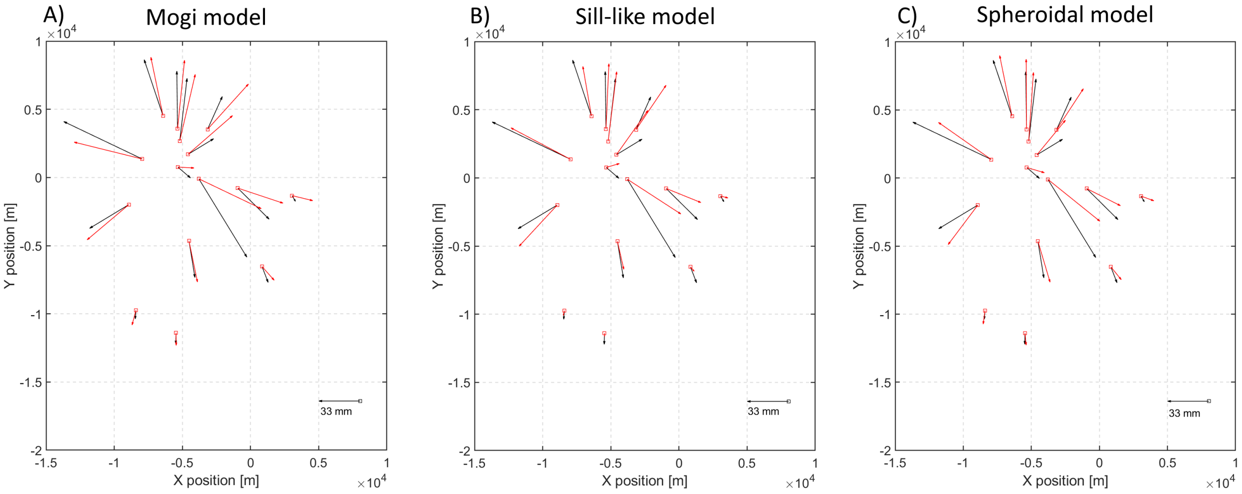

Figure 42: Comparison of horizontal GNSS displacement (black: observations; red: model) for A) the Mogi model, B) the Sill-like model, C) the spheroidal model. Output from the GBIS software. The map corresponds to the GNSS stations shown in Figure 14.

All models show horizontal displacement outward from a point located close to GNSS station OUTL (the station with relatively small horizontal displacement close to (-5000,0)). The three maps look alike, The stations to the East of the center of displacement all move significantly further South than modelled. out of the three tested geometries, the spheroidal model is able to capture this behaviour the best. The overall fit of the modelled GNSS displacement is assessed with the SSE, where the errors (or residuals) are the lengths of the vector differences between observed and modelled displacement. The SSE is 0.062, 0.089, and 0.072 for the Mogi, sill-like and spheroidal models, respectively. Again, the sill-like model performs the worst, but now the Mogi model performs best. The discrepancy of SSE results between the InSAR and GNSS residuals could be caused by the limited number of GNSS stations and their distribution.

5.2.3.2 HMMR modelling

The deformation located the Halema’uma’u crater is significantly smaller than that of the Southern caldera region. Trying to fit the Southern caldera inflation source and the summit deflation source simultaneously resulted in model parameters that would not convert or were highly dependent on their boundary conditions. It is expected that the minor overall deflation of the summit will have little influence on the model parameters of the Southern caldera inflation source which displayed significantly larger deformation. Therefore, it is possible to first fit the Southern caldera inflation source and then fit the summit deflation source to the residuals. The results of fitting a negative volume change Mogi source to the residuals is presented in Table 9.

Table 9: Optimal Mogi model parameters and 95% confidence interval for the HMMR.

SCR model	longitude (degrees)	latitude (degrees)	Depth (m)	Volume change (mˆ3)
Mogi	-155.281 (-155.304, -155.278)	19.413 (19.410, 19.428)	1559 (1352, 3874)	-180533 (-896032, -113715)
Sill-like	-155.271 (-155.284, -155.262)	19.407 (19.404, 19.421)	518 (754, 3271)	-11920 (-249382, -11113)
Spheroidal	-155.273 (-155.280, -155.268)	19.410 (19.407, 19.417)	1438 (945, 2623)	-108626 (-289236, -37643)

The table shows that the horizontal location of the Mogi source matches reasonably well no matter which SCR model has been used. Only the SCR Mogi model places the HMMR Mogi model further West than the other two. The depth of the fitted HMMR sources is about 1.5 km for the SCR Mogi and spheroidal models but about 500 m for the Sill like model. The depth of the HMMR is thought to be about 1.5 km [Baker and Amelung, 2012; Poland et al., 2014; Bagnardi et al., 2014; Anderson et al., 2015]. This further argues against the sill-like geometry as option for the SCR for the May 2015 event. A map displaying the horizontal location of the fitted HMMR models is given in Figure 43.

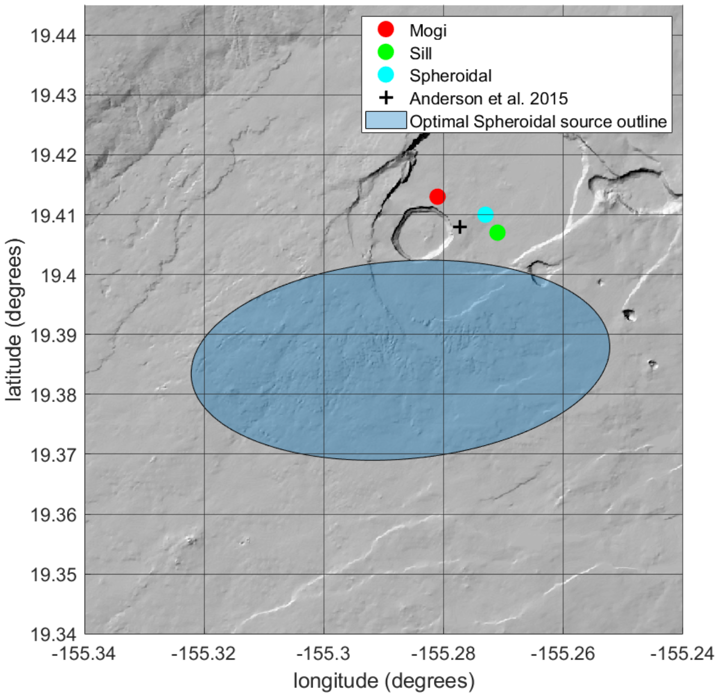

Figure 43: Horizontal location of the HMMR Mogi model fitted to the residual of the different SCR models. The location given by Anderson et al. [2015] is marked with a black plus sign. The outline of the optimal spheroidal source geometry for the SCR is shown in blue.

Of these fitted Mogi sources, the one with the spheroidal SCR model is the closest to the one given by Anderson et al. [2015] which is also the approximate position for the HMMR by others [Poland et al., 2014; Bagnardi et al., 2014]. The SSE results for the InSAR residuals is 38.94, 46.16, and 34.06 for the Mogi, sill-like, and spheroidal SCR source geometries, respectively. All SSE values reduced by the introduction of the HMMR source, with the spheroidal SCR model geometry experiencing the most improvement. The SSE values from GNSS show very little change.

5.3 Microgravity data and corrections

The microgravity data is analyzed and the results are presented in the supporting information. Part of the analysis is the FAG correction. This was done based on the vertical deformation rate as observed by InSAR satellites TSX and CSK. The vertical displacement between October/November 2012 and September 2015 is presented in Figure 44.

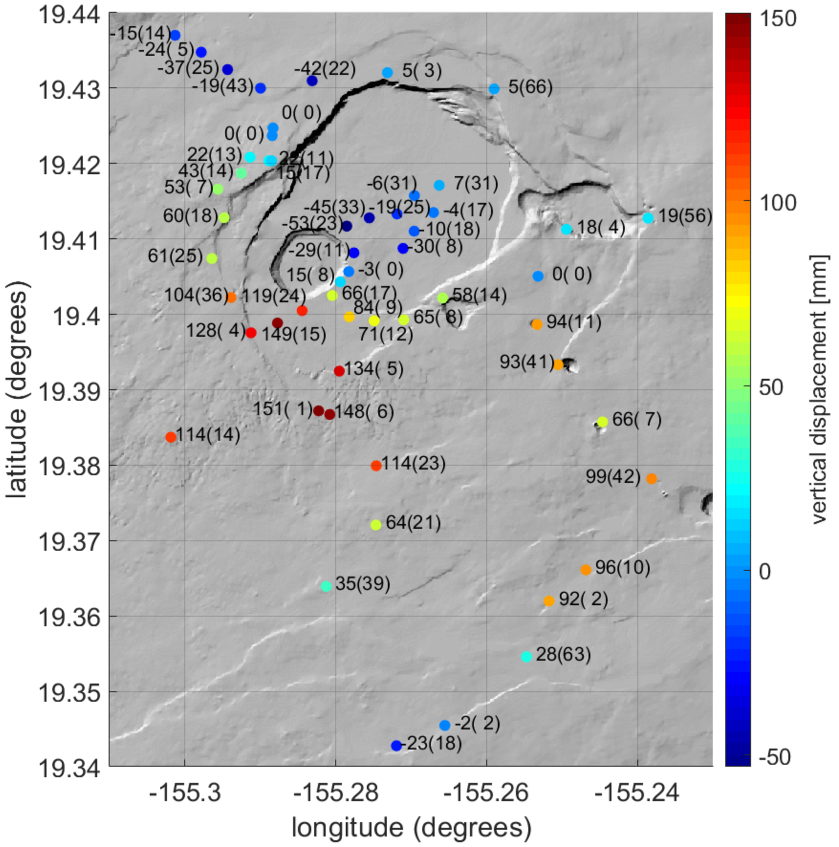

Figure 44: Map of estimated vertical displacement and uncertainty at each of the gravimeter benchmarks between October/November 2012 and September 2015.

This vertical displacement, estimated according to Section 4.4.4, is used for the FAG correction. It shows that the Southern caldera region has uplifted up to 151mm whereas the region Northeast of the Halema'uma'u crater has subsided between October/November 2012 and September 2015 by up to 53mm. The total vertical deformation at each benchmark is calculated from the deformation rate and the number of days between benchmark occupations. The FAG correction between June 2012 and October/November 2012 is taken directly from Bagnardi et al. [2014]. The net microgravity signal from June 2012 to October/November 2012 and from October/November 2012 and September 2015 are shown below. The results are the weighted mean values between the two Scintrex CG5 gravimeters used.

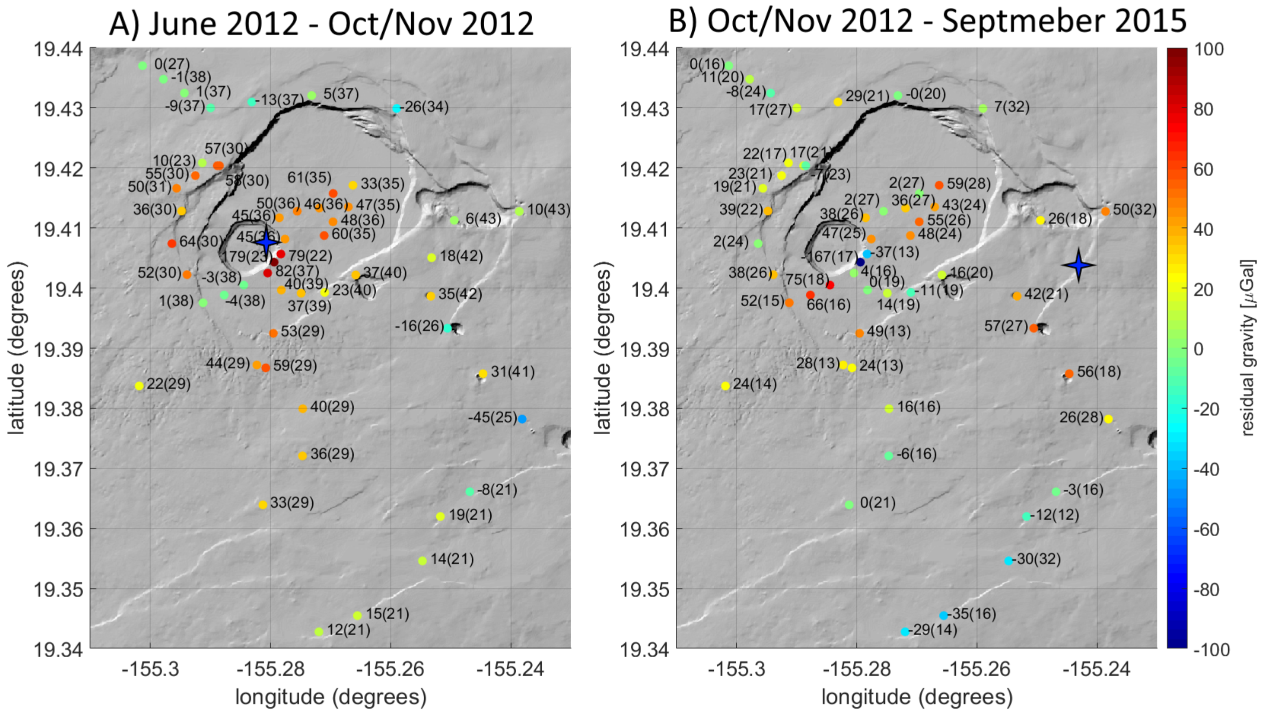

Figure 45: Net microgravity difference corrected for FAG between A) June 2012 and October/November 2012 and B) October/November 2012 and September 2015. The four-pointed star in each figure indicates the optimal fitted point source mass change location.

Figure 45 is similar to the figure made by Bagnardi et al. [2014] using the same data. The data processing is however slightly different explaining the minor differences in net microgravity changes. Nevertheless, the fitted point source location is nearly identical to that found by Bagnardi et al. [2014] which was slightly more to the East. The benchmarks closest to the lava lake go from the highest values in Figure 45 A to the lowest values in Figure 45 B. This variation is most likely due to variations in the lava lake level. The effect on benchmark HOVL-G in particular has been shown by Poland and Carbone [2016] who found a > 300 μGal drop in microgravity due to the drop in lava level from 11-16 May 2015. Bagnardi et al. [2014] corrects for these gravity changes according to a model created by Carbone et al. [2013]. Comparing the two maps from Figure 45 reveals that the better part of the gravity change between June 2012 and September 2015 occurred between June 2012 and October/November 2012. The regions where the microgravity continues to change after October/November 2012 are the Summit caldera, the Southern caldera region and the region to the Northwest of the Halema'uma'u crater. The data from the June 2012 survey and the September 2015 survey have also been compared (independently for the October/November 2012 survey). The results of this analysis fall within the uncertainty of the summation of the two periods presented in Figure 45. This indicates that averaging of the results from two instruments for each of the surveys give consistent results and that the October/November 2015 survey did not have any significant measurement errors. Such an leave-one-out assessment cannot be performed for the June 2012 or September 2015 surveys.

5.3.1 Microgravity modelling

A mass change point source is fitted to the data. For the gravity difference between June and October/November 2012, starting at the proposed location of the HMMR by Bagnardi et al. [2014], and for October/November 2012 to September 2015 a point source is fitted starting in the Southern caldera region using the best fit solution from Jo et al. [2015]. The size of the mass change is also inferred from the volume change presented by Jo et al. [2015] using a magma density of 2600 $^{kg}/_{m^3}$. In both cases, the horizontal location, depth and mass change were allowed to vary in order to find an optimal solution. The best-fit point source mass change solution for June to October/November 2012 is located at a depth of 2.04 km close to the proposed location of the HMMR, with a mass change of $0.46 \cdot 10^{1}1$ kg. This is comparable to the 1.59 km depth and $0.56 \cdot 10^{1}1$ kg mass change found by Bagnardi et al. [2014] for the net gravity change between March 2011 and October/November 2012. The best fit location for a point source mass change between October/November 2012 and September 2015 is located at 3.42 km, several kilometers East of the Summit caldera. This location does not correlate with the location of the deformation according to 44. There is a net gravity increase of 25-50 μGal in the Southern caldera region which does correlate with deformation in the region. The best fitted location represents the combined average location of the mass addition/subtraction processes from October/November 2012 to September 2012. This includes the May 2015 event and approximately the 2.5 years before and 3 months after the May 2015 event. Furthermore, benchmarks to the Northeast of the lava lake have subsided between October/November 2012 and September 2015. mass removal causing deflation of the HMMR would result in a net gravity decrease in that region. However, gravity has increased in the region over this period. This mismatch between observations indicates that mass was added to the region that did not result in uplift.

5.3.1.1 Forward modelling from deformation sources

The Mogi deformation sources from Section 5.2.3 can be used to determine the gravity change at the location of each benchmark assuming the added/ removed volume has a density of 2600 $^{kg}/_{m^3}$. This gravity change is shown in the figure below.

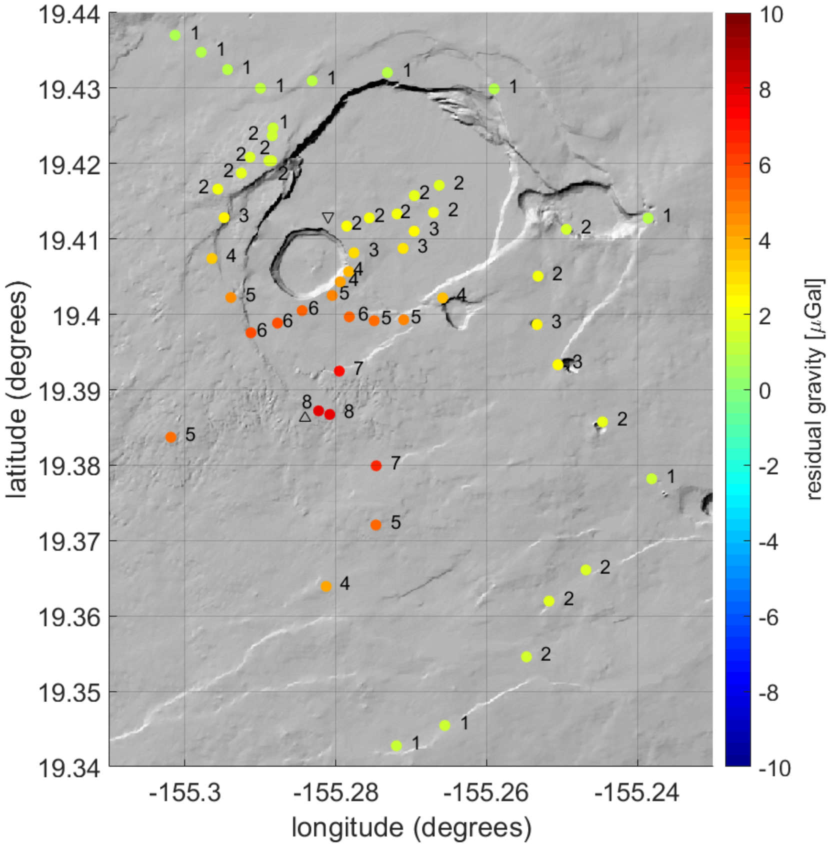

Figure 46: Forward gravity change model for the two fitted Mogi models using data from Tables 6 and 9. The black triangles indicate the horizontal location of the two Mogi sources (upward pointing : positive volume change, downward pointing: negative volume change).

Figure 46 shows that the expected signal from the Mogi models will only result in a surface gravity change of 8 μGal closest to the SCR source. This is far below the observed microgravity changes from Figure 45 B at 25-50 μGal. On top of that, the gravity change patterns of Figure 45 B and Figure 46 do not match. The microgravity changes between October/November 2012 and September 2015 do not match the expected gravity changes from volume addition/subtraction during the May 2015 event alone. This means that, baring incorrect observations, the two point source model is not complex enough to describe the observed microgravity changes. There are multiple possible explanations for this mismatch which are not taken into account in the point source model: 1) mass addition/subtraction between October/November 2012 and the start of the May 2015 event 2) filling and emptying of void space, 3) compressibility of magma and/or 4) densification of the reservoirs.

6 Discussion

6.1 Evolution of activity

In general, the combined data paint a clear picture of what happened during the May 2015 event. During stage A, surface deformation observed by GNSS, tilt and InSAR all point to inflation centered around the Eastern edge of the Halema'uma'u crater (see Figures 30, 31 and 33). Increased earthquake activity during this period is also centered around this region at depths of 1-3 km (see Figures 26 and 25). Together with the rise in lava level this indicates that pressure increased in the Halema'uma'u reservoir, located at approximately 1.5 km depth below the east edge of the Halema'uma'u crater. Stage B is described by only minor surface deformation centered around 1.5 km to the Southeast of Halema'uma'u crater, near the Keanakāko'i crater. The increased seismic activity in the upper ERZ and Southern caldera indicates that magma was not only moving to the HMMR. Baker and Amelung [2012] points out that increased seismic activity in the upper ERZ is associated with a magma storage area located Southeast of the caldera at a depth of 3.4 km, referred to as the Keanakāko'i reservoir by Poland et al. [2014] (see Figure 6). Poland et al. [2014] proposes that inflation of this region represents a temporary storage of magma. Deformation near Keanakāko'i crater is also observed in the descending track interferogram from May 3rd to May 18th 2015 (see figure 33 B), but is not clearly observed in the phase offset signal (see Figure 35). This strengthens the temporary storage hypothesis. The accumulation of magma in this region may be due to build-up of magma that cannot escape through the ERZ. This would also explain why the lava lake reached historically high levels during this period. The magma flux into the shallow plumbing system could not (easily) escape through the ERZ causing an increase in pressure and a rise in lava level of the Halema'uma'u reservoir and lava lake, respectively. The lava level dropped when the magma found another pathway during stages C and D when the seismic activity in the clogged up upper ERZ reduced to background activity. Stage C saw a lava level drop and surface deformation indicative of deflation of the HMMR. The earthquakes that occurred during this stage were mostly located in the southern caldera region and hinting at continued activity of the SCR. The drop in lava level, which acts as a proxy for pressure decrease of the HMMR [Patrick et al., 2015], and the increased seismic activity in the SCR could be explained by a hydraulic link between the HMMR and the SCR. Poland et al. [2014] already suggested the existence of such a hydraulic link between these reservoirs and between the SCR and the ERZ to explain prior activity of the East Rift Zone, the lava lake and Halema'uma'u reservoir and the Southern caldera reservoir. Stage D sees a further drop in lava level after a day of stability (see Figure 32) and significant surface deformation indicative of inflation of the Southern caldera reservoir. The simultaneous drop in lava level and inflation of the Southern caldera reservoir suggests that deflation of the HMMR continued from stage C to stage D as the magma moved away from the HMMR to flow into the Southern caldera reservoir and intrude into upper SWRZ. A schematic version of the magma transport within each stage of the May 2015 event is shown in Figure 47

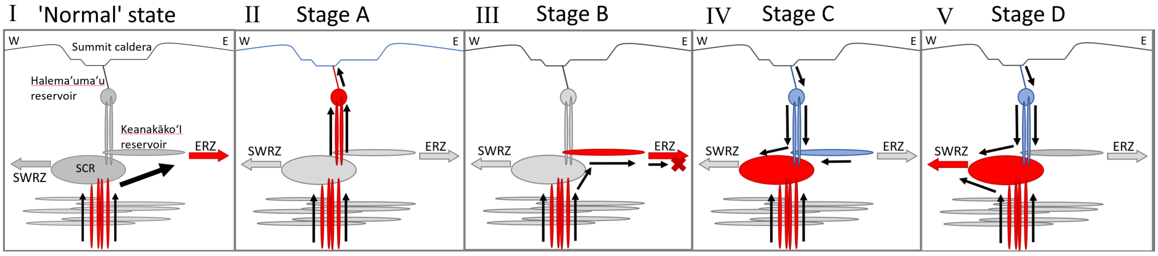

Figure 47: Schematic of the deviatoric behaviour during the different stages of the May 2015 event. The cross sections run from West to East and show surface features of Kīlauea volcano along with a simplified version of the proposed plumbing system of the volcano taken from [Baker and Amelung, 2012; Poland et al., 2014]. Red colors indicate pressurization/inflation, blue colors indicate depressurization/deflation and grey colors indicate inactivity. I) The general state of the plumbing system with the magma supply from below mostly going into the ERZ without observed deformation in the summit region. II) Activity during stage A with the pressurization of the HMMR. III) Stage B, the possible temporary storage of the Keanakāko'i reservoir and the inability of more magma to flow down the ERZ. IV) Stage C, draining of the Keanakāko'i and Halema'uma'u reservoirs moving into the Southern caldera reservoir. V) Stage D, Inflation of the Southern caldera reservoir with more draining from the Halema'uma'u reservoir, intrusion into the upper SWRZ. Schematic is not to scale.

The ability to observe these rapid changes with ground and space geodetic instruments speaks to the effectiveness of the measurement network and the use of InSAR to gain insight into the volcanic processes of Kīlauea volcano.

6.2 Cause of deformation

The deformation observed during the May 2015 event originated at the Halema'uma'u reservoir. This build up of pressure is due to an imbalance of the magma influx and drainage from the reservoir, which was already postulated by Dzurisin and Poland [2018]. Additionally, from the sudden onset of HMMR inflation, we can assume that a sudden change in the situation must have taken place that started the gradual build up of pressure. This imbalance could be caused by 4 possible mechanisms: 1) an increase in the magma supply rate, 2) declined efficiency of the ERZ conduit, the primary drainage pathway of the shallow plumbing system, 3) filling up of the directly available void space near the HMMR and SCR, or 4) a combination of two or all of the processes.

Mechanism 1 is an increase in the magma supply rate. This has already been observed between 2003 and 2007 [Baker and Amelung, 2012; Poland et al., 2014; Anderson and Poland, 2016] before subsequently dropping between 2007 and 2012 [Poland et al., 2014; Anderson and Poland, 2016]. Dzurisin and Poland [2018] hints at a possible increase in the magma supply rate between 2012 and 2015. However, this gradual process alone does not explain the sudden onset of HMMR inflation. Mechanism 2 is a reduction in efficiency of the ERZ conduit. Stress perturbations in the upper ERZ could be due to inflation/ deflation of the area or movement of the southern flank. These stress perturbations may in turn affect the flow rate through the ERZ conduit [Chouet and Dawson, 2013]. Sudden (partial) closure of the ERZ conduit would result in magma backing up toward the summit. Seismic activity and inflation started at the summit indicating that a sudden change in efficiency of the ERZ conduit is not a likely culprit. If the influx of magma from the summit to the ERZ was already near its maximum before the May 2015 event, the increase in pressure could not be accommodated (quickly) by an increase in magma flux to the ERZ. As the pressure build up, magma might have been temporarily stored in the Keanakāko'i reservoir before pressurizing the SCR and intruding into the upper SWRZ. The reduction in the flow capacity of the ERZ conduit is also inferred from observations of flow vigor which over the period of 2013-2015 remained low [Dzurisin and Poland, 2018]. The reduced flow rate through the ERZ over these years would have shrunk the size of the ERZ conduit reducing its maximum capacity.

The third mechanism, filling up of the available void space in the summit region, could have caused the imbalance in the magma flux. Filling and draining of void space has been used to explain mass addition in the subsurface without accompanying surface deformation [Johnson et al., 2010]. If the magma supply rate remained constant and was split between filling up void space and going down the ERZ, then when the available void space ran out, an imbalance occurred because the ERZ conduit could not deal with the sudden increase in volume. The long term trend in lava level between 2008 and 2015 presented in Poland and Carbone [2016] could reflect the gradual filling of available void space which accommodated part of the magma supply rate. When the void space was filled up, this part would need to pass through the ERZ conduit which might not have enough capacity resulting in inflation of the summit region. Finally, with mechanism 4, the May 2015 event could have been caused by a combination of the previously discussed mechanisms. The lower magma supply rate around 2010-2012 could have narrowed the ERZ conduit lowering its maximum flow capacity. At the start of the May 2015 event, the possible steady increase in magma supply starting in 2012 could have reached this maximum flow capacity, any additional magma supply would have gone to inflation of the summit and southern caldera region. Alternatively, assuming a constant magma supply rate, the inflation could also have been triggered by the near complete filling of void space which removed available accommodation space for part of the magma supply. When this space was no longer available, this part of the magma supply resulted in inflation of the summit. This pressure increase was eventually alleviated by volume addition to the SCR and intrusion in the upper SWRZ. The evidence presented in Dzurisin and Poland [2018] seems to point toward a combination of increased magma supply rate and reduced ERZ conduit efficiency. However, without an estimate of magma supply rate or the filling of void space, the reason why the imbalance in supply rate and discharge was reached remains speculative.

6.3 Insights gained from microgravity surveys

The interpretation of the net microgravity data is complicated due to the long time span between surveys. The net microgravity changes between June 2012 and September 2015 seem to have mostly occurred between June and October/November 2012. The gravity changes between October/November 2012 and September 2015 do not reflect the expected microgravity changes inferred from the surface deformation of the May 2015 event. The long time span between the 2012 surveys and the 2015 survey is unfortunate. When gravimetric surveys are only performed after significant deformation events and/or volcanic activity, the microgravity change that took place due to this activity cannot easily be distinguished from the total microgravity signal. This is the case when comparing the October/November 2012 and September 2015 microgravity surveys. It is likely mass changes in the subsurface occurred in the region even before the onset of the May 2015 event between October/November 2012 and May 2015. Poland and Carbone [2016] found that continuous gravity observations from 2012 to 2015 by the continuous microgravity (station HOVL-G co-located with GNSS station HOVL) show unexpectedly strong mass surges. They suggest magma flux to and from the shallow plumbing system. No clear deformation was observed during this time period, which Poland and Carbone [2016] attributes to the filling of void space in the region. The filling of void space complicates the interpretation of the campaign microgravity results. Deformation observed during the May 2015 event suggests a minimum of $2.03 \cdot 10^{10}$ kg mass accumulation in the Southern caldera region (assuming a density of 2600 $^{kg}/_{m^3}$ and the volume change from the Spheroidal model). This estimate is a minimum since processes like the compressibility of magma or the filling of void space would have added mass without accompanying surface deformation. Similarly, mass depletion of $-2.82 \cdot 10^{8}$ kg is suggested East of the Halema'uma'u crater. The surface microgravity changes which would result from the subsurface volume changes estimated from the model that best fits the deformation data are significantly lower than the gravity changes observed. Additionally, the fitted point source solution to the microgravity changes between October/November 2012 and September 2015 does not clearly align with any features of the Kīlauea plumbing system. This is because this point source is fitted to all the activity between October/November 2012 and September 2015. In contrast, the fitted point source mass change between June 2012 and October/September 2012 is close to the proposed location of the HMMR, suggesting that this reservoir was primarily responsible for the observed changes in microgravity at this time.

6.4 The 'missing' gravity signal

The expected surface gravity change inferred from the deformation modelling is significantly smaller than the actually observed net microgravity changes. This suggests mechanisms were active that can add mass to the subsurface without resulting in significant surface deformation. The same question was posed by Bagnardi et al. [2014] who also found a discrepancy between the estimated volumes, from gravity data and surface deformation, between March 2011 and October/November 2012. Johnson et al. [2010], who investigated the microgravity changes and deformation between 1967 and 2008 lists three mechanisms that would increase mass of a subsurface magma source in the absence of notable surface deformation: 1) replacement of magma by olivine cumulates, 2) progressive assimilation of roof rock by an upward-advancing magma body, or 3) filling of existing void space by magma. Of these mechanisms, Johnson et al. [2010] states that the filling of void space is the most likely explanation as evidence for the existence of void space at Kīlauea was provided by Dawson et al. [1999]. The filling of void space could also explain the discrepancy we found between the estimated volume changes related to the SCR. This same mechanism could also be at play for the HMMR, however, Bagnardi et al. [2014] provided an additional mechanism related to the then existing lava lake and summit vent. The opening of the vent in 2008 was accompanied with an one order increase in magnitude of the gas emissions from the summit of Kīlauea volcano [Elias and Sutton, 2012]. According to Carey et al. [2013] the increased emissions are caused by convection of the lava lake which allows gas rich magma to rise to the surface, outgas and sink to deeper levels with an increased density. This outgassing could therefore progressively replace gas-rich magma with denser outgassed magma and is according to Bagnardi et al. [2014] the main mechanism for mass addition without noticeable surface deformation that occurred between March 2011 and October/November 2012. It is likely that this process continued between 2012 and 2015 along with the continued presence of the lava lake. This would also explain why, over the May 2015 event, deformation related to the HMMR indicated net deflation while a net mass addition is observed between October/November 2012 and September 2015. According to Poland and Carbone [2016] there were several discrete events of mass addition to, or subtraction from the shallow plumbing system of the volcano during 2011 to 2015. This could be the reason why the fitted point source solution from Figure 45 does not align with any of the proposed features of the plumbing system. There are no gravity surveys between October/November 2012 and September 2015, so the activities unrelated to the May 2015 event cannot be separated from the activities occurring before it. Regular or more frequent microgravity surveys would remove the signals from unrelated activity and make interpretation of the results less convoluted.

6.5 Modelling of surface deformation sources

The possible sources of volcanic activity have been modelled from surface deformation (GNSS and InSAR) to determine the volume change of the sources, and from net microgravity changes to determine the mass change of the sources. Analysis of the surface deformation data indicates that the HMMR and the SCR were the locus of surface deformation. The overall deformation pattern as presented by Figure 35 primarily shows inflation centered around the southern caldera region. The source of this deformation has been modelled from these observations and the GNSS displacements presented in Table 5. From the Mogi, sill and spheroidal source geometries, the Mogi and Spheroidal sources preformed better than the sill source as assessed by visual observation and InSAR SSE of the phase offset residuals from Figures 37, 39, and 41. Similarly to Jo et al. [2015] we find that the opening for the sill-like intrusion has a multi-modal distribution from the Monte Carlo-Markov chain model solutions. Further analysis revealed that even after $3 \cdot 10^{6}$ iterations, the sill width and opening did not converge to singular values and are strongly interdependent. This suggests that the sill-like intrusion model is not the likely source geometry for this inflation event. Inversion of the spheroidal source parameters from the data shows that all parameters converged and the distribution of the parameter values did not have multiple peaks. The optimal spheroidal source form our research closely resembles that from Jo et al. [2015] in depth and size, however the orientation and volume change are noticeably different. The solution by Jo et al. [2015] is however, about 16% larger than ours which could explain part of this volume change difference. The main differences between the research by Jo et al. [2015] and ours is the use of different data (CSK vs. Sentinel-1 and GNSS) and displacement calculation method (Multiple aperture InSAR vs PSI phase offset). These differences could explain the observed differences in the model outcomes. The depth of the spheroidal model of approximately 2.8 km also matches the depth distribution of earthquakes during the southern caldera region deformation. The similarity between the model solution of this research and that of Jo et al. [2015] who used a different data set suggests this solution is quite robust. The deformation of the Southern caldera region can therefore be best described by inflation of approximately a Northeast oriented ellipsoid centered at 2.8 km depth in the Southern caldera region. This solution also matches the proposed depth of the SCR of approximately 3 km [Poland et al., 2014; Baker and Amelung, 2012; Myer et al., 2008].

The residual phase of all three tested SCR source geometries shows a remaining deformation signal located in the summit caldera. The source of this deformation is expected to be the HMMR which, over the course of the May 2015 event, experiences a net deflation. A Mogi source was used to model this deflation present in the residual phase as seen in Figures 37, 39, and 41. The optimal HMMR solutions, found when modelling the residual phase from either the Mogi or spheroidal SCR source geometries, both placed the depth of Halema'uma'u reservoir at approximately 1.5 km. The optimal model solution for the HMMR, obtained from the sill-like SCR geometry, was places at an physically unlikely 520 meters below the surface. The volume of the HMMR is previously estimated to be in the vicinity of 1km^3[Bagnardi et al., 2014; Poland et al., 2014]. A sphere with this volume has a radius of about 620 m. If the HMMR was located at 520 meters depth, the top of the spherical body would extend above the surface which is not the case. The 1.5 km depth of the other two cases matches the depth found by Baker and Amelung [2012]; Bagnardi et al. [2014]; Poland et al. [2014] and confirms the proposed depth for the HMMR.

7 Conclusion and recommendations

Data from GNSS, tilt,lava lake level, seismic activity and InSAR all agree that the May 2015 event had four distinct stages of deformation. These stages are linked to the imbalance in magma supply and discharge rate to/from the shallow plumbing system of Kīlauea volcano. The May 2015 event started with pressurization and inflation of the HMMR which was likely caused by a combination of reduced efficiency of magma transport through the ERZ conduit between 2013-2015 and a gradual increase in magma supply rate to the shallow plumbing system starting from 2012. Alternatively, the filling of available void space could also have introduced this imbalance. The seismic activity in the upper ERZ and laterally outward displacement from a region slightly west of the Keanakāko'i crater indicates that magma transport to the ERZ increased and might have temporarily been stored in the Keanakāko'i reservoir. The drop in lava level that went accompanied by deflation of the summit, along with deflation of the summit and a increase in seismic activity in the Southern caldera region and upper SWRZ indicate that the magma started to pressurize the much larger SCR and possibly intruded into the upper SWRZ This was later confirmed by significant inflation and a swarm of seismic activity in the Southern caldera region and upper SWRZ. Activity and surface deformation waned as magma supply to the shallow plumbing system was again balanced by magma outflow.

I found two sources of inflation/deflation - the HMMR and the SCR -were active and propose that magma may have been temporarily stored in the Keanakāko'i reservoir prior to moving into the SCR and upper SWRZ. The deformation data from InSAR and GNSS related to the overall HMMR deflation and SCR inflation have been inverted to estimate model parameters resulting in an optimal spheroidal source roughly 3.7 x 1.8- x 1.8 km in size oriented Northeast-Southwest located at a depth of 2.8 km in the Southern caldera region which has increased in volume by about $7.8 \cdot 10^6 m^3$. This spheroidal source approximately matches the source found by Jo et al. [2015] especially in depth and location and aligns with the proposed location and depth of the SCR [Poland et al., 2014]. This match, considering the use of different data and a different methodology speaks to the robustness of this solution. The HMMR deflation was modelled from the residuals of the optimal SCR deformation inversion. The optimal Mogi source describing the deflation of the HMMR is located in the summit caldera East of the Halema'uma'u crater at a depth of approximately 1.5 km. This source was not identified by Jo et al. [2015] but was certainly active according to the surface deformation, seismic activity and lava level results. The HMMR experienced a net deflation over the May 2015 event but experienced an initial inflation stage smaller in magnitude. GNSS and InSAR suggest that magma could have been temporally stored, or backed-up into the Keanakāko'i reservoir from the upper ERZ where further transport was limited.

The microgravity surveys conducted before the May 2015 event in October/November 2012 and after the May 2015 event in September 2015 show little to no correlation with the observed surface deformation of the May 2015 event. The observed net microgravity is the result of the May 2015 event and all other contributing processes occurring between October/November 2012 and April 2015. Processes like the filling of void space, compression of magma in reservoirs and densification due to outgassing of magma from the lava lake have been proposed as the main contributors to surface gravity changes (without observable surface deformation) between 2009 and 2012 [Bagnardi et al., 2014]. These processes have likely continued past November 2012 and have all contributed to the observed gravity change signal between October/November 2012 and September 2015. These processes are not included in the single point source model used to estimate the mass change associated with the May 2015 event. This indicates that just the use of a point source model was not sufficient for modelling of the mass change between October/November 2012 and September 2015. More frequent campaign microgravity surveys would have helped to distinguish the contribution from the previously mentioned processes making the single point source model a possible viable modelling option. Another possibility would have been to use more complex models which take into account magma properties such as compressibility. Recently, Anderson and Poland [2016] have made great progress with these kinds of models. The microgravity data could not be used to effectively fit a simplistic model, but still provided us with valuable insights. The microgravity data proved that the mass change estimation from deformation modelling was not enough to explain the observed microgravity changes. Leading us to conclude that other processes such as void space filling/draining, magma compressibility and densification of the magma reservoirs played a role. This could not have been done without analysis of the microgravity data. Microgravity data elucidate the complexity of the volcano beyond what is possible from surface deformation data alone and allows us to think about quantifying the processes involved in the volcanic activity of Kīlauea volcano.

The analysis of ground and space geodetic data relating to the May 2015 event resulted in a significantly improved understanding of the evolution of the volcanic activity and the resulting deformation which has been linked to the activity of two or possibly three magma reservoirs in the shallow pluming system of Kīlauea volcano. The surface microgravity changes which would result from changes in these reservoirs are significantly lower than the gravity changes observed. This suggests that besides the May 2015 intrusion, other volcanic processes, such as filling of void spaces, densification of magma in reservoirs and compressibility of magma, played an important role. More frequent microgravity campaign surveys would help to understand and quantify these processes.

7.1 Recommendations

7.1.1 Repeated microgravity surveys

The lack of microgravity surveys between October/November 2012 and September 2015 is unfortunate and a consequence of the limited capacity of financial and personal resources. The May 2015 event spurred the incentive for another survey. Bagnardi et al. [2014] and Johnson et al. [2010] have shown that significant surface gravity changes can occur without significant surface deformation. More frequent microgravity surveys will help improve our understanding of these processes and will allow us to better separate them from unique (and therefore possibly important) volcanic activity like the May 2015 event. We propose regularly repeated ($\leq$ 1 year) microgravity surveys be performed in order to separate the processes responsible for surface gravity changes. The current gravity network, contains about 55 benchmarks. It takes about one week to completely measure and is therefore time and resource expensive. Reducing the network would allow for more frequent microgravity surveys without a change in the required (time) resources. Our microgravity results show that the temporal resolution is an important aspect in determining the usefulness of the microgravity surveys. When performed adequately frequently, the microgravity surveys provide the means to estimate the subsurface mass addition/subtraction which is a conserved parameter unlike the volume which is not conserved due to compressibility of the magma [Johnson et al., 2010]. The combination of microgravity data and surface deformation data provide a clear means to constrain the density of the intruded/extruded volumes which would not be possible without the microgravity surveys.

7.1.2 Keanakāko‘i reservoir

The possible temporary storage of magma below the Keanakāko‘i crater might have been captured by the Sentinel-1 satellite between May 3^{rd} 2015 and May 15^{th} 2015. This interferogram (the central image in Figure 33 not only has deformation in the Southern caldera region and the Summit caldera, but also in the area between the Southern caldera and the upper ERZ this is close to the proposed location of the temporary magma storage area. Fitting three deformation sources (one for the SCR, the HMMR and one for the temporary storage near Keanakāko‘i Crater) could provide more information regarding this feature of the complex pluming system of Kīlauea volcano.

References

Anderson, K. R. and Poland, M. P. (2016). Bayesian estimation of magma supply, storage, and eruption rates using a multiphysical volcano model: Kīlauea volcano, 2000–2012. *Earth and Planetary Science Letters*, 447:161 – 171.

Anderson, K. R., Poland, M. P., Johnson, J. H., and Miklius, A. (2015). *Episodic Deflation–Inflation Events at Kīlauea Volcano and Implications for the Shallow Magma System*, chapter 11, pages 229–250. American Geophysical Union (AGU).

Babb, J. L., Kauahikaua, J. P., and Tilling, R. I. (2011). *The Story of the Hawaiian Volcano Observatory: A Remarkable First 100 Years of Tracking Eruptions and Earthquakes*. US Department of the Interior, US Geological Survey.

Babu, A. and Kumar, S. (2019). SBAS interferometric analysis for volcanic eruption of Hawaii island. *Journal of Volcanology and Geothermal Research*, 370:31–50.

Bagnardi, M. and Hooper, A. (2018). Inversion of surface deformation data for rapid estimates of source parameters and uncertainties: A bayesian approach. *Geochemistry, Geophysics, Geosystems*, 19(7):2194–2211.

Bagnardi, M., Poland, M. P., Carbone, D., Baker, S., Battaglia, M., and Amelung, F. (2014). Gravity changes and deformation at Kīlauea Volcano, Hawaii, associated with summit eruptive activity, 2009–2012. *Journal of Geophysical Research: Solid Earth*, 119(9):7288–7305.

Baker, S. and Amelung, F. (2012). Top-down inflation and deflation at the summit of kīlauea volcano, hawai‘i observed with insar. *Journal of Geophysical Research: Solid Earth*, 117(B12).

Battaglia, M., Cervelli, P. F., and Murray, J. R. (2013). *Modeling Crustal Deformation Near Active Faults and Volcanic Centers–a Catalog of Deformation Models*. US Department of the Interior, US Geological Survey.

Battaglia, M., Lisowski, M., Dzurisin, D., Poland, M., Schilling, S., Diefenbach, A., and Wynn, J. (2018). Mass addition at Mount St. Helens, Washington, inferred from repeated gravity surveys. *Journal of Geophysical Research: Solid Earth*, 123(2):1856–1874.

Battaglia, M., Poland, M., and Kauahikaua, J. (2012). Gtools: an interactive computer program to process gravity data for high-resolution applications. In *AGU Fall Meeting Abstracts*.

Carbone, D., Poland, M. P., Diament, M., and Greco, F. (2017). The added value of time-variable microgravimetry to the understanding of how volcanoes work. *Earth-Science Reviews*, 169:146 – 179.

Carbone, D., Poland, M. P., Patrick, M. R., and Orr, T. R. (2013). Continuous gravity measurements reveal a low-density lava lake at kīlauea volcano, hawai'i. *Earth and Planetary Science Letters*, 376:178 – 185.

Carey, R. J., Manga, M., Degruyter, W., Gonnermann, H., Swanson, D., Houghton, B., Orr, T., and Patrick, M. (2013). Convection in a volcanic conduit recorded by bubbles. *Geology*, 41(4):395–398.

Cervelli, P. F. and Miklius, A. (2003). The shallow magmatic system of kilauea volcano. *US Geol. Surv. Prof. Pap*, 1676:149–163.

Chouet, B. (2003). Volcano seismology. *Pure and Applied Geophysics*, 160(3-4):739–788.

Chouet, B. and Dawson, P. (2013). Very long period conduit oscillations induced by rockfalls at kilauea volcano, hawaii. *Journal of Geophysical Research: Solid Earth*, 118(10):5352–5371.

Dawson, P. B., Chouet, B. A., Okubo, P. G., Villaseñor, A., and Benz, H. M. (1999). Three-dimensional velocity structure of the kilauea caldera, hawaii. *Geophysical Research Letters*, 26(18):2805–2808.

Decriem, J., Árnadóttir, T., Hooper, A., Geirsson, H., Sigmundsson, F., Keiding, M., Ófeigsson, B., Hreinsdóttir, S., Einarsson, P., LaFemina, P., and Bennett, R. (2010). The 2008 may 29 earthquake doublet in sw iceland. *Geophysical Journal International*, 181(2):1128–1146.

Delaney, P. and McTigue, D. (1994). Volume of magma accumulation or withdrawal estimated from surface uplift or subsidence, with application to the 1960 collapse of Kilauea Volcano. *Bulletin of Volcanology*, 56(6-7):417–424.

Delaney, P. T., Denlinger, R. P., Lisowski, M., Miklius, A., Okubo, P. G., Okamura, A. T., and Sako, M. K. (1998). Volcanic spreading at kilauea, 1976–1996. *Journal of Geophysical Research: Solid Earth*, 103(B8):18003–18023.

Delaney, P. T., Fiske, R. S., Miklius, A., Okamura, A. T., and Sako, M. K. (1990). Deep magma body beneath the summit and rift zones of kilauea volcano, hawaii. *Science*, 247(4948):1311–1316.

Dzurisin, D. (2006). *Volcano Deformation: Geodetic Monitoring Techniques*. Springer.

Dzurisin, D., Anderson, L. A., Eaton, G. P., Koyanagi, R. Y., Lipman, P. W., Lockwood, J. P., Okamura, R. T., Puniwai, G. S., Sako, M. K., and Yamashita, K. M. (1980). Geophysical observations of kilauea volcano, hawaii, 2. constraints on the magma supply during november 1975–september 1977. *Journal of Volcanology and Geothermal Research*, 7(3):241 – 269.

Dzurisin, D. and Poland, M. P. (2018). Magma supply to kīlauea volcano, hawai 'i, from inception to now: Historical perspective, current state of knowledge, and future challenges. *Field Volcanology: A Tribute to the Distinguished Career of Don Swanson*, 538:275.

Elias, T. and Sutton, A. J. (2012). Sulfur dioxide emission rates from kīlauea volcano, hawai 'i, 2007–2010. Technical report, US Geological Survey.

Faller, J. (2002). Thirty years of progress in absolute gravimetry: a scientific capability implemented by technological advances. *Metrologia*, 39(5):425.

Fialko, Y., Khazan, Y., and Simons, M. (2001). Deformation due to a pressurized horizontal circular crack in an elastic half-space, with applications to volcano geodesy. *Geophysical Journal International*, 146(1):181–190.

Fiske, R. S. and Kinoshita, W. T. (1969). Inflation of kilauea volcano prior to its 1967-1968 eruption. *Science*, 165(3891):341–349.

Fores, B., Champollion, C., Moigne, N. L., Bayer, R., and Chery, J. (2016). Assessing the precision of the iGrav superconducting gravimeter for hydrological models and karstic hydrological process identification. *Geophysical Journal International*, page ggw396.

Fossen, H. (2016). *Structural geology*. Cambridge University Press.

Fujii, T. and Kushiro, I. (1977). Density, viscosity and compressibility of basaltic liquid at high pressures. *Year Book Carnegie Inst. Washington*, 76:419–424.

Gonnermann, H. M., Foster, J. H., Poland, M., Wolfe, C. J., Brooks, B. A., and Miklius, A. (2012). Coupling at mauna loa and kīlauea by stress transfer in an asthenospheric melt layer. *Nature Geoscience*, 5(11):826.

Hanssen, R. F. (2001). *Radar interferometry: data interpretation and error analysis*, volume 2. Springer Science & Business Media.

Heliker, C., Swanson, D. A., and Takahashi, T. J. (2003). *The Pu'u O'o-Kupaianaha eruption of Kīlauea Volcano, Hawai'i: the first 20 years*. US Geological Survey Reston, Virginia.

Hooper, A. (2006). *Persistent scatterer radar interferometry for crustal deformation*. PhD thesis, PhD Thesis. Stanford: Stanford University.

Hooper, A., Segall, P., and Zebker, H. (2007). Persistent scatterer interferometric synthetic aperture radar for crustal deformation analysis, with application to volcán alcedo, galápagos. *Journal of Geophysical Research: Solid Earth*, 112(B7).

Hooper, A., Zebker, H., Segall, P., and Kampes, B. (2004). A new method for measuring deformation on volcanoes and other natural terrains using insar persistent scatterers. *Geophysical Research Letters*, 31(23).

Hooper, A. and Zebker, H. A. (2007). Phase unwrapping in three dimensions with application to insar time series. *J. Opt. Soc. Am. A*, 24(9):2737–2747.

Jo, M.-J., Jung, H.-S., and Won, J.-S. (2015). Detecting the source location of recent summit inflation via three-dimensional InSAR observation of Kīlauea volcano. *Remote Sensing*, 7(11):14386–14402.

Johannes, W. J. and Smilde, P. L. (2009). Fundamentals of Gravity, Elements of Potential Theory. In *Gravity Interpretation*, pages 23–111. Springer.

Johnson, D. J. (1992). Dynamics of magma storage in the summit reservoir of Kilauea volcano, Hawaii. *Journal of Geophysical Research: Solid Earth*, 97(B2):1807–1820.

Johnson, D. J., Eggers, A. A., Bagnardi, M., Battaglia, M., Poland, M. P., and Miklius, A. (2010). Shallow magma accumulation at Kīlauea Volcano, Hawai'i, revealed by microgravity surveys. *Geology*, 38(12):1139–1142.

Kauahikaua, J., Miklius, A., and Heliker, C. (2003). Long-term trends in microgravity at Kilauea's summit during the Pu'u 'O'o-Kupaianaha eruption. *The PuuOo-Kupaianaha eruption of Kilauea Volcano, Hawaii: The first*, 20:165–171.

Klein, F. W., Koyanagi, R. Y., Nakata, J. S., and Tanigawa, W. R. (1987). The seismicity of Kīlauea's magma system. *US Geol. Surv. Prof. Pap*, 1350(2):1019–1185.

LaCoste, L. J. (1935). A simplification in the conditions for the zero-length-spring seismograph. *Bulletin of the Seismological Society of America*, 25(2):176–179.

Lagarias, J. C., Reeds, J. A., Wright, M. H., and Wright, P. E. (1998). Convergence properties of the Nelder–Mead simplex method in low dimensions. *SIAM Journal on optimization*, 9(1):112–147.

Lederer, M. (2009). Accuracy of the relative gravity measurement. *Acta Geodyn. Geomater*, 6(3):155.

Lundgren, P., Poland, M., Miklius, A., Orr, T., Yun, S.-H., Fielding, E., Liu, Z., Tanaka, A., Szeliga, W., Hensley, S., and Owen, S. (2013). Evolution of dike opening during the march 2011 kamoamoa fissure eruption, kīlauea volcano, hawai'i. *Journal of Geophysical Research: Solid Earth*, 118(3):897–914.

McNutt, S. R. (2002). Volcano seismology and monitoring for eruptions. *International Geophysics Series*, 81(A):383–406.

McTigue, D. F. (1987). Elastic stress and deformation near a finite spherical magma body: Resolution of the point source paradox. *Journal of Geophysical Research: Solid Earth*, 92(B12):12931–12940.

Ménoret, V., Vermeulen, P., Le Moigne, N., Bonvalot, S., Bouyer, P., Landragin, A., and Desruelle, B. (2018). Gravity measurements below 10- 9 g with a transportable absolute quantum gravimeter. *Scientific reports*, 8(1):12300.

Mogi, K. (1958). Relations between the eruptions of various volcanoes and the deformations of the ground surfaces around them. *Earthq Res Inst*, 36:99–134.

Montgomery-Brown, E. K., Sinnett, D., Larson, K., Poland, M. P., Segall, P., and Miklius, A. (2011). Spatiotemporal evolution of dike opening and décollement slip at kīlauea volcano, hawai'i. *Journal of Geophysical Research: Solid Earth*, 116(B3).

Montgomery-Brown, E. K., Sinnett, D., Poland, M., Segall, P., Orr, T., Zebker, H., and Miklius, A. (2010). Geodetic evidence for en echelon dike emplacement and concurrent slow slip during the june 2007 intrusion and eruption at kīlauea volcano, hawaii. *Journal of Geophysical Research: Solid Earth*, 115(B7).

Moore, R. B. and Trusdell, F. A. (1993). Geology of Kilauea volcano. *Geothermics*, 22(4):243–254.

Myer, D., Sandwell, D., Brooks, B., Foster, J., and Shimada, M. (2008). Inflation along kilauea's southwest rift zone in 2006. *Journal of Volcanology and Geothermal Research*, 177(2):418 – 424.

Okada, Y. (1992). Internal deformation due to shear and tensile faults in a half-space. *Bulletin of the seismological society of America*, 82(2):1018–1040.

Owen, S., Segall, P., Freymueller, J., Mikijus, A., Denlinger, R., Árnadóttir, T., Sako, M., and Bürgmann, R. (1995). Rapid deformation of the south flank of kilauea volcano, hawaii. *Science*, 267(5202):1328–1332.

Owen, S., Segall, P., Lisowski, M., Miklius, A., Denlinger, R., and Sako, M. (2000). Rapid deformation of kilauea volcano: Global positioning system measurements between 1990 and 1996. *Journal of Geophysical Research: Solid Earth*, 105(B8):18983–18998.

Patrick, M. R., Anderson, K. R., Poland, M. P., Orr, T. R., and Swanson, D. A. (2015). Lava lake level as a gauge of magma reservoir pressure and eruptive hazard. *Geology*, 43(9):831–834.

Patrick, M. R., Orr, T., Sutton, A., Lev, E., Thelen, W., and Fee, D. (2016a). Shallowly driven fluctuations in lava lake outgassing (gas pistoning), kīlauea volcano. *Earth and Planetary Science Letters*, 433:326 – 338.

Patrick, M. R., Swanson, D., and Orr, T. (2016b). Automated tracking of lava lake level using thermal images at kīlauea volcano, hawai'i. *Journal of Applied Volcanology*, 5(1):6.

Pepe, A. and Calò, F. (2017). A review of interferometric synthetic aperture RADAR (InSAR) multi-track approaches for the retrieval of Earth's surface displacements. *Applied Sciences*, 7(12):1264.

Poisson, E. and Will, C. M. (2014). *Gravity: Newtonian, post-newtonian, relativistic*. Cambridge University Press.

Poland, M. P. and Carbone, D. (2016). Insights into shallow magmatic processes at kīlauea volcano, hawaii, from a multiyear continuous gravity time series. *Journal of Geophysical Research: Solid Earth*, 121(7):5477–5492.

Poland, M. P. and de Zeeuw-van Dalfsen, E. (2019). Assessing seasonal changes in microgravity at Yellowstone caldera. *Journal of Geophysical Research: Solid Earth*.

Poland, M. P., Takahashi, T. J., and Landowski, C. M. (2014). *Characteristics of Hawaiian volcanoes*. Government Printing Office.

Reudink, R., Klees, R., Francis, O., Kusche, J., Schlesinger, R., Shabanloui, A., Sneeuw, N., and Timmen, L. (2014). High tilt susceptibility of the scintrex cg-5 relative gravimeters. *Journal of Geodesy*, 88(6):617–622.

Rivalta, E. and Segall, P. (2008). Magma compressibility and the missing source for some dike intrusions. *Geophysical Research Letters*, 35(4).

Samiei Esfahany, S. (2017). *Exploitation of distributed scatterers in synthetic aperture radar interferometry*. PhD thesis, Delft University of Technology.

Tilling, R. I., Heliker, C., and Swanson, D. A. (2010). Eruptions of Hawaiian volcanoes-Past, present, and future. Technical report, US Geological Survey.

Valliant, H. D. (1991). Gravity meter calibration at LaCoste and Romberg. *Geophysics*, 56(5):705–711.

Wauthier, C., Roman, D. C., and Poland, M. P. (2019). Modulation of seismic activity in kīlauea's upper east rift zone (hawaii) by summit pressurization. *Geology*.

Yang, X., Davis, P. M., Delaney, P. T., and Okamura, A. T. (1992). Geodetic analysis of dike intrusion and motion of the magma reservoir beneath the summit of kilauea volcano, hawaii: 1970–1985. *Journal of Geophysical Research: Solid Earth*, 97(B3):3305–3324.

Yang, X.-M., Davis, P. M., and Dieterich, J. H. (1988). Deformation from inflation of a dipping finite prolate spheroid in an elastic half-space as a model for volcanic stressing. *Journal of Geophysical Research: Solid Earth*, 93(B5):4249–4257.